Rock Physics Templates for 4D Seismic Reservoir Monitoring

A case study from Yttergryta field in the Norwegian Sea

Albert Kabanda

Master of Science in Petroleum Geophysics

Department of Earth Science

University of Bergen

June, 2014

This research was carried out from June 2013 to May 2014 at the Department of Earth sciences, UiB. It was supervised by the following:

Prof. Tor Arne Johansen (UiB)

Dr. Erling Jensen Hugo (UiB)

Dr. Bent Ole Ruud (UiB)

University of Bergen

Bergen, Norway

Abstract

Time-lapse 3D seismic which geoscientists often abbreviate to 4D seismic has the potential to monitor changes especially in pore pressure, hydrocarbon and brine saturation in a reservoir due to production or water/gas injection. This is achieved by repeating 3D seismic surveys over some known time interval and the difference between different parameters can be analyzed.

This study presents the use of rock physics templates (RPTs) in both reservoir characterization and 4D seismic reservoir monitoring. 4D well-log effect modeling and RPT analysis were used to investigate the power of RPTs towards reservoir characterization and monitoring on the Yttergryta field. Gassmann's fluid substitution modeling was applied on real well-log data to model 4D well-log effects, which included compressional and shear velocity logs, density logs to produce synthetic well-logs representing the reservoir at 25%, 50%, 75% and 100% fluid saturations of brine and gas. Three cases were considered; (1) fluid saturation changes (gas-brine) in Garn formation, (2) change of the gas-water contact in the Ile formation and (3) fluid saturation changes (gas-oil) in the whole reservoir interval from top Garn to base Ile. The Not formation which is between Garn and Ile was left out during fluid substitution. Generally the average Vp/Vs for brine saturated reservoir (around 1.9) was observed to be higher than that of gas (around 1.55-1.72) saturated reservoir cases.

The original and fluid substituted logs were used to calculate amplitude versus angle (AVA) synthetics for all the three cases mentioned above using Zoeppritz equations for near angle (5) and far angle (30) degrees, using a zero phase Ricker wavelet of assumed dominant frequency 25 Hz. Seismic amplitude variation on the computed AVA prestack synthetics shown as gathers was found to be successful at showing brine substitution effects. To further appreciate these fluid saturation changes, the differences between the original (base) and the fluid substituted (monitor) AVA synthetics were calculated using the time-lapse module in Hampson-Russell software package. These encouraging results on AVA synthetics suggested that with good quality seismic data from Yttergryta field, it is possible to see a difference in AVA responses between brine and gas filled reservoirs.

After this 4D analysis on the computed prestack AVA synthetics, the results were then used in rock physics modeling (static and 4D RPT analysis). In general rock physics and 4D seismic can work together as a link between geologic reservoir parameters (like porosity, clay content, sorting, lithology, saturation) and seismic parameters (like Vp/Vs, density and elastic moduli). This combination can give a broad picture and knowledge about a reservoir in terms of fluid saturation and pressure changes to geoscientists.

RPT analysis was performed on both the original and fluid substituted well-log data from Yttergryta field in the Norwegian Sea. Different cross-plots of Vp/Vs versus acoustic impedance (AI) with different rock physics models (RPMs) have been used in the study. The study has demonstrated how RPTs can be used in reservoir characterization and monitoring.

Acknowledgements

I dearly thank my supervisors: Prof. Tor Arne Johansen and Dr. Erling Hugo Jensen for the academic love, support, training, guidance and counseling from the start to the end of my studies at the department.

I once again thank Dr. Erling Hugo Jensen for the support he gave me during the modeling of the patchy cemented sandstone model using Matlab software package, I really appreciated.

Dr. Ole Ruud Bent, I thank you for the technical support and guidance you gave me during this project. I also thank Mr. Kenneth Bredesen (PhD candidate) for the support and the different information he gave me throughout my project, I really appreciated.

Special thanks go to all the lecturers who have taught me in different courses at the University of Bergen.

I thank my CSEG mentor, Mr. Matteo Niccoli for the academic support and advice in different areas, I dearly appreciate.

I thank my family for the prayers and encouragement they gave me during this project. I thank my friend Mr. Isaac Bisaso for the academic guidance, reading through my thesis and the support he gave me.

I thank Spring Energy for providing me the well-log data that has been used in this project.

Finally great thanks go to the government of the Royal kingdom of Norway, for the great financial support, welfare towards my education, life and health here in Bergen, Norway. May the good Lord reward you abundantly.

Thank you God

Albert Kabanda

Bergen, June 2014

Table of Contents

List of tables

List of acronyms

AVA: Amplitude Variation with Angle
AVO: Amplitude Variation with Offset
AI: P-wave Acoustic Impedance
CT: Contact Theory
CCT: Constant Cement Theory
Fm: Formation
FRM: Fluid Replacement Modeling
GOR: Gas-Oil Ratio
GR: Gamma Ray
GWC: Gas Water Contact
HRS: Hampson Russell Software
KB: Kelly Bushing
MD: Measured Depth
NPD: Norwegian Petroleum Directorate
PC: Patchy Cemented
RPM: Rock Physics Models
RPT: Rock Physics Template
SI: S-wave Impedance
PR: Poisson Ratio
Vp: P-wave velocity
Vs: S-wave velocity
Vshale: Volume of shale
Vp/Vs: P-wave velocity divided by S-wave velocity
UiB: Universitetet i Bergen (University of Bergen)

Dedication

This research is dedicated to my beloved family and to the Royal Kingdom of Norway for the financial support towards my studies and entire welfare in Norway. I dearly appreciated.

One who gains strength by overcoming obstacles possesses the only strength which can overcome adversity. – ***Albert Schweitzer***

1.0 Introduction

1.1 Motivation

A major challenge in seismic exploration is the mapping of type, location, extent of hydrocarbon fluids and how they change in a reservoir with time. In seismic reservoir monitoring, the aim is to follow the temporal variations of the various spatial fluid distributions and changes during production phase (Johansen et al., 2002).

In this project, both rock physics and the knowledge of 4D seismic analysis were applied to demonstrate how a reservoir can be monitored using rock physics templates by considering different scenarios. Rock physics works as a bridge to link reservoir, elastic and seismic parameters. This provides a more quantitative link between reservoir properties, well-logs and seismic data. Figure 1.1 below summarizes the main steps in this project.

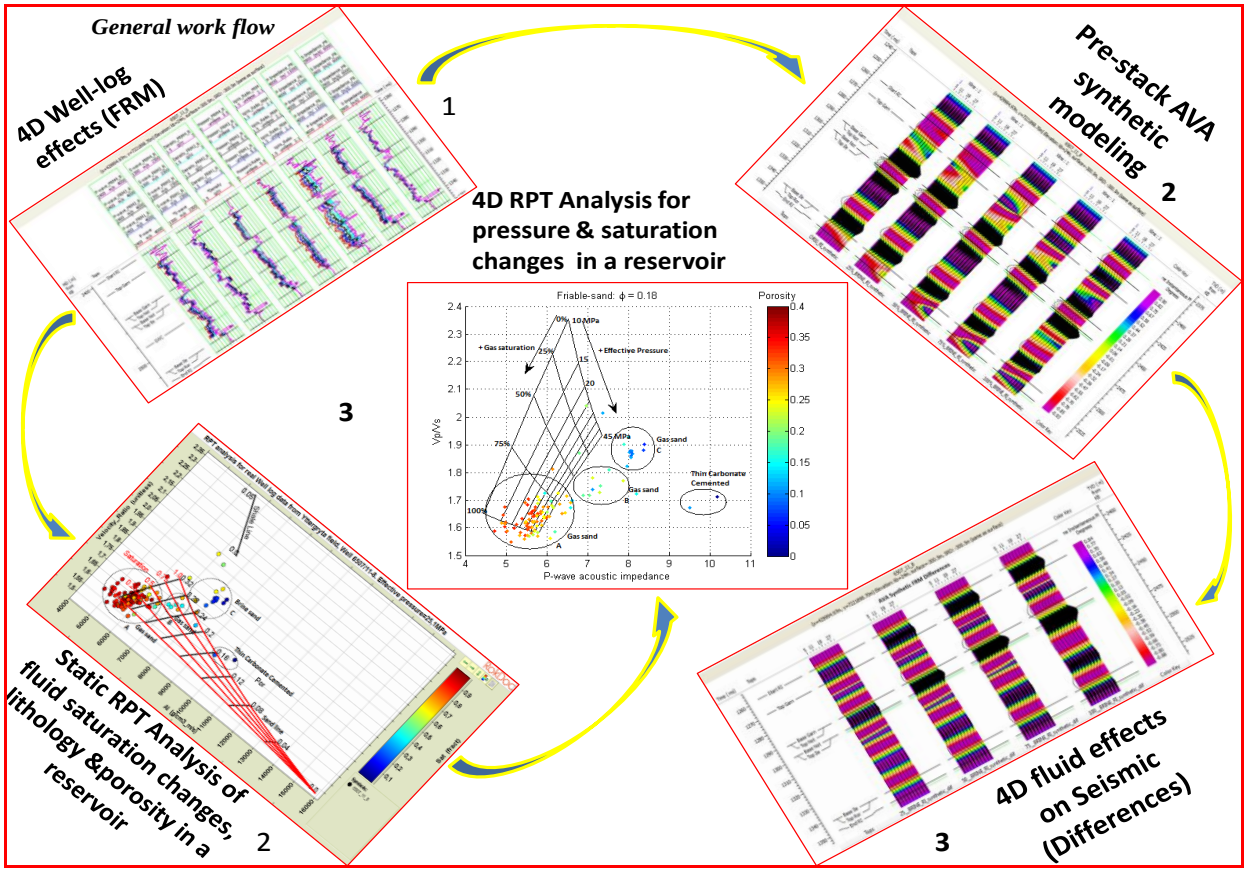

Figure 1.1: The main project work flow. 4D well-log effects are modeled through fluid substitution using Gassmann's model, this is followed by AVA synthetics computed using Zoeppritz equations and differences calculated. Static and dynamic RPTs are later applied on both the original and fluid substituted data to monitor the effects due to fluid changes as realized on the synthetics.

1.2 Main objectives

- Give a general overview of the rock physics templates (RPTs) approach of Avseth et al., 2005.
- Reservoir characterization on data by predicting reservoir properties using RPTs
- Application of RPTs in 4D seismic reservoir monitoring on data from Yttergryta field

1.3 Thesis synopsis

This thesis is presented as a series of key chapters as summarized below:

Chapter 1 covers the introduction and presents the main motivation, objectives of the thesis and the thesis synopsis.

Chapter 2 introduces the study area and provides an overview of the location of the study field.

Chapter 3 gives the background theory; this Chapter discusses all the theory that is necessary in this project. The main parts in this chapter include; elasticity theory, seismic wave velocities and pore fluid properties, petrophysics, rock physics models for dry rocks, fluid replacement modeling (FRM) and amplitude variation with offset/angle (AVO/AVA) modeling.

Chapter 4 covers the methodology; this Chapter gives an introduction to rock physics template technology which is the main method applied in this project. It shows how RPTs can be used in monitoring fluid type, fluid saturation and pore pressure changes in the life of a producing reservoir due to different activities.

Chapter 5 presents reservoir characterization on data from Yttergryta field using three models: friable sand model, constant-cement model and patchy cemented sandstone model.

Chapter 6 presents the applications of RPTs in 4D seismic reservoir monitoring on Yttergryta. This chapter contains all the results from the fluid substitution modeling where different scenarios of fluid changes have been considered. The Chapter also shows how fluid changes may affect seismic data through AVA synthetic modeling of the different scenarios. RPTs analysis for the fluid substituted datasets has also been considered in this Chapter.

Chapter 7 covers the discussion of the observations and findings in this project. The main objectives, pitfalls and solutions, rock physics model evaluation and the *'what if scenarios'* are all discussed.

Chapter 8 brings together the whole thesis to an end with findings, conclusions on the type of lithology, hydrocarbons, saturation in this field and the model that matched the dataset. This Chapter also contains a recommendation part for further study. The Chapter is followed by appendixes and references used in this project.

2.0 Study area: Yttergryta field

2.1 Introduction

In this Chapter, the location and geology of the study area are covered. The well database, location and production history are also presented.

2.2 The Yttergryta field

In this research, well-log data from well 6507/11-8 in the Yttergryta field in the Norwegian Sea has been used.

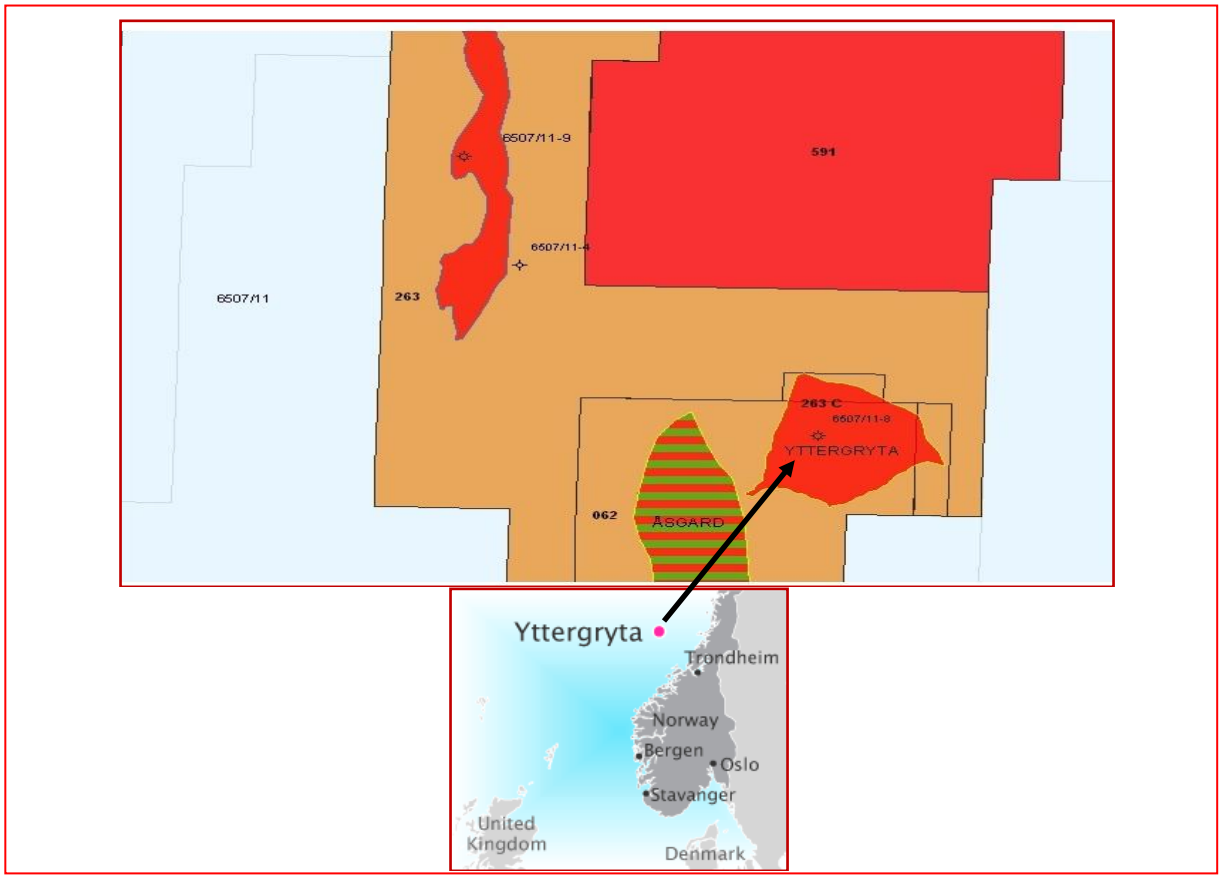

Figure 2.1: Location of block number 6507/11 in Yttergryta field in the Norwegian Sea, adapted and modified from NPD, 2014 and Statoil, 2013.

Yttergryta is a gas and condensate field in the Norwegian Sea 33 km East of Åsgard B. The provided well-log data is from well 6507/11-8 which is located on the Eastern part of the Halten Terrace on the Yttergryta structure. It was drilled to a total vertical depth of 2749 meters below Sea level and terminated in Early Jurassic rocks. The primary objective was to identify gas in the Garn and Ile formations. The secondary objective of this well was to acquire data and test for possible hydrocarbons in the Tilje and Åre formations (NPD, 2014).

The well proved gas in Fangst group from the middle Jurassic rocks. It was developed with a simple subsea production facility on the seabed and a pipeline tied back to the Åsgard B platform. The field was produced by pressure depletion and it was assumed that gas which flows from the Northern reservoir segment to the main segment during production was the reason for

the good production results. The field was later shut down in late 2011 because of water production in the gas production well (NPD, 2014).

2.3 Halten Terrace

The Halten Terrace area is situated offshore Mid-Norway, and the basin covers an area of 150x50 km. The area contains gas with natural high Carbon dioxide content that can be extracted and stored (Unknown author, 2014). The Halten Terrace forms a rhomboidal structural feature and is separated from the Trøndelag platform by the Bremstein fault zone to the East and from the Møre and Rås basins by the Klakk fault zone to the West. To the North, the terrace merges into the narrower Dønna Terrace.

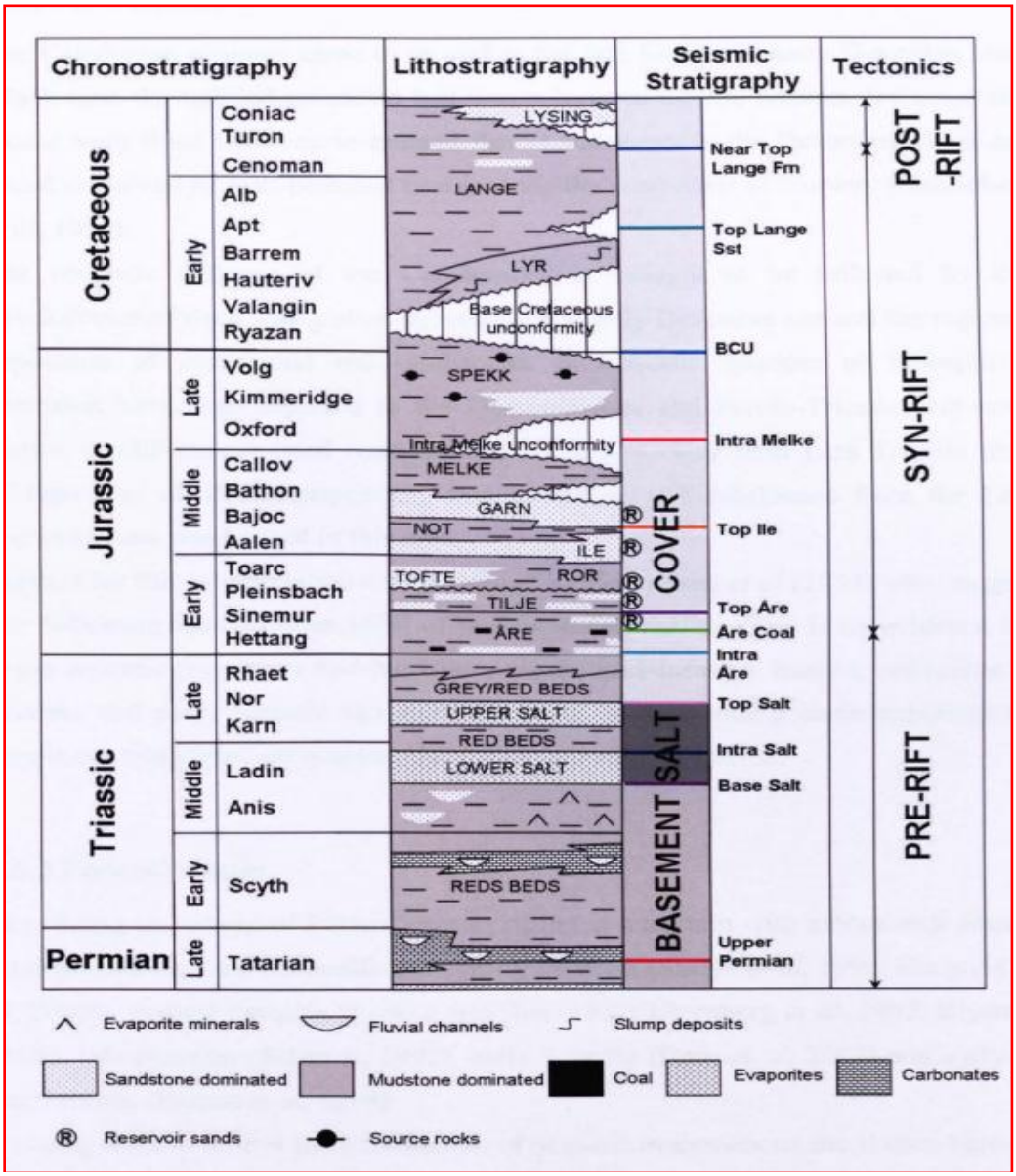

Figure 2.2: Stratigraphic frame work for Halten Terrace, showing the ages and representative lithologies of the formations present (adapted from Marsh, 2008). The main interest is in Garn, Not, Ile and Ror formations.

2.4 The Fangst and Båt Groups

The information discussed in this **Section 2.4** is referenced from NPD, 2014 however in some sections below it has been modified to fit the study well, 6507/11-8.

The Fangst group typically comprises of three lithological units: Ile, Not and Garn formations. The base of the group is defined by the base of the Ile formation. The age is of Late Toarcian to Bathonian. Shallow marine to coastal/deltaic facies dominate sequences on the Halten Terrace. Increasing continental influence is inferred towards the Trøndelag platform to the East, especially in the lower part of the group. Upper parts interfinger with marine shales to the Northeast in the Trænabanken area.

The Båt group represents a transition from the Halten Terrace to the Trøndelag platform in blocks 6507/11 and 6507/12. The Båt group consists of alternating sandstone and shale/siltstone units, with sandstone as the dominant lithology. The base of the Båt Group is defined by the base of the Åre formation. Only Ror formation in the Båt group will be discussed here. The age of Båt group is Rhaetian to Toarcian. Shallow marine to deltaic environments dominated during deposition of the group.

2.4.1 Garn Formation

The Garn formation has a gross thickness of 31.50 m (2416.0-2447.50 m, MD from KB) and a net thickness of 26.75 m in the study well. The Garn formation consists of medium to coarse-grained, moderately to well-sorted sandstones. Mica-rich zones are present. The sandstone is occasionally carbonate-cemented. The lower boundary is defined by a drop in gamma ray response. The age is of Bajocian to Bathonian. The Garn formation may represent progradations of braided delta lobes. Delta top and delta front facies with active fluvial and wave-influenced processes are recognized.

2.4.2 Not Formation

The Not formation has a gross thickness of 11.50 m (2447.5-2459 m, MD from KB) in the study well. The lithology is claystones with micronodular pyrite coarsening upwards into bioturbated fine-grained sandstones which are locally mica-rich and carbonate-cemented. The lower boundary is defined by an abrupt increase to a steady high gamma ray response. The age is of Aalenian to Bajocian. The basal part of the formation reflects a semi-regional transgression which led to the development of lagoons or sheltered bays. The upper part of the unit consists of prograding deltaic or coastal front sediments. The formation is recognized over the entire Haltenbanken area if not eroded.

2.4.3 Ile Formation

This formation has a gross thickness of 60.00 m (2459.0-2519.00 m, MD from KB) and a net thickness of 47.50 m in the study well. The lithology of Ile formation is fine to medium and occasionally coarse-grained sandstones with varying sorting are interbedded with thinly laminated siltstones and shales. Mica-rich intervals are common. Thin carbonate-cemented stringers occur particularly in the lower parts of the unit. The lower boundary is defined at the base of a generally coarsening upwards sequence visible on the gamma ray log. In the study well, the coarsening trend is evident on logs, however the base of the formation may also be picked where the overall lithology changes from siltstone to sandstone. This transition is associated with

one or more carbonate-rich beds (see Figure 3.6). The age of Ile formation is of Late Toarcian to Aalenian. The formation represents various tidal-influenced delta or coastline settings.

2.4.4 Ror Formation

This formation has a gross thickness of 75.0 m (2519.0-2594.0 m, MD from KB) and a net thickness of 3.00 m in the study well. Dominant grey to dark grey mudstones contain interbedded silty and sandy coarsening upwards sequences, commonly a few meters thick. Such sequences become more frequent towards the top of the formation, giving the unit an overall coarsening upwards trend over most of Haltenbanken. The base is defined by the abrupt transition from sandstones of the Tilje formation into mudstone. The break is well defined in most Haltenbanken wells and is easily picked on the gamma log (see Figure 3.6). The age is Pliensbachian to Toarcian. The formation was deposited in open shelf environments, mainly below wave base. The coarsening upwards trend reflects ongoing shallowing and storm-generated sands are common in the unit's upper part. Sand input from the west indicates syn-sedimentary tectonic uplift along the Western margins of the basin.

2.5 Data base: Well-log data

The table below gives a summary of the provided well-log data from Yttergryta.

Official name	Short name	Depth range (m)	Original log curves provided
6507/11-8 Yttergryta	Well 8	356.0064- 2774.8992	Depth (356.0064 -2774.8992)m Gamma ray (356.0064-2773.5)m Caliper (2390.09 – 2762.23)m Deep resistivity (356.0064 – 2773.13)m Density (2398.59 – 2758.33)m Neutron porosity (2394.52 – 2757.59)m P-sonic (2392.3 – 2750.93)m S-sonic (2391.19 – 2749.44)m Saturation (2415 – 2755.37)m Porosity (2415.99 – 2755.74)m Depth (2373 - 2773)m Volume of shale (1168.02 – 2772.76)m Depth (356.0064 -2774.8992)m

Table 2.1: Well-log summary for the data provided from Yttergryta field in the Norwegian Sea

2.6 Summary

This Chapter has briefly discussed the general location, geology of the study area and the type of data provided.

3.0 Background theory

3.1 Introduction: Elasticity theory

Elasticity theory focuses on different conditions like stress and strain in which different materials can undergo when a wave is propagating or due to different types of loading. During this period, different parameters in different material medium may change like the Poisson ratio, shear and bulk modulus and such changes affect seismic velocities. These changes are expected to vanish entirely upon removal of the stresses that cause them. In seismic exploration the amount of stress and strain lie within the elastic behavior of natural materials and Hooke's law holds.

3.2 Seismic wave velocities (P- and S-wave)

Seismic wave velocities are greatly affected by: pore fluids (brine, gas or oil and their properties under different conditions like; temperature, pressure, salinity and others), clay content, porosity, pressure and other factors. P- and S-wave velocities for seismic waves travelling in a homogeneous, isotropic and elastic media (Mavko et al., 2009) are respectively given by:

$$V_P = \sqrt{\frac{K+\frac{4}{3}\mu}{\rho}} \tag{3.1}$$

$$V_S = \sqrt{\frac{\mu}{\rho}} \tag{3.2}$$

where μ and K are the shear and bulk moduli, respectively; ρ is the bulk density of the material.

3.2.1 Porosity and clay content effects on seismic velocities

The porosity, $\emptyset$ is the fractional rock volume occupied by pore fluids. Clean and well-sorted sands are typically deposited with porosities near 40% and poorly-sorted sands will be deposited at lower porosities (Avseth et al., 2005). Porosity decreases with burial depth because of compaction due to the overlying sediments and diagenetic processes. Porosity with respect to depth is mathematically given by:

$$\emptyset(z) = \emptyset_{\mathbf{0}}(z=0)e^{-bz} \tag{3.3}$$

where z is the depth in the z-direction, $\emptyset_{\mathbf{0}}$ is the depositional porosity and b is the constant of dimension (length^{-1}).

Velocity is affected by both porosity and clay content in different ways. As stressed by Avseth (Bjørlykke, 2010), Marion (1990) introduced a topological model for sand/shale mixtures to predict the interdependence between velocity, porosity and clay content. When clay content is less than the sand porosity, clay particles are assumed to be located within the pore space of the load-bearing sand. The clay will stiffen the pore-filling material, without affecting the frame properties of the sand. As the clay content increases, so will the stiffness and velocity of the sand/shale mixture, as the elastic moduli of the pore-filling material (fluid and clay) increases. Once the clay content exceeds the sand porosity, the addition of more clay will cause the sand grains to become separated, as we go from grain-supported to clay-supported sediments (i.e. shales).

Marion assumed that, as with fluids, the pore-filling clay would not significantly affect the shear modulus of the rock. This assumption was supported by laboratory measurements on unconsolidated sand/shale mixtures (Yin 1992). The impact on the velocity-porosity relationship of increasing clay content in a sand/shale mixture is depicted in Figure 3.1. From the measured data we can see that when clay content increases, porosity decreases and velocity increases up to a given point called the *critical clay content*. This point represents the transition from shaly sands to sandy shales. After this point, porosity increases with increasing clay content, and velocity decreases.

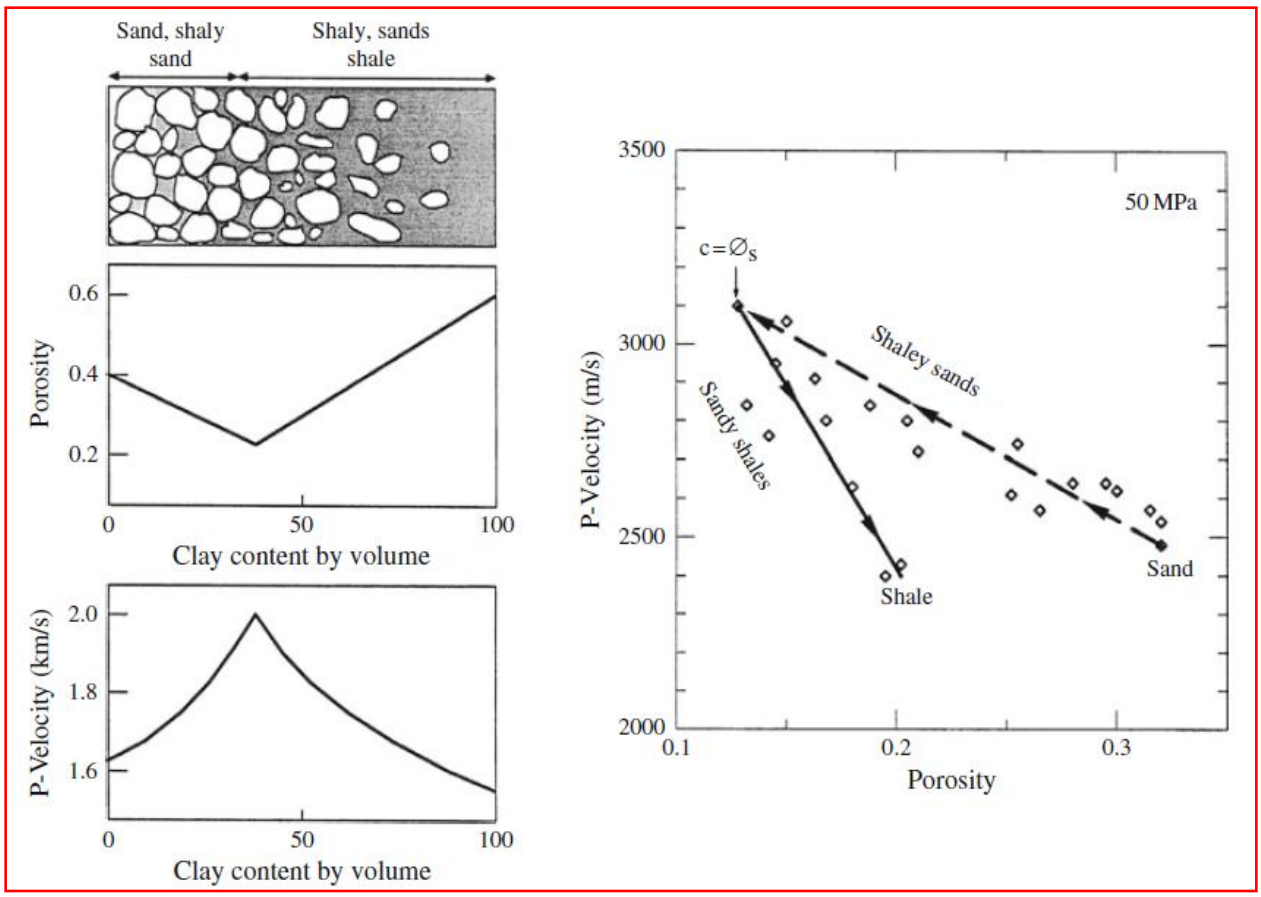

Figure 3.1: The Yin-Marion topological model of porosity and P-wave velocity versus clay content for shaly sands and sandy shales, left. Laboratory experiments (Yin 1992) showing P-wave velocity versus porosity for unconsolidated sands and shales at constant effective pressure of 50 MPa. A clear V-shape trend is observed with increasing clay content, where velocity reaches a maximum and porosity a minimum when the clay content equals the sand porosity, right. (Adapted from Bjørlykke, 2010)

3.2.2 Gas, Oil and Brine properties

Gas properties

Gases are easy to model because the composition and phase behavior have been examined and clearly understood in depth. Gases usually contain alkanes such as methane, ethane and propane. The physical property of a gas is defined by its specific weight, G. G is the relationship between the density of the gas and that of air at 15.6 ºC and 1 atmospheric pressure. Typical values of G lie between 0.56 for methane and over 1.8 for heavy gases (Johansen, 2014). The most important parameters of gas are the formation volume factor, B_g which relates the reservoir volume of free gas to the volume at standard conditions, incompressibility, K_g and density, ρ given by the following relations:

$$K_g \cong \frac{P\gamma^0(P_{pr})}{\left\{1-\frac{(P_{pr})}{Z}\frac{\partial Z}{\partial P_{pr}}\right\}_T}, \rho_g \cong \frac{28.8GP}{Z(T_{pr},P_{pr})RT_a} \text{ and } B_g = \frac{\lfloor V_g \rfloor_{RC}}{\lfloor V_g \rfloor_{STC}} \quad (3.4)$$

where P is pressure, RC is reservoir conditions and STC is standard conditions, P_{pr} is Pseudoreduced pressure, T_a is the absolute temperature, T_{pr} is Pseudoreduced temperature, Z is the compressibility factor, R is a gas constant, $\gamma^0 = func(P_{pr})$ and $Z = func(T_{pr}, P_{pr})$. K_g has units of Pa (N/m^2), ρ_g has units of g/cc and B_g has units of Rm^3/Sm^3.

Density and bulk modulus (Figure 3.2) both parameters increase with increasing pressure. The increase in bulk modulus is strongest though for gases with low temperature. The density increases strongly for lower pressures while it is less dependent on pressure in the high pressure interval. Gas can be compressed or expanded easily since the distance between individual molecules is large; when compressed a greater amount of it can occupy a given volume thereby increasing density and the reverse is true (density is directly proportional to pressure at constant temperature). Figure 3.3 shows the effect of increasing pressure and temperature on viscosity and P-wave velocity of both light and heavy gases. Increased temperature increases and decreases both viscosity and P-wave velocity at lower and higher pressures respectively.

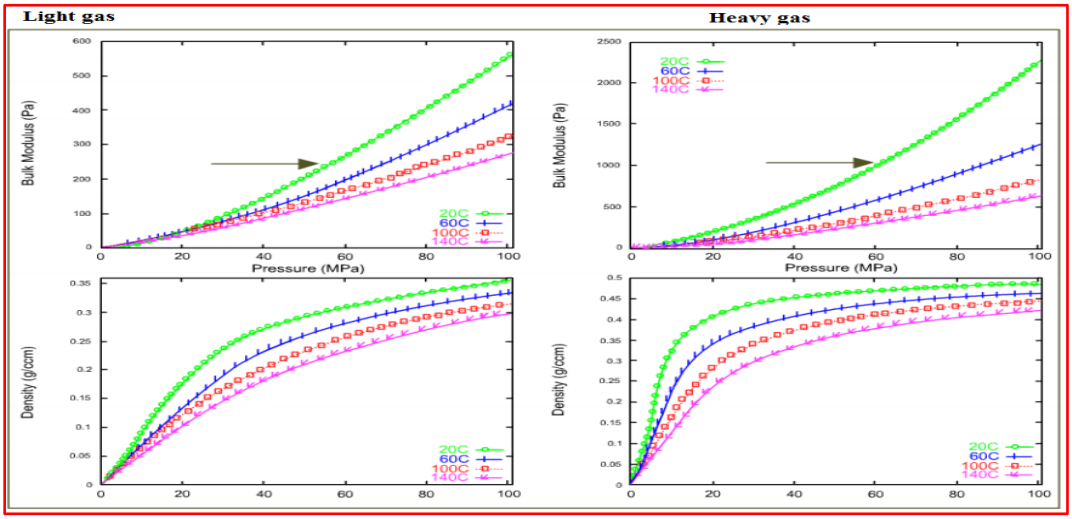

Figure 3.2: Bulk modulus and density of gas versus pressure at different temperatures for both light and heavy gas. Bulk modulus increases with increasing pressure and decreases with increasing temperature. The same trend is observed on density, (figure adapted from Johansen, 2014)

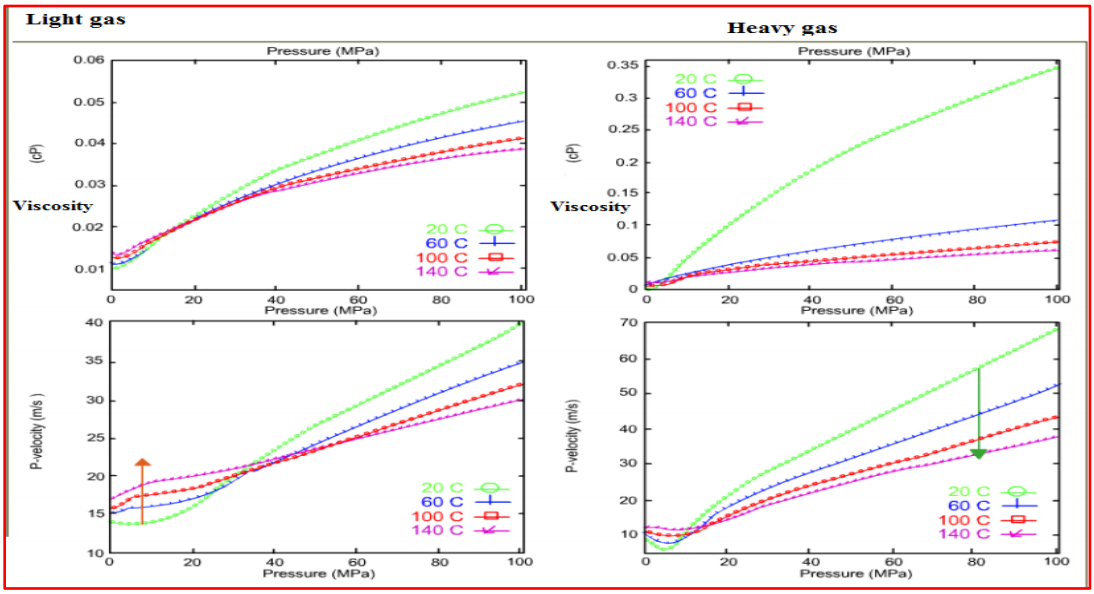

Figure 3.3: Viscosity and P-wave velocity of gas versus pressure at different temperatures for both light and heavy gas. Increased temperature increases and decreases both viscosity and P-wave velocity at lower and higher pressures respectively, (figure adapted from Johansen, 2014)

Oil properties

Analogous to gas, the properties of oil are defined from reference density, ρ_0 which is the density of oil at 15.6 ºC and atmospheric pressure (Johansen, 2014). The properties can also be defined by its API (American Petroleum Institute) number where heavy oils take on API <10 and light oil with API >10. API number is given by:

$$\text{API} = \frac{141.5}{\rho_0} - 131.5 \tag{3.5}$$

The in-situ density can be expressed in terms of pressure effect, ρ_P and the temperature effect, ρ_T. The expression was developed by Dodson and Standing (1945) as noted by Batzle and Wang (1992) and is given as:

$$\rho = \frac{\rho_0 + \left(0.00277\,P - 1.71\times10^{-7}P^3\right)(\rho_0 - 1.15)^2 + 3.49\times10^{-4}P}{0.972 + 3.81\times10^{-4}(T+17.78)^{1.175}} \tag{3.6}$$

P-wave velocity for oil can be expressed as:

$$V_P = 2096\left[\frac{\rho_0}{2.6-\rho_0}\right]^{0.5} - 3.7T + 4.64P + 0.0115[4.12(1.08{\rho_0}^{-1} - 1)^{0.5} - 1]TP \tag{3.7}$$

Thus the oil bulk modulus ($K_O = \rho V_P^2$) can be calculated.

Oil properties are affected by temperature, pressure and other conditions almost in the same way as gas.

Water and Brine properties

Batzle and Wang (1992) noted that, the most common pore fluid is brine. Brine compositions can range from almost pure water to saturated saline solutions. P-wave velocity in water and brine varies relatively little with pressure and temperature. The most important parameter for

brine is salinity, S (is the weight fraction (ppm/1000000) of sodium chloride). Water density, ρ_W and brine density, ρ_B in g/cc are given by the equations below and symbols hold their usual meaning as already defined:

$$\rho_W = 1 + 10^{-6}(-80T - 3.3T^2 + 0.00175T^3 + 489P - 2TP + 0.016T^2P - 1.3 \times 10^{-5}T^3P - 0.333P^2 - 0.002TP^2) \quad (3.8)$$

$$\rho_B = \rho_W + S(0.668 + 0.44S + 10^{-6}(300P - 2400PS + T(80 + 3T - 3300S - 13P + 47PS))) \quad (3.9)$$

Wilson (1959) in Batzle and Wang (1992) provided a relationship for the velocity, V_W of pure water to 100°C and about 100 MPa. Millero et al., (1977) and Chen et al., (1978) also provided additional factors that can be added to the velocity of water to calculate the effects of salinity so that the velocity of brine, V_B can be calculated. The corresponding velocities for water and brine respectively are therefore given by:

$$V_W = \sum_{i=0}^{4}\sum_{j=0}^{3}\omega_{ij}T^iP^j \quad (3.10)$$

$$V_B = V_W + S(1170 - 9.6T + 0.055T^2 - 8.5 \times 10^{-5}T^3 + 2.6P - 0.0029TP - 0.0476P^2) + S^{1.5}(780 - 10P + 0.16P^2) - 820S^2 \quad (3.11)$$

where constants ω_{ij} are as given in Table (A), see Appendix 2.

Bulk modulus ($K = \rho V^2$) can then be calculated.

Figure (3.4) shows how water/brine is affected by salinity, temperature and pressure.

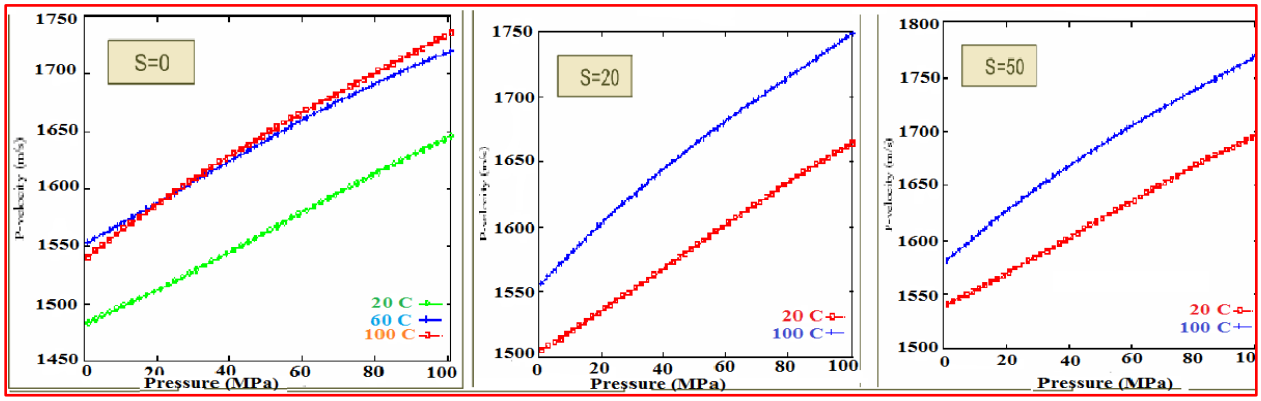

Figure 3.4: P-wave velocity of water/brine versus pressure at different salinities and temperatures. P-wave velocity increases with salinity, temperature and pressure. It can be noted that for S=0, the velocity changes largely for a temperature interval of T=20 ºC to T=60 ºC and almost remains the same from T=60 ºC to T=100 ºC, (figure modified from Johansen, 2014)

3.2.3 Mixed pore fluids: Gas-Brine and Gas-Oil ratios

Batzle and Wang (1992) stressed that gas can also be dissolved in brine and the amount of gas that can go into solution is substantially less than in light oils. Dodson and Standing (1945) in Batzle and Wang (1992), found that the solution's isothermal modulus K_G decreases almost linearly with gas content:

$$K_G = \frac{K_B}{1+0.0494R_{GW}} \tag{3.12}$$

where K_B is the bulk modulus of the gas-free brine and R_{GW} is the gas-water ratio at room pressure and temperature.

The **gas-oil ratio** (R_G) is the ratio of the volume of gas that comes out of solution to the volume of oil at standard conditions. R_G is one of the most important factors controlling seismic response of hydrocarbon saturated rocks. This is through whether oil is live or dead. Live oil contains hydrocarbon compounds that will occur in a gaseous state when brought to the surface ($R_G \neq 0$). Dead oil does not contain gas in solution ($R_G = 0$) and has higher density and velocity values than live oil. When oil is brought to surface conditions it is usual for some natural gas to come out of solution. This affects different seismic properties as summarized in Figure 3.5.

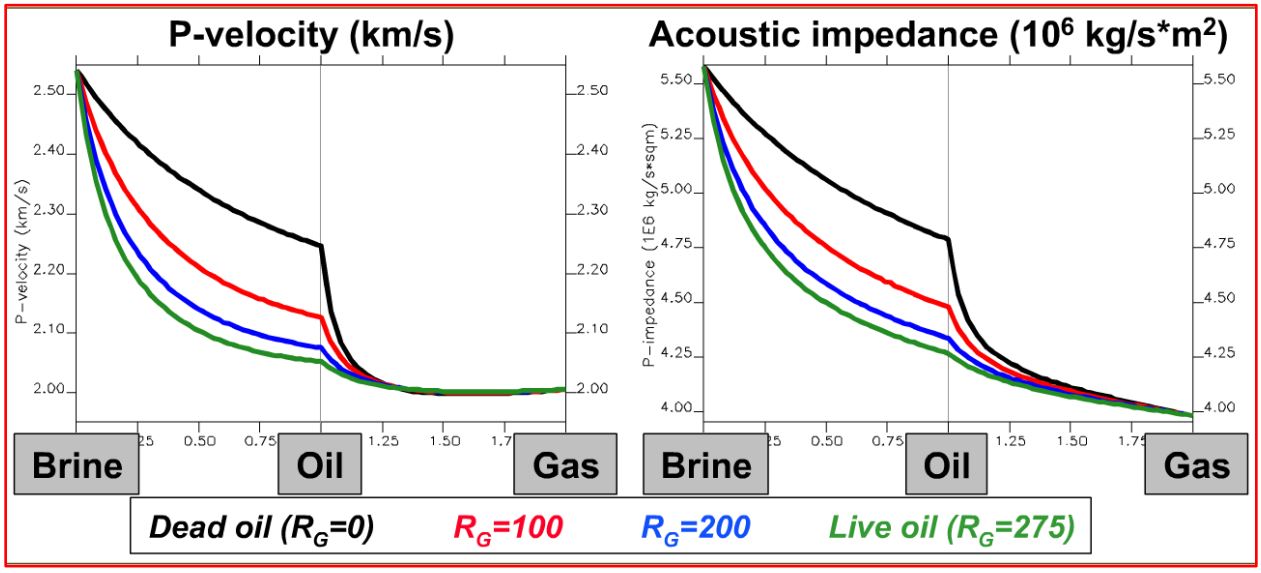

Figure 3.5: Summary of gas-oil ratio effects on P-wave velocity and Acoustic impedance versus fluid composition. Brine has the highest P-wave velocity and P-wave acoustic impedance followed by oil and lowest for gas. It can also be noted that a slight addition of gas in oil causes a dramatic decrease in both the two properties, (Adapted from Johansen, 2014).

3.2.4 Effective and pore pressure effects

Pore pressure (P_p)

This is a function of the weight of the overlying pore fluids and acts in the opposite direction of the confining pressure under normal compaction; this makes the fluid load bearing. Pore Pressure impacts velocities in so many ways; softens the elastic mineral frame by opening cracks and flaws tending to lower velocities. It also has a tendency of making the pore fluid less compressible thereby increasing velocities. Furthermore changing pore pressure can change saturation as gas goes in and out of solution, velocities can be sensitive to saturation changes. High pore pressure persisting over long periods of time can inhibit diagenesis and preserve porosity tending to keep velocities low (Mavko, 2014). Considering a constant fluid density, $\rho_f(z)$ at depth, z, pore pressure is given by:

$$P_p = \int_0^z \rho_f(z) g \, dz \quad (3.13)$$

Confining pressure (P_c)

The external load of the sediment is often denoted as the lithostatic pressure, (P_{Li}) or the confining pressure, (P_c) which is the pressure that acts on the whole volume of the rock. It is given by:

$$P_{Li} = P_c = \int_0^z \rho^*(z) g \, dz \quad (3.14)$$

where $\rho^*(z)$ is the bulk density at depth, *z* and g is the gravitational constant.

Effective Pressure (P_e)

When confining and pore pressures are both increased and become very high, the grains may deform and become smaller. Then there may occur structural changes which may depend on the actual values of P_c and P_p (Unigeo, 2014). Effective pressure takes into account the structural dependence and is given by the equation below:

$$P_e = P_c - P_p \quad (3.15)$$

where P_c and P_p is the confining and pore pressure.

Pressure effects on porosity and pore shapes

Pressure opens and closes very thin cracks and flaws. When pressure increases flat pores and cracks will deform more easily than rounded pores, cracks and fractures may close when sufficiently high pressures are applied. This greatly reduces the porosity and stiffens the rock more thereby increasing velocities but on the other hand permeability of the reservoir rock becomes almost reduced. This reduces both the flow of hydrocarbons within the rock and storage capacity.

3.3 Petrophysics

Well-log data provides a very important information which is helpful in reservoir definition. In this project, well-log data from Yttergryta field in the Norwegian Sea was considered. The gross reservoir interval considered in this project is from 2400-2530 m of measured depth (MD) from kelly bushing (KB). This interval contains hydrocarbons from parts of Garn and Ile formations as shown in the interpretations in Figure 3.6.

3.3.1 Geophysical well-log interpretation

All necessary logs were available and HRS-9 software was used to display the logs. From Figure 3.6, geophysical well-logs were interpreted. Based on gamma ray, shale content (volumetric) and porosity logs, the formations with good porous sands were interpreted as Garn and Ile formations. Further interpretations using neutron porosity and density logs was carried out to identify which hydrocarbons exist in these two formations. Density log when combined with neutron log can provide both quantitative and qualitative interpretations (Rider and Kennedy, 2000) as reflected on the logs in Figure 3.6 with a good separation from Garn, 2416-2447.50 m and in Ile, 2459.0-2519.0 m. These separations indicate presence of hydrocarbons especially gas. Within the same intervals, there is a decrease in P- and S-wave velocities, bulk and shear moduli and Poisson ratio which could be an effect due to presence of gas in the reservoir.

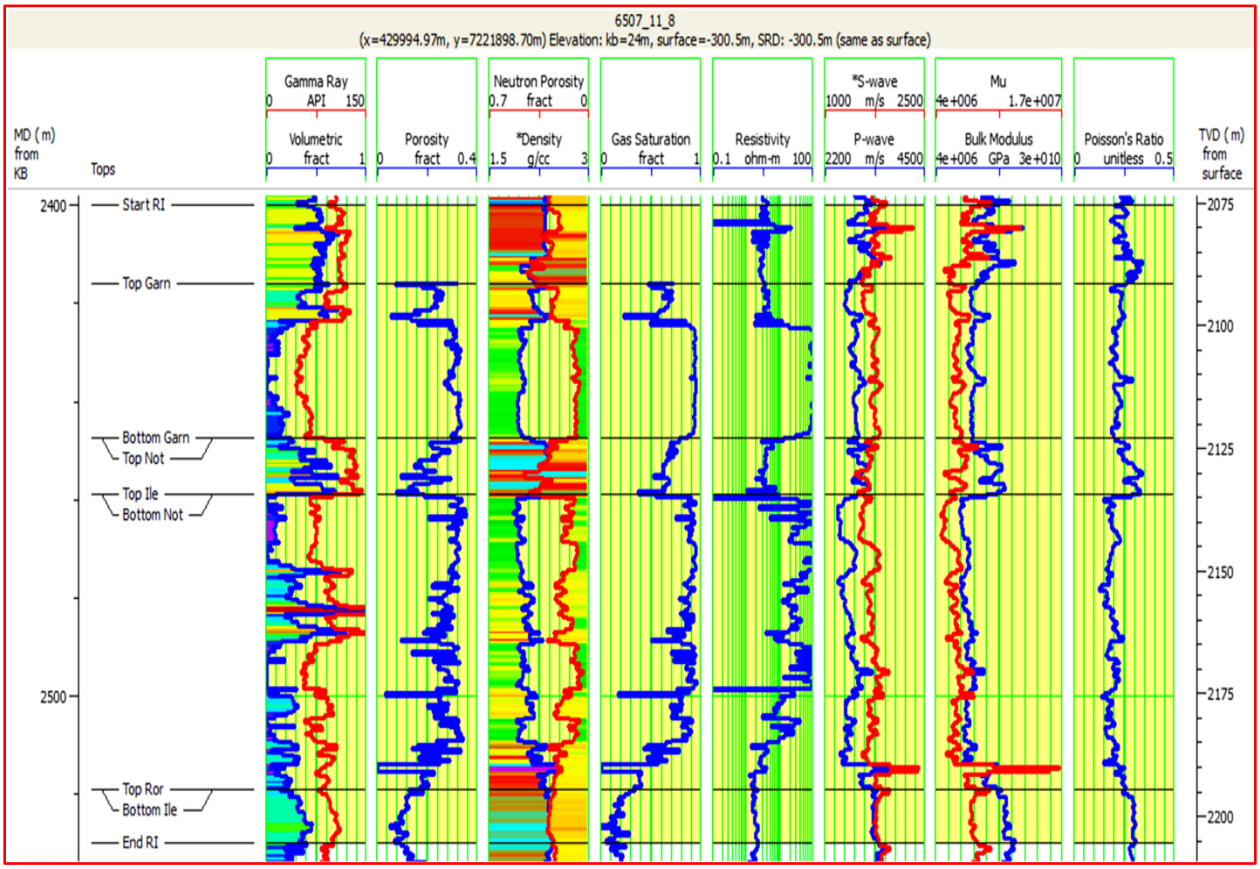

Figure 3.6: The markings (top and bottom) on the well-logs represent different formations' boundaries in the reservoir interval. A good separation between neutron porosity and density logs is an indicator of hydrocarbons. Gas saturation, resistivity and porosity logs are very high within the same intervals, (Garn and Ile formations where hydrocarbons are expected).

3.3.2 Well-log data quality control

Well-log data is subject to different sources of errors which could lead to wrong interpretations. This type of data can be faulty for any number of reasons, the most common of which are poor wellbore conditions (e.g., washouts) and problems with the measurements (e.g., cycle skips on sonic data). Examination of caliper log data is the most common technique for identifying areas in the wellbore that potentially contain bad data. This is especially relevant for density data, as the density tool is a pad type of device and needs to be in contact with the wellbore wall (Smith, 2011).

Because of those known reasons, the caliper log was evaluated first to potentially identify zones with damaged borehole conditions which may affect density readings. The second step was to derive porosity logs (using standard and resistivity method) and compare them with the original porosity log in order to check the correlation as shown in Figure 3.7.

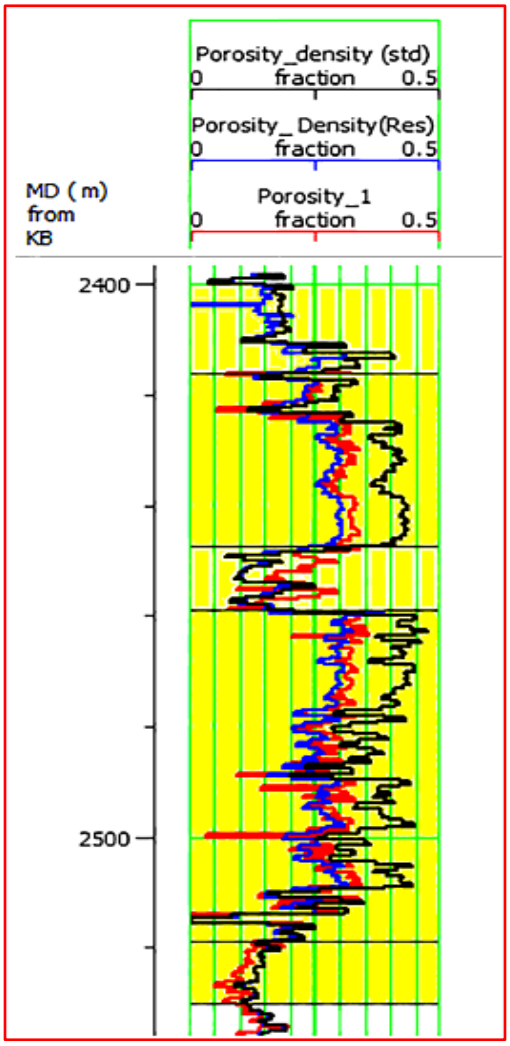

Figure 3.7: Well-log quality control using porosity derived logs from density (black log) and resistivity (blue log) compared with original log (red).Results show a perfect match between the derived porosity log (using resistivity method) and the original log; showing good quality of data and slightly higher values for porosity log derived based on standard method with respect to the original.

3.4 Fluid replacement modeling (FRM)

Fluid substitution is the rock physics problem of understanding and predicting how seismic velocity and impedance depend on pore fluids (Avseth et al., 2005). The pore fluids of a porous permeable rock for over time may be replaced by another pore fluid. It is an important part of seismic attribute work, because it provides the interpreter with a tool for modeling and quantifying the various fluid scenarios which gives rise to an observed amplitude variation with offset (AVO) or 4D responses (Smith, 2011).

3.4.1 The Gassmann's relations (isotropic form) and FRM recipe

Once there changes in reservoir fluids, Gassmann's relations (1951) in equations 3.16 and 3.17 are used for predicting new P- and S-wave velocities and density for the new reservoir conditions. It requires only the bulk modulus of the new fluid mix under the new temperature and pressure conditions. The fluid properties are calculated using the Batzle and Wang empirical relationships (Batzle and Wang, 1992). During fluid substitution there are two fluid effects that must be considered:

- The change in rock bulk density
- The change in rock compressibility (reciprocal of the rock bulk modulus).

$$\frac{K_{sat}}{K_{mineral} - K_{sat}} = \frac{K_{dry}}{K_{mineral} - K_{dry}} + \frac{K_{fluid}}{\emptyset(K_{mineral} - K_{fluid})} \tag{3.16}$$

$$\mu_{sat} = \mu_{dry} \tag{3.17}$$

where K_{fluid} (K_f), K_{dry} (K_d), $K_{mineral}$ (K_o), K_{sat} (K_s) is the pore fluid, dry rock, mineral and saturated rock bulk modulus respectively at porosity, $\emptyset$.

The dry and saturated moduli in turn are related to P-and S-wave velocity.

Equation (3.16) can be re-arranged in the form:

$$K_s = K_d + \Delta K_d \tag{3.18}$$

where $\Delta K_d = \frac{K_o(1-\frac{K_d}{K_o})^2}{1-\emptyset-\frac{K_d}{K_o}+\emptyset\frac{K_o}{K_f}}$ is the increment in bulk modulus caused by fluid saturation.

With a change of fluid saturation from fluid 1 to fluid 2, the bulk modulus increment (ΔK_d) is equal to:

$$\Delta K_{21} \approx \mathrm{G}(\emptyset) * (K_{f2} - K_{f1}) \tag{3.19}$$

where $\mathrm{G}(\emptyset) = \frac{(1-\frac{K_d}{K_o})^2}{\emptyset}$, K_{f1} and K_{f2} are the bulk moduli of fluids 1 and 2 respectively; ΔK_{21} represents the change in the saturation increment that results from substituting fluid 2 for fluid 1. Equation 3.19 uses the fact that the gain function $\mathrm{G}(\emptyset)$ of the dry rock frame remains constant as fluid modulus changes however this may not be true for real rocks. The fluid substitution effect on bulk modulus is simply proportional to the difference of fluid bulk moduli.

Figure 3.8 demonstrates the effects of fluid substitution (brine) on the rock bulk and shear moduli and velocities. Bulk modulus is more strongly sensitive to water saturation. The bulk volume deformation produced by a passing seismic wave results in a pore volume change, and causes a pressure increase of pore fluid (water). This has an effect of stiffening the rock and increasing the bulk modulus. Shear deformations do not produce pore volume change, and differing pore fluids often do not affect shear modulus, (α) as stated in equation 3.17.

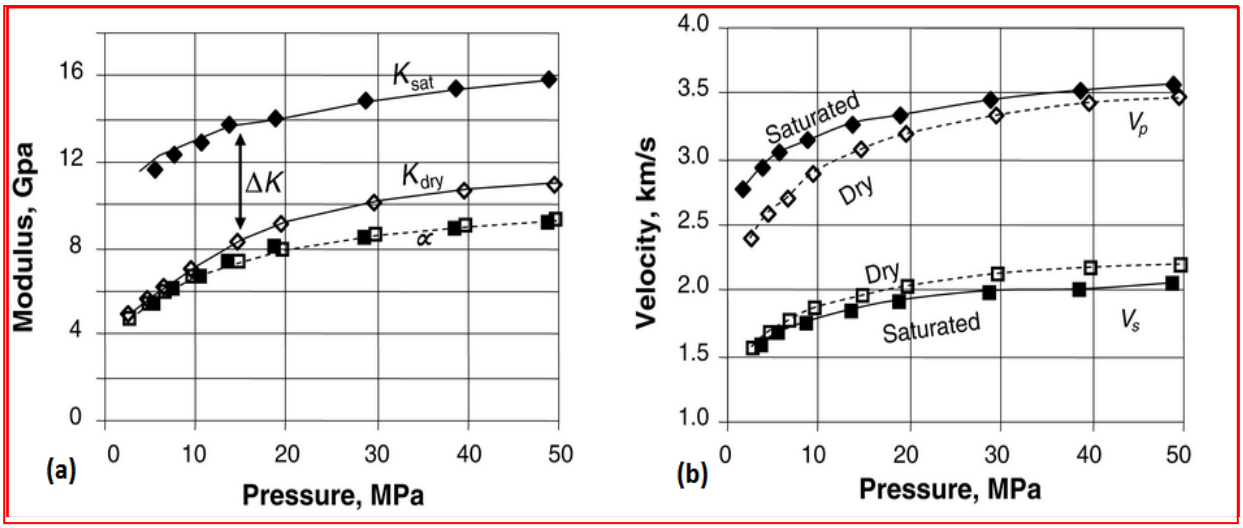

Figure 3.8: A plot of bulk and shear moduli as a function of pressure for dry and brine-saturated sandstone (a), the same sandstone but plotted in terms of Compressional and shear velocity as a function of pressure for dry and brine-saturated sandstone (b), (picture adapted from PetroWiki, 2014).

Gassmann's Assumptions

- Dry bulk modulus does not change with different saturating fluids
- Saturated shear modulus does not change with different saturating fluid
- Porosity does not change with different saturating fluids
- Frequency effects are negligible in the measurements
- Isotropic and homogeneous (single mineralogy) rocks

The Gassmann's Fluid substitution recipe

Gassmann's fluid substitution recipe summarized here is as described in Avseth et al., 2005 where the most common scenario is to begin with an initial set of velocities and densities, $V_p^{(1)}$, $V_s^{(1)}$ and $\rho^{(1)}$ corresponding to the rock with an initial set of fluids, which we call "fluid 1". These velocities often come from well-logs, but might also be the result of an inversion or theoretical model. Then fluid substitution is performed as follows:

Step 1: Extract the dynamic bulk and shear modulus from $V_p^{(1)}$, $V_s^{(1)}$ and $\rho^{(1)}$:

$$K^{(1)} = \rho\left\{(V_p^{(1)})^2 - \frac{4}{3}(V_s^{(1)})^2\right\} \text{ and } \mu^{(1)} = \rho(V_s^{(1)})^2$$

Step 2: Apply Gassmann's relation, equations (3.16) to transform the bulk modulus:

$$\frac{K_{sat}{}^{(2)}}{K_{mineral} - K_{sat}{}^{(2)}} - \frac{K_{fluid}{}^{(2)}}{\emptyset(K_{mineral} - K_{fluid}{}^{(2)})} = \frac{K_{sat}{}^{(1)}}{K_{mineral} - K_{sat}{}^{(1)}} - \frac{K_{fluid}{}^{(1)}}{\emptyset(K_{mineral} - K_{fluid}{}^{(1)})}$$

where $K_{sat}{}^{(1)}$ and $K_{sat}{}^{(2)}$ are the rock bulk moduli saturated with fluid (1) and fluid (2), and $K_{fluid}{}^{(1)}$ and $K_{fluid}{}^{(2)}$ are the bulk moduli of the fluids themselves.

Step 3: Leave the shear modulus unchanged:

$$\mu_{sat}{}^{(2)} = \mu_{sat}{}^{(1)}$$

Step 4: Remember to correct the bulk density for the fluid change:

$$\rho^{(2)} = \rho^{(1)} + \emptyset(\rho^{(2)}{}_{fluid} - \rho^{(1)}{}_{fluid})$$

Step 5: Reassemble the velocities:

$$V_p{}^{(2)} = \sqrt{\frac{K_{sat}{}^{(2)} + \frac{4}{3}\mu_{sat}{}^{(2)}}{\rho^{(2)}}}$$

$$V_s{}^{(2)} = \sqrt{\frac{\mu_{sat}{}^{(2)}}{\rho^{(2)}}}$$

Thus from the Gassmann's fluid substitution recipe the new velocities can be obtained as above.

3.4.2 Fluid mixing models: Homogeneous and patchy saturation

Figure 3.9 shows the two fluid mixing models: homogeneous and patchy fluid saturations and how fluids are distributed. The model considered oil and gas as the pore fluids.

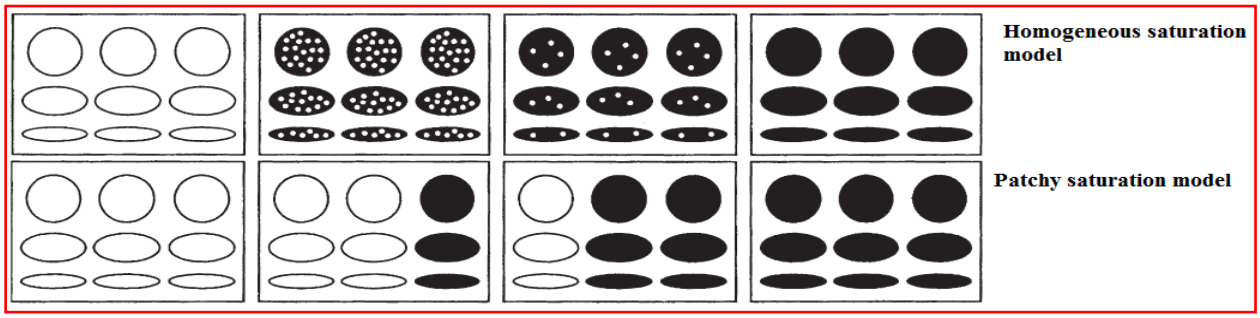

Figure 3.9: Shows a homogeneous fluid mixing model where gas bubbles are gradually formed in the oil (top) and a patchy saturation fluid mixing model where gas is formed in all pores simultaneously (bottom), (modified from Johansen, 2002).

Homogeneous saturation

This type of saturation is characterized by fluids (gas, oil or brine) phases which are mixed uniformly at a very small scale, so that the different wave-induced increments of pore pressure in each phase have time to diffuse and equilibrate during a seismic period (Avseth et al., 2005). In case of homogeneous saturation of *N* fluids, the pore fluid properties are locally represented by

those of an effective fluid (Unigeo, 2013). Wood's equation can then be used to compute the effective fluid bulk modulus $K_f^{(W)}$ as shown below:

$$\frac{1}{K_f^{(W)}} = \sum_{i=1}^{N} \frac{s_i}{K_i} \quad (3.20)$$

where s_i and K_i are the different saturations and bulk modulus for fluid *i*

Patchy saturation

The definition of a patchy saturation is when the two pore fluids occupy different volumes of the pore space, but individually they occupy the same relative fraction of all types of pores, (Johansen et al., 2002). Also in a patchy saturation case (HRS, 2013), the fluids are not uniformly mixed therefore Reuss averaging will not work. Patchy fluid distributions are defined by permeability, fluid viscosity and frequency bandwidth (which is scale dependent: millimeters for logs and meters for seismic). This can happen when porosity is heterogeneous as common in carbonates and also during injection and production displacement processes. Patchy saturation is heterogeneous over scales larger than some critical value (patchy length, L_c) given by:

$$L_c \approx \sqrt{\frac{kK_{fluid}}{f\eta}} \quad (3.21)$$

where *f* is the frequency of the seismic wave, *k* is the permeability, η is the fluid viscosity and K_{fluid} is the bulk modulus of the most viscous fluid phase.

These saturations will have wave-induced pore pressure gradients that can't equilibrate during the seismic period. When the patch sizes are large compared to the seismic wavelength, we use Voigt averaging (Domenico, 1976) whereas when the patch sizes are intermediate in size, one should do a Gassmann's fluid substitution for each patch area and a volume average (Dvorkin et al., 1999a). This can be approximated with the Brie power-law averaging technique to calculate the bulk fluid modulus. Brie et al., 1995 suggested the following empirical mixing law based on the in situ downhole data:

$$K_{fl} = (K_w - K_g)S_w^e + K_g \quad (3.22)$$

where S_w is water saturation, K_g is the bulk modulus of the gas and e is a calibration constant.

Domenico (1977) showed that when e = 1, Brie et al.'s formula is the same as the isostrain (Voigt) average. It can be shown that as the calibration constant (e) increases, patchy saturation tends to homogeneous fluid mixing as shown in Figure 3.10. In this figure, different graphs have been plotted for different values of e =1, 8, 11, 12.

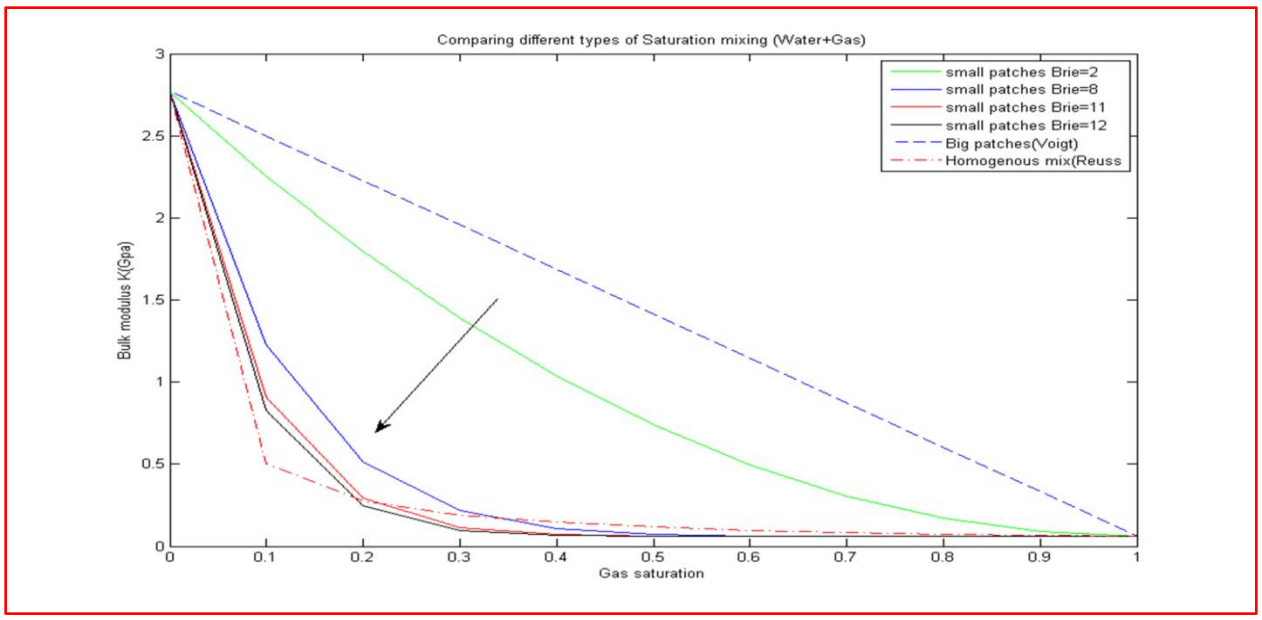

Figure 3.10: Bulk modulus as a function of gas saturation showing the effect of Brie's calibration constant. As *e* increases the patchy saturation approaches the characteristics of uniform (homogeneous) saturation and approaches nearly a uniform saturation at e = 11, 12.

Homogeneous versus patchy saturation effect on seismic velocity

Patchy fluid mixing type (big patches-Voigt) of saturation leads to an effective velocity that is higher than if the saturation was homogeneous or patchy (small patches-Brie, *e*=2). This is because it assumes a stiffer model of mixing, Voigt averaging as shown in the graphs Figure 3.11. This means that before a fluid mixing type is chosen, a good evaluation of the appropriate mixing type is needed.

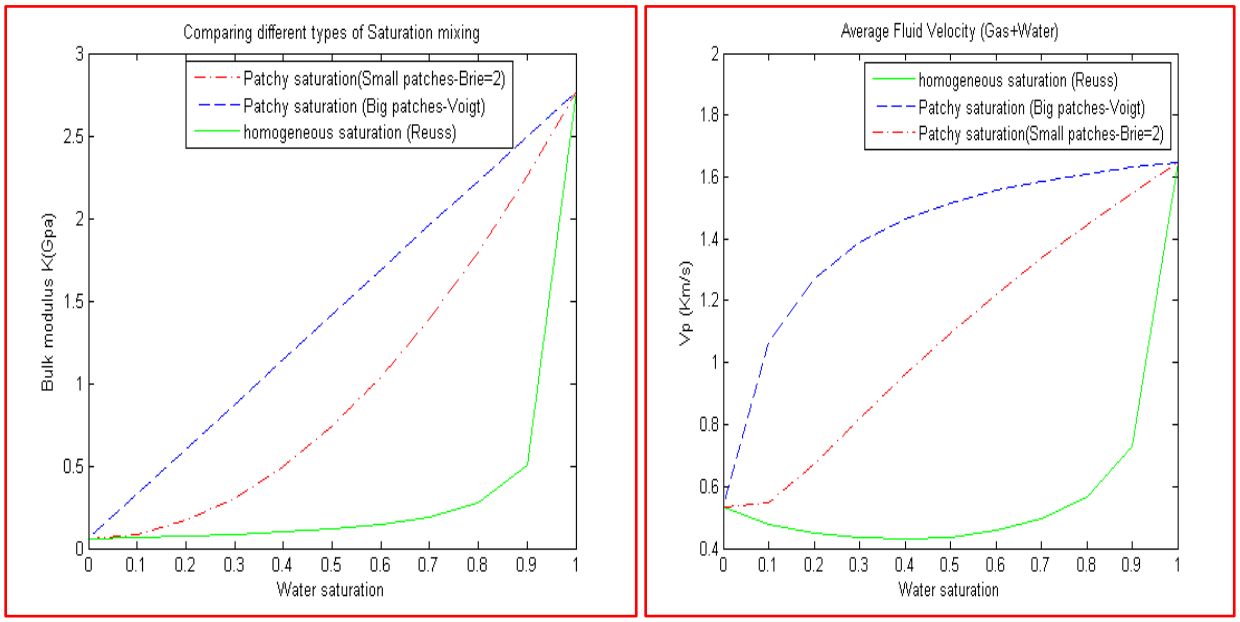

Figure 3.11: Effect of patchy and homogeneous fluid mixing types on velocities. Patchy fluid mixing model increases velocity as it can be seen in blue and red compared to homogeneous mixing (green).

So in this project based on the known trends as in Figure 3.11, the first step was to identify the appropriate mixing type to be used in all the modeling in this project. Using the given data, graphs of bulk modulus and P-wave velocity versus water saturation (Figures 3.12 and 3.13) were plotted.

By comparing the observed trend and the theoretical known trends as shown in Figure 3.11, it was found out that the trend is patchy. A different approach like identifying patchy saturation from well-logs could be used if the trends from the plotted data were not matching with the theoretical ones. A good separation between homogeneous and patchy saturation was noted. Patchy fluid mixing (Voigt) was used in this project.

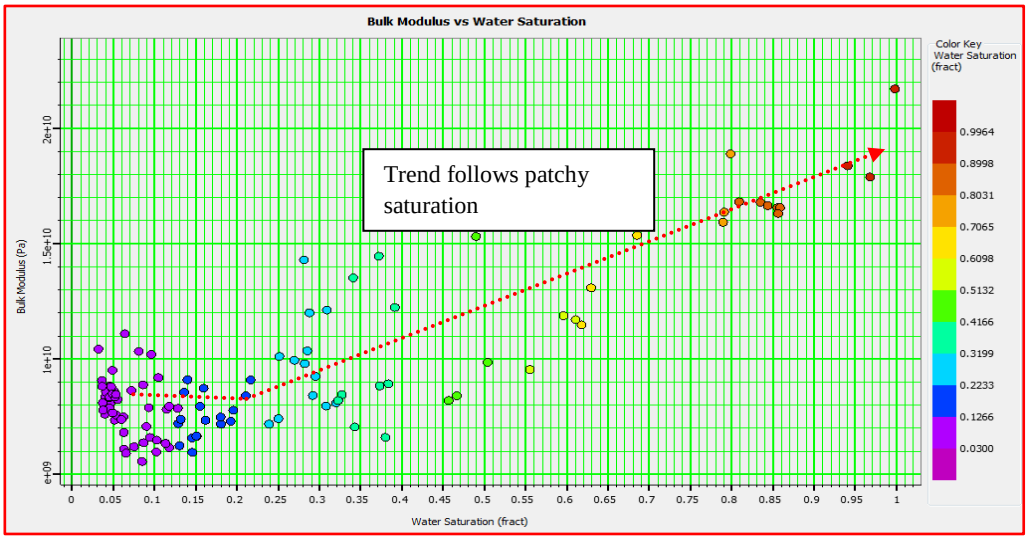

Figure 3.12: Plot of bulk modulus against brine saturation indicating a patchy saturation trend.

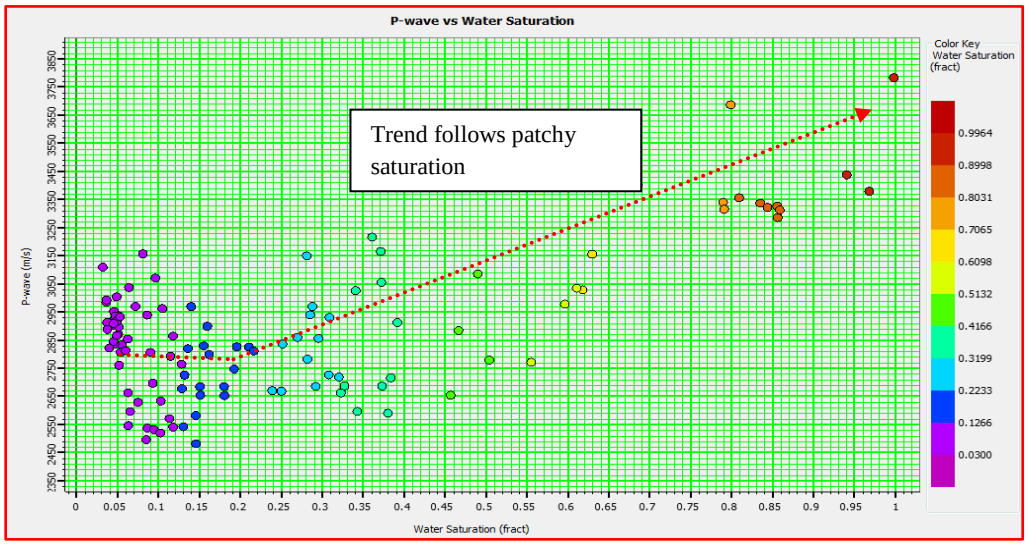

Figure 3.13: Plot of P-velocity against brine saturation indicating a patchy saturation trend.

3.5 Rock physics models for dry rocks

Rock physics is an integrated part of quantitative seismic data analysis and is fundamental for fluid and lithology substitution, for AVO modeling, and for interpretation of elastic inversion results (Avseth and Ødegaard, 2004). This **Section 3.5** is discussed with reference from Avseth et al., 2005.

Elastic Bound Models: (Effective elastic media: bounds and mixing laws)

Elastic bound models provide a useful frame work for velocity-porosity relations (Avseth et al., 2005). Many effective medium models exist and attempt to describe the effective elastic moduli of rocks and sediments. The models among others include; inclusion models, granular–medium models/contact models and others. Regardless of the approach, the models generally need to specify only three (3) types of information:

- The volume fractions of the various constituents (like V_1 andV_2)
- The elastic moduli of the various phases (like K_1 and K_2)
- The geometric details of how the phases are arranged relative to each other.

3.5.1 The Voigt, Reuss and Hill's average models

The simplest but not necessarily the best bounds are the Voigt (1910) and Reuss (1929) bounds. The **Voigt upper bound** on the effective elastic modulus, (M_V) of a mixture of N materials (Avseth et al., 2005) is:

$$M_V = \sum_{i=1}^{N} f_i M_i \qquad \frac{1}{M_R} = \sum_{i=1}^{N} \frac{f_i}{M_i} \tag{3.23}$$

where f_i is the volume fraction and M_i is the elastic modulus of the *i*th constituent.

The Voigt bound is sometimes called the **isostrain average**, because it gives the ratio of average stress to average strain when all constituents are assumed to have the same strain.

The **Reuss lower bound** of the effective elastic modulus, (M_R) is given by the formula in equation (3.23). The Reuss bound is sometimes called the **isostress average**, because it gives the ratio of average strain when all constituents are assumed to have the same stress. Reuss average can be used to describe the effective modulus of a suspension of solid grains in fluid, shattered materials. Figure 3.14 shows the geometric arrangement of the two phases to each other.

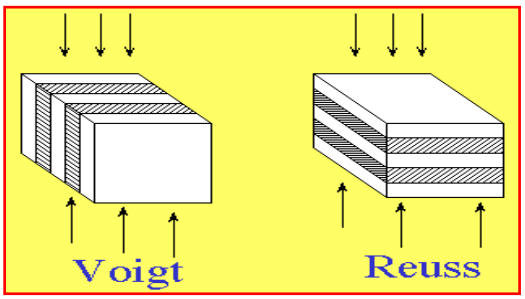

Figure 3.14: Geometric arrangement of the two phases in Voigt and Reuss mixing bounds (from Wisconsin, 2014)

Hill's average model denotes the mean value of both Reuss and Voigt and is given by:

$$M^{(H)} = \frac{1}{2}(M_V + M_R) = \frac{1}{2}\left\{\left(\sum_{i=1}^{N} f_i M_i\right) + \left(\sum_{i=1}^{N} \frac{f_i}{M_i}\right)^{-1}\right\} \tag{3.24}$$

The Voigt-Reuss-Hill average is useful when an estimate of the moduli is needed, not just the allowable range of values (Mavko et al., 2009). It has some limitations and assumptions and these include:

- The result is strictly heuristic. Hill (1952) showed that the Voigt and Reuss averages are upper and lower bounds respectively.
- The rock is isotropic.

3.5.2 Hashin-Shtrikman lower and upper bounds

These are the best bounds for an isotropic elastic mixture. Hashin-Shtrikman bounds give the narrowest possible range of elastic moduli without specifying anything about the geometries of the constituents (Avseth et al., 2005). When there are only two constituents, the bounds are written as:

$$K^{HS\pm} = K_1 + \frac{f_2}{(K_2-K_1)^{-1}+f_1(K_1+\frac{4}{3}\mu_1)^{-1}} \quad (3.25)$$

$$\mu^{HS\pm} = \mu_1 + \frac{f_2}{(\mu_2-\mu_1)^{-1}+2f_1(K_1+2\mu_1)/[5\mu_1\left(K_1+\frac{4}{3}\mu_1\right)]} \quad (3.26)$$

where K_1, μ_1 and K_2, μ_2 are the bulk and shear moduli of the individual constituents 1 and 2, f_1 and f_2 are the respective volume fractions.

Upper and lower bounds are computed by interchanging which material is subscripted 1 and which is subscripted 2, (Avseth et al., 2005). Upper bound is when the stiffest material is subscripted 1 in equations (3.25 & 3.26) and the lower bound when the softest material is subscripted 1 in the same equations.

Figure 3.15 (left) below shows Hashin-Shtrikman coated sphere morphology and the physical interpretation of the upper and lower bounds for the moduli of two phase material. In the same figure (right), is the illustration of elastic bound models for shear modulus with respect to volume fraction; it includes Voigt, Reuss, Hashin-Shtrikman upper and lower bounds.

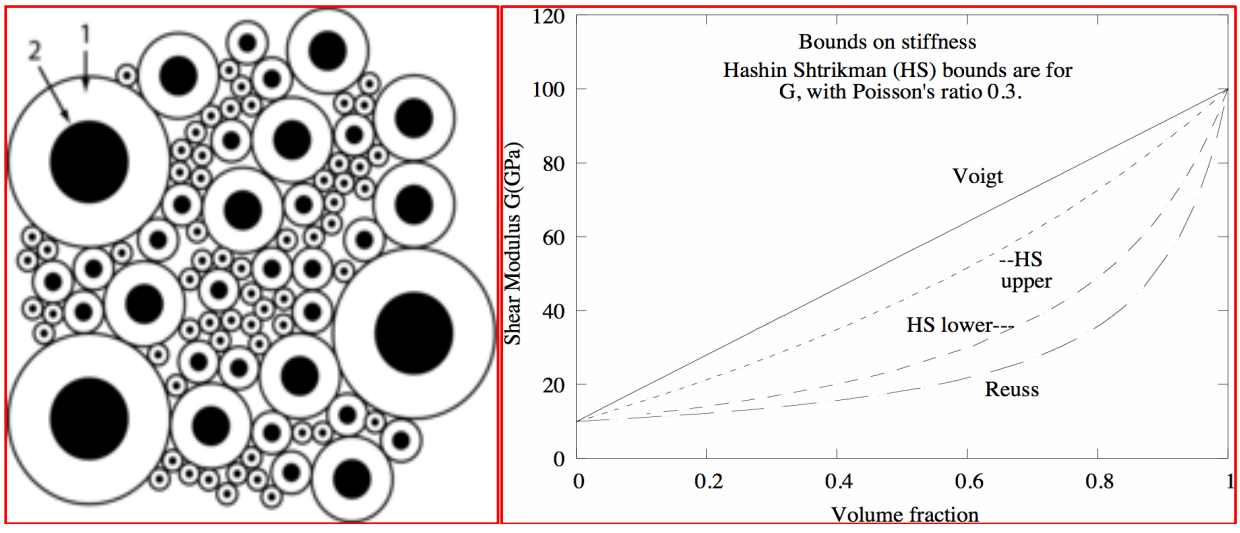

Figure 3.15: Hashin-Shtrikman coated sphere morphology (left), (stiffest-2 and softest-1, adapted from Ferguson and Bazant, 2012) and elastic bound models (right), (adapted from Wisconsin, 2014).

3.5.3 Contact Theory

Hertz-Mindlin theory

The physical foundation of this theory is based on considering a random pack of identical spherical grains. The elastic properties are seen to depend on the contact properties between the grains: contact stiffness, contact area and number of contact points and the elastic properties of the grains and the porosity. The Hertz-Mindlin theory moduli as noted in Avseth et al., 2005 are:

$$K_{HM} = \sqrt[3]{\frac{n^2(1-\emptyset_c)^2\mu^2 P}{18\pi^2(1-\upsilon)^2}} \tag{3.27}$$

$$\mu_{HM} = \frac{5-4\upsilon}{5(2-\upsilon)}\sqrt[3]{\frac{3n^2(1-\emptyset_c)^2\mu^2 P}{2\pi^2(1-\upsilon)^2}} \tag{3.28}$$

where $K_{HM}$and μ_{HM} is the dry rock bulk and shear moduli respectively at critical porosity, $\emptyset_c$ (depositional porosity), P is the effective pressure (difference between the overburden pressure and pore pressure), μ and υ are the shear modulus and Poisson's ratio of the solid phase and n is the coordination number (average number of contacts per grain). The Poisson's ratio can be expressed in terms of the bulk, (K) and shear, (μ) moduli as follows:

$$\upsilon = \frac{3K-2\mu}{2(3K+\mu)} \tag{3.29}$$

The effective pressure versus depth is obtained with the following formula:

$$\text{P=g}\int_0^z(\rho_b - \rho_f)dz \tag{3.30}$$

where g is the gravity constant, ρ_b and ρ_f is the bulk and fluid densities respectively at depth z.

The coordination number (n) depends on porosity (ϕ) as shown by Murphy (1982) according to Avseth et al., 2005. The relationship between coordination number and porosity can be approximated by the following empirical equation:

$$n = 20 - 34\phi + 14\phi^2 \tag{3.31}$$

The Hertz-Mindlin model assumes that the grain aggregate is stable with further loading. Mindlin (1949) also considered the effect of a shear stress when it is applied subsequently to normal stress and assumed that no slip between the grains takes place, and that there is a maximum grain friction (Avseth et al., 2005).

Walton model

Walton (1987) model is another contact theory model expressed in other parameters than those of Hertz-Mindlin model. It assumes that the shear stress is added simultaneously to the normal stress, so giving slightly different results from the Hertz-Mindlin model. Furthermore, the roughness of the grain contacts is considered in two extreme cases, giving it an upper and lower limit for the elastic parameters.

The upper limit is in the case of a very high friction coefficient (very rough grain contacts), giving the effective bulk and shear moduli of a dry package respectively as:

$$K^{(Wa^+)} = \frac{1}{6}\sqrt[3]{\left\{\frac{3(1-\emptyset_c)^2 c_0{}^2 P_c}{\pi^4 B^2}\right\}} \quad (3.32)$$

$$\mu^{(Wa^+)} = \frac{3}{5}K^{(Wa^+)}\frac{5B+A}{2B+A} \quad (3.33)$$

where $\emptyset_c, c_0$, and P_c is the critical porosity, coordination number and confining pressure respectively. For variables A and B see equation set 2.2 in the Appendix 2.

In case of smooth grain contact, the Walton (1987) dry pack bulk and shear moduli respectively are given by:

$$K^{(Wa^-)} = K^{(Wa^+)} = \frac{1}{6}\sqrt[3]{\left\{\frac{3(1-\emptyset_c)^2 c_0{}^2 P_c}{\pi^4 B^2}\right\}} \quad (3.34)$$

$$\mu^{(Wa^-)} = \frac{3}{5}K^{(Wa^-)} \quad (3.35)$$

3.5.4 The friable sand model

From Avseth et al., 2005, the friable-sand model was introduced by Dvorkin and Nur (1996) and these involved two theoretical models for high-porosity sands. The friable-sand model or the "unconsolidated line", describes how the velocity-porosity relation changes as the sorting deteriorates. The "well-sorted" end member is represented as a well-sorted packing of similar grains whose elastic properties are determined by the elasticity at the grain contacts. The "well-sorted" end member typically has a critical porosity, ϕ_c around 40%. The friable-sand model represents poorly sorted sands as the "well-sorted" end member modified with additional smaller grains deposited in the pore space. These additional grains deteriorate sorting, decrease porosity, and only slightly increase the stiffness of the rock.

The elastic moduli of the dry well-sorted end member at critical porosity are modeled as an elastic sphere pack subject to confining pressure. These moduli are given by the Hertz-Mindlin theory as discussed in **Section 3.5.3**. The other end point in the friable-sand model is at zero porosity and has the bulk (K) and shear (μ) moduli of the mineral. Moduli of the poorly sorted sands with porosities between 0 and $\emptyset_c$ are "interporated" between the mineral point and the well-sorted end member using the lower Hashin-Shtrikman (1963) bound.

The Hashin-Shtrikman lower bound is chosen for unconsolidated sands due to the softest component, (the sphere pack) being the load bearing material whilst the solid material introduced in the pore spaces is the stiffest component and is dispersed between the spheres. At porosity, ϕ the concentration of the pure solid phase (added to the sphere pack to decrease porosity) in the rock is $1-\frac{\phi}{\phi_c}$ and that of the original sphere-pack phase is $\frac{\phi}{\phi_c}$. Then the bulk (K_{dry}) and shear (μ_{dry}) moduli of the dry friable sand mixture are:

$$K_{dry} = \left[\frac{\frac{\phi}{\phi_c}}{K_{HM}+{}^{4\mu_{HM}}/_3} + \frac{1-\frac{\phi}{\phi_c}}{K+{}^{4\mu_{HM}}/_3}\right]^{-1} - \frac{4}{3}\mu_{HM} \quad (3.36)$$

$$\mu_{dry} = \left[\frac{\frac{\phi}{\phi_c}}{\mu_{HM}+Z} + \frac{1-\frac{\phi}{\phi_c}}{\mu+Z}\right]^{-1} - Z \quad (3.37)$$

where Z $=\frac{\mu_{HM}}{6}\left(\frac{9K_{HM}+8\mu_{HM}}{K_{HM}+2\mu_{HM}}\right)$

The saturated elastic moduli, K_{sat} and μ_{sat} can now be calculated from Gassmann's equations. The density is given by:

$$\rho_b = \emptyset\rho_{fl} + (1-\emptyset)\rho_{min} \tag{3.38}$$

where ρ_b is the bulk density, ρ_{min} is the mineral density, ρ_{fl} is the fluid density and for dry rocks it is zero.

The P- and S-wave velocities of the unconsolidated saturated sand can then be calculated based on the above information for a known fluid.

3.5.5 The contact-cement model

During burial, sands are likely to become cemented sandstones. This cement may be diagenetic quartz, calcite, albite or other minerals. Cementation has a more rigid stiffening effect because grain contacts are "glued" together. The contact-cement model assumes that porosity reduces from the initial porosity of the sand pack because of the uniform deposition of the cement layers on the surface of the grains (Avseth et al., 2005). The contact cement dramatically increases the stiffness of the sand by reinforcing the grain contacts. The initial cementation effect will cause a large velocity increase with only a small decrease in porosity. Dvorkin et al., 1994 presented mathematical models for the contact-cement model as follows:

$$K_{dry} = n(1-\emptyset_c)M_cS_n/6 \tag{3.39}$$

$$\mu_{dry} = \frac{3K_{dry}}{5} + 3n(1-\emptyset_c)\mu_cS_\tau/20 \tag{3.40}$$

where K_{dry} and μ_{dry} are the effective bulk and shear moduli for the dry rock, respectively; $\emptyset_c$ is the critical porosity and n is the coordination number, S_n and S_τ are variables (given in equation set 2.1, Appendix 2), K_c and μ_c are the bulk and shear moduli of the cement material, respectively; K_s and μ_s are the bulk and shear moduli of the grain material, respectively; $M_c = K_c + 4\mu_c/3$ is the compressional modulus of the cement.

Saturated elastic moduli are then calculated using Gassmann's equations (equations, 3.16 and 3.17). Dry and saturated bulk densities are calculated using equation (3.38). The P- and S-wave velocities of the contact cement saturated sands can then be calculated based on the above information for a known fluid.

3.5.6 The constant-cement model

This model was introduced by Avseth et al., 2000 according to Avseth et al., 2005 and it assumes that sands of varying sorting (and therefore varying porosity) all having the same amount of contact cement. Porosity reduction is solely due to noncontact pore-filling material. This model is a combination of contact cement model, where the porosity reduces from the initial sand-pack porosity to porosity $\emptyset_b$ because of contact-cement deposition, and the friable-sand model where porosity reduces from $\emptyset_b$ because of deposition of the solid phase away from the grain contacts (Avseth et al., 2005). Porosity $\emptyset_b$ is shown in the figure as an open circle (Figure A, see Appendix 2). The equations for this model are given by:

$$K_{dry} = \left[\frac{\phi/\phi_b}{K_b+(4/3)\mu_b} + \frac{1-\phi/\phi_b}{K+(4/3)\mu_b}\right]^{-1} - \frac{4}{3}\mu_b \quad (3.41)$$

$$\mu_{dry} = \left[\frac{\phi/\phi_b}{\mu_b+z} + \frac{1-\phi/\phi_b}{\mu+z}\right]^{-1} - z \quad (3.42)$$

where $z = \frac{\mu_b}{6}\left(\frac{9K_b+8\mu_b}{K_b+2\mu_b}\right)$

ϕ_b is the well-sorted end-member porosity and the respective dry-rock bulk and shear moduli at that porosity are (K_b & μ_b). The remaining parameters carry their usual meaning.

3.5.7 Patchy cemented sandstone model

Avseth et al., 2012 discussed the patchy cemented sandstone model in details. Avseth et al., 2012 noted that the microstructure of patchy cemented sandstones can be represented as an effective medium comprising of a binary mixture of cemented sandstones where all grains contacts are cemented and loose, unconsolidated sands. One approach is to apply the Hashin-Shtrikman model (Mavko et al., 2009) to mix the two constituents in an isotropic manner. The cemented sandstone end-member can be modeled using the Dvorkin-Nur model, whereas the loose sand end-member can be modeled using the Hertz-Mindlin or Walton contact theory. The effective dry rock moduli for patchy cemented high porosity end-member can then be formulated assuming stiffest isotropic mixture according to the Hashin-Shtrikman model (upper bound) as follows:

$$K_{patchy} = K_{cem} + \frac{(1-f)}{(K_{unc}-K_{cem})^{-1}+f(K_{cem}+\frac{4}{3}\mu_{cem})^{-1}} \quad (3.43)$$

$$\mu_{patchy} = \mu_{cem} + \frac{(1-f)}{(\mu_{unc}-\mu_{cem})^{-1}+2f\left[\frac{K_{cem}+2\mu_{cem}}{5\mu_{cem}\left[K_{cem}+\frac{4}{3}\mu_{cem}\right]}\right]} \quad (3.44)$$

where K_{cem} and K_{unc} are the dry rock bulk moduli of cemented rock and unconsolidated rock, respectively; μ_{cem} and μ_{unc} are the ditto dry rock shear moduli; and *f* is the volume fraction of cemented rock in the binary mixture of cemented and unconsolidated rock of the patchy cemented rock. The softest isotropic mixture of the two constituents according to Hashin-Shtrikman formulation is obtained by exchanging the soft and the stiff end members in the equations above, and replacing *f* with (1-*f*).

The next step is to interpolate between the effective high-porosity end member described by equations 3.43 and 3.44 and the mineral point (zero porosity) using a modified lower bound Hashin-Shtrikman to account for varying porosity associated with sorting. The resulting model trends for both stiffest and softest isotropic mixtures are plotted as shown in the Figure 3.16.

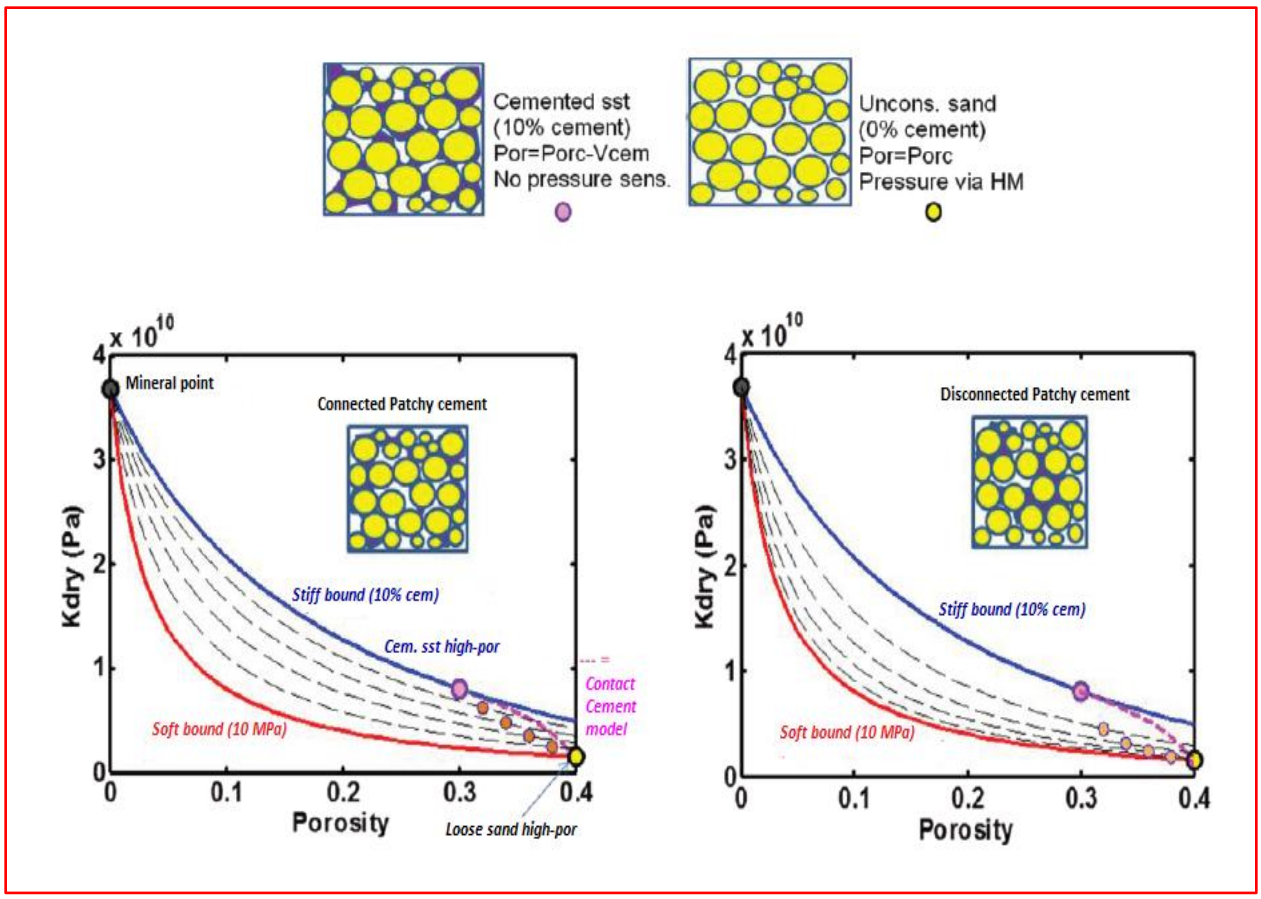

Figure 3.16: Rock physics modeling of patchy cemented sandstone (mixture of 10% cemented sandstone with no pressure sensitivity and unconsolidated sands where pressure is given according to Hertz-Mindlin contact theory, at volume fractions f=0-1, at steps of 0.2). The modeling here is shown for effective pressure of 10 MPa, assuming connected patchy cement (left) and disconnected patchy cement (right), (Slightly modified from Avseth et al., 2012).

3.6 AVO/AVA synthetic modeling

Synthetic modeling is a very useful technique in identifying horizons of interest on seismic data. In 4D seismic surveys, synthetics can be used to quantify the changes in seismic data due to different changes in reservoir properties. Synthetic modeling in most cases requires a flat horizontal layered earth model of known acoustic impedance and known source wavelet.

3.6.1 Acoustic Impedance (Z)

At an interface between two rock layers there is generally a change in propagation velocity resulting from the difference in physical properties of the two layers. When an elastic wave hits such an interface, the energy within the incident wave is partitioned into transmitted and reflected waves. The relative amplitudes of the transmitted and reflected pulses depend on the velocities (v), densities (ρ) and the angle of incidence. Acoustic impedance (Z) is defined as the product between density of a material and the velocity within it and is given by:

$$Z = I = \rho v \tag{3.45}$$

The strength and changes in acoustic impedance with depth in the earth's subsurface determines the seismic amplitudes due to different reflections in seismic data.

3.6.2 The reflection, transmission coefficients and Zoeppritz equations

According to Mavko et al., 2009, at a plane interface between two thick, homogeneous, isotropic, elastic layers, the normal incidence reflectivity for waves travelling from medium 1 to medium 2 is the ratio of the displacement amplitude, A_r of the reflected wave to that of the incident wave, A_i and is given by:

$$R_{12} = \frac{A_r}{A_i} = \frac{I_2 - I_1}{I_2 + I_1} = \frac{\rho_{2V_2} - \rho_{1V_1}}{\rho_{2V_2} + \rho_{1V_1}} \approx \frac{1}{2} ln(\frac{I_2}{I_1}) \tag{3.46}$$

For -1<R<1 and a negative reflection coefficient implies a phase inverse (Sheriff, 1991) as noted in Mavko et al., 2009. The coefficient of reflection indicates the amount of energy reflected.

A normally incident P- and S-wave generates only reflected and transmitted P- and S-waves respectively. There are no mode conversions. The normal transmission coefficient (T) indicates the amount of energy transmitted. Mathematically it is given by the expression:

$$T_{12} = \frac{A_t}{A_i} = \frac{2I_1}{I_2 + I_1} = \frac{2\rho_{1V_1}}{\rho_{2V_2} + \rho_{1V_1}} \tag{3.47}$$

where A_t and A_i are the amplitudes for the transmitted and incident waves respectively.

If the elastic wave is incident at an angle other than 90^0, both reflected P- and S-waves will be generated at the interface between two elastic media. This is called *mode conversion*. However, at a fluid-solid interface like at the sea floor, the shear waves will not exist in the fluid part.

Analysis of AVO, or amplitude variation with offset, seeks to extract rock parameters by analyzing seismic amplitude as a function of offset, or more correctly as a function of reflection angle, (Avseth et al., 2005). The reflection and transmission coefficients for plane elastic waves as a function of reflection angle at a single interface for all these wave conversions are described by the Zoeppritz equations as discussed in Avseth et al., 2005 and given by equation 3.48.

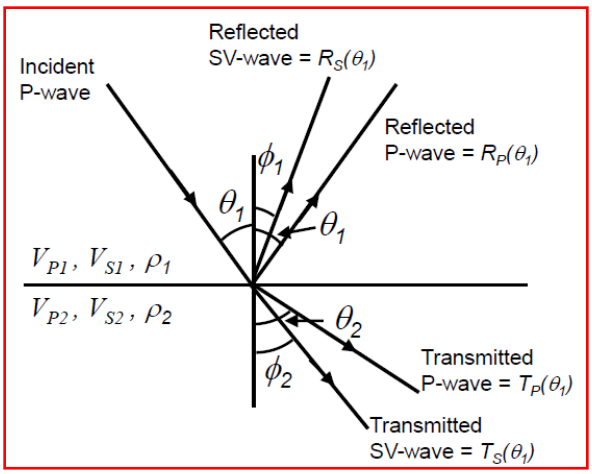

Figure 3.17: Reflection and transmission of obliquely incident rays

Snell's laws also hold and apply to both P- and S-waves for transmitted and reflected waves.

$$\begin{bmatrix} R_P(\theta_1) \\ R_S(\theta_1) \\ T_P(\theta_1) \\ T_S(\theta_1) \end{bmatrix} = \begin{bmatrix} -sin\theta_1 & -cos\emptyset_1 & sin\theta_2 & cos\emptyset_2 \\ cos\theta_1 & -sin\emptyset_1 & cos\theta_2 & -sin\emptyset_1 \\ sin2\theta_1 & \frac{V_{P1}}{V_{S1}}cos2\emptyset_1 & \frac{\rho_2 V_{S2}^2 V_{P1}}{\rho_1 V_{S1}^2 V_{P2}}cos2\emptyset_1 & \frac{\rho_2 V_{S2} V_{P1}}{\rho_1 V_{S1}^2}cos2\emptyset_2 \\ -cos2\emptyset_1 & \frac{V_{S1}}{V_{P1}}sin2\emptyset_1 & \frac{\rho_2 V_{P2}}{\rho_1 V_{P1}}cos2\emptyset_2 & -\frac{\rho_2 V_{S2}}{\rho_1 V_{P1}}sin2\emptyset_2 \end{bmatrix}^{-1} \begin{bmatrix} sin\theta_1 \\ cos\theta_1 \\ sin2\theta_1 \\ cos2\emptyset_1 \end{bmatrix} \quad (3.48)$$

For analysis of P-wave reflections a well-known approximation is given by Aki and Richards, assuming weak layer contrasts (Avseth et al., 2005) as shown below:

$$R(\theta_1) \approx \frac{1}{2}(1 - 4p^2V_s^2)\frac{\Delta\rho}{\rho} + \frac{1}{2cos^2\theta}\frac{\Delta V_p}{V_p} - 4p^2V_s^2\frac{\Delta V_s}{V_s} \quad (3.49)$$

where $p = \frac{sin\theta_1}{V_{p1}}$, $\theta = \frac{(\theta_1+\theta_2)}{2} \approx \theta_1$, $\Delta\rho = \rho_2 - \rho_1$, $\rho = \frac{(\rho_2+\rho_1)}{2}$ and

$\Delta V_p = V_{p2} - V_{p1}$, $V_p = \frac{(V_{p2}+V_{p1})}{2}$, $\Delta V_s = V_{s2} - V_{s1}$, $V_s = \frac{(V_{s2}+V_{s1})}{2}$

In the above formulas, p is the ray parameter, θ_1 and θ_2 is the angle of incidence and transmission; V_{p1}, V_{p2} and V_{s1}, V_{s2} are the P-wave and S-wave velocities above and below a given interface of densities ρ_1 and ρ_2 respectively (Figure 3.17). The approximation given by Aki and Richards can be further approximated (Shuey, 1985):

$$R(\theta) \approx R(0) + Gsin^2\theta \quad (3.50)$$

where $R(0) = \frac{1}{2}\left(\frac{\Delta V_p}{V_p} + \frac{\Delta\rho}{\rho}\right)$, $R_s = \frac{1}{2}\left(\frac{\Delta V_s}{V_s} + \frac{\Delta\rho}{\rho}\right)$, $G = \frac{1}{2}\left(\frac{\Delta V_p}{V_p} - 2\frac{\Delta V_s}{V_s} - \frac{\Delta\rho}{\rho}\right) = R(0) - 2R_s$

The Zero-offset reflectivity $R(0)$ is controlled by the contrast in acoustic impedance across an interface. The gradient, *G*, is more complex in terms of rock properties, but from the expression (Avseth et al., 2005), it shows that it depends not only on the contrasts in V_p and density but also V_s.

3.6.3 Synthetic seismogram

A synthetic seismogram is the result of forward modeling the seismic response of an input earth model (defined in terms of variations in physical properties). In hydrocarbon exploration this is used to provide a 'tie' between changes in rock properties in a borehole and seismic reflection data at the same location.

In this project Hampson Russell Suite (HRS-9/R-1.6.1) through 'Create AVO Synthetics' module was used to compute the corresponding AVA synthetics. The modeling options used are as below:

- Pre-stack synthetics
- Computing using Zoeppritz equations
- Angle type of synthetics, number of angles =10, Near =5 and far =30 degrees
- Ricker wavelet of 25 HZ (assumed) and zero phase, Figure 3.18 (right)
- Assuming no transmission losses or geometric spreading or no noise added

The Seismic trace, $T(t)$ (Figure 3.18, left) is then computed as:

$$T(t) = R(t) * W(t) \tag{3.51}$$

where $R(t)$ is the reflection coefficient series as a function of two way travel time (TWT) for a seismic wave in the media convolved (*) with a source wavelet $W(t)$.

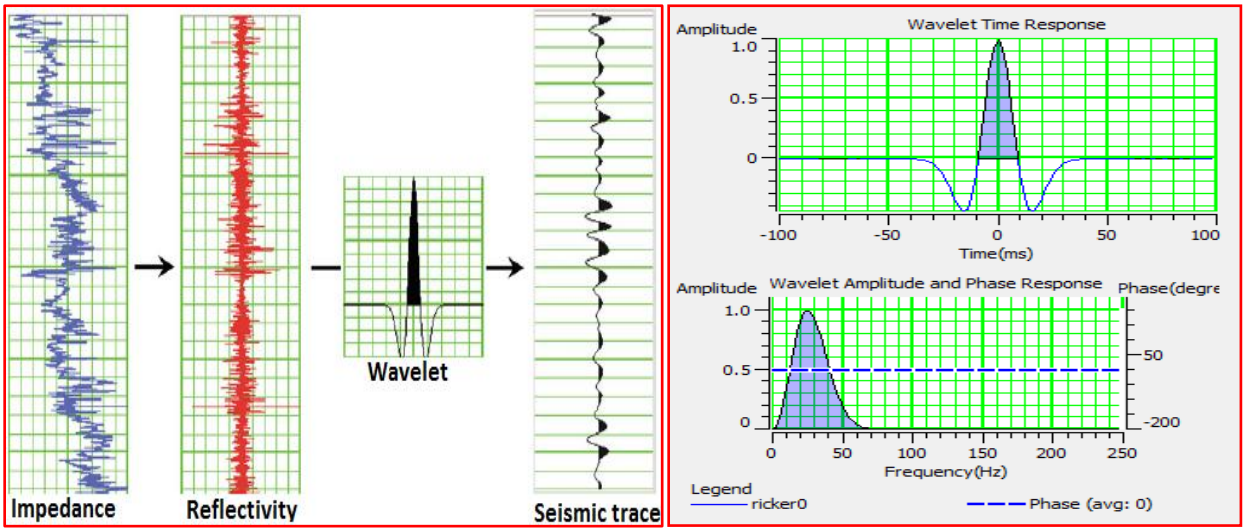

Figure 3.18: Seismic trace is a result of convolution of a wavelet and the reflectivity series plus noises (left, Adapted from Bjørlykke, 2010). A 25 Hz Ricker wavelet (right) used in this project in the modeling of AVA synthetics

3.7 Summary

This Chapter has shown how seismic wave velocities change under different pore fluid conditions, petrophysics including geophysical well-log interpretations have also been discussed. The Chapter has covered effects of different saturating pore fluids on rock properties, and rock physics models for dry rocks that predict the rock elastic moduli from given reservoir properties. Finally, the Chapter comes to an end with AVO/AVA theory.

4.0 Rock Physics Template (RPT) methodology

4.1 Introduction

Rock physics templates are locally constrained charts of rock physics models for prediction of lithology, porosity and fluids (Avseth et al., 2005). The technology of RPTs was first presented by Ødegaard and Avseth (2003).

RPTs are field specific and honor local geological factors. Geologic constraints on rock physics templates include; lithology, mineralogy, burial depth, diagenesis (cementation), pressure and temperature. In general it is essential to include only the expected lithology for the area under investigation when generating the templates (Avseth et al., 2005). The most common form of RPT is between Vp/Vs and P-wave acoustic impedance (AI) as a combination of these two is a good lithology and fluid indicator (Avseth et al., 2005; Chi and Han, 2009). Other forms of RPTs may include plots of AI, SI, EI, and Lame's parameter, Lambda-Rho, Lambda-Mu, Mu-Rho and others. There are two types of RPTs: **static** and **dynamic** rock physics templates.

4.2 Rock physics template forward modeling

In the modeling of an RPT (Avseth et al., 2005), the first step is to calculate velocity-porosity trends for the expected lithology for various burial depths. This is followed by application of Hertz-Mindlin contact theory to calculate the pressure dependency at the high porosity end member. The other end point is at zero porosity and has the bulk and shear moduli of the solid mineral.

These two points in the porosity-moduli plane are then connected with a curve given by the modified Hashin-Shtrikman bounds. This can be bulk and shear moduli for the mixture of two phases, original porous phase and the added solid phase. Porosity reduction related to packing and sorting, where small grains enter the pore space between larger grains, is modeled by the lower bound. For cemented rocks, we can either apply Dvorkin-Nur's cement model or the Hashin-Shtrikman upper bound model.

The next step is to calculate the elastic bulk moduli of brine- and hydrocarbon- saturated rocks to see the effect of fluid substitution. The dry rock properties calculated from the combined Hertz-Mindlin and Hashin-Shtrikman model are used as the inputs into Gassmann's equation to calculate the saturated rock properties assuming either uniform or patchy saturation. From these, P- and S-wave velocity and density of brine or gas saturated rocks can be calculated. Finally AI and Vp/Vs can be computed so that a cross plot of Vp/Vs against AI can be plotted. The simplest work flow and summary is as follows in Figure 4.1.

It is important to note that during this modeling process of an RPT we need to know different acoustic properties of formation water and hydrocarbons in the area of investigation. These properties include; pressure, temperature, brine salinity, gas gravity, oil reference density (API) and gas-oil ratio (GOR).

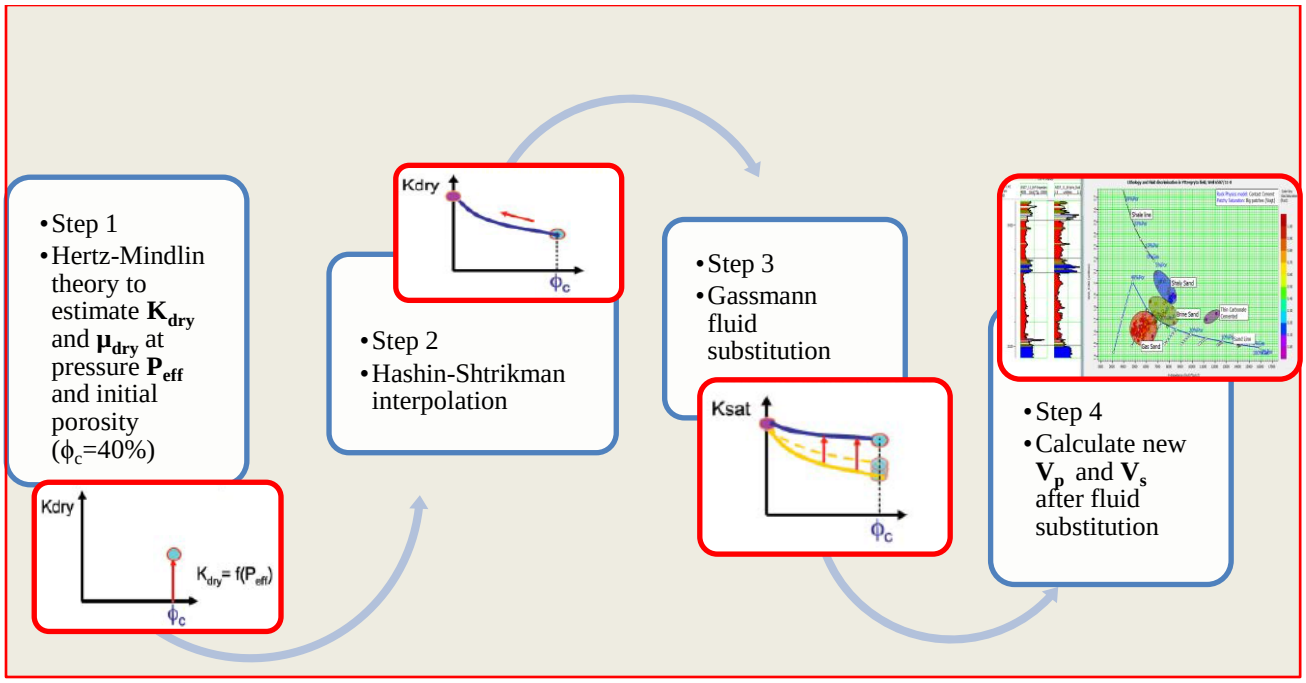

Figure 4.1: Rock physics template work flow, (Small graphs modified from Avseth, 2009)

4.3 Static Rock Physics Templates

Static RPTs relate elastic properties of AI and Vp/Vs of the producing reservoir at fixed time in its life history. A general RPT of Vp/Vs versus AI can be presented as follows in Figure 4.2:

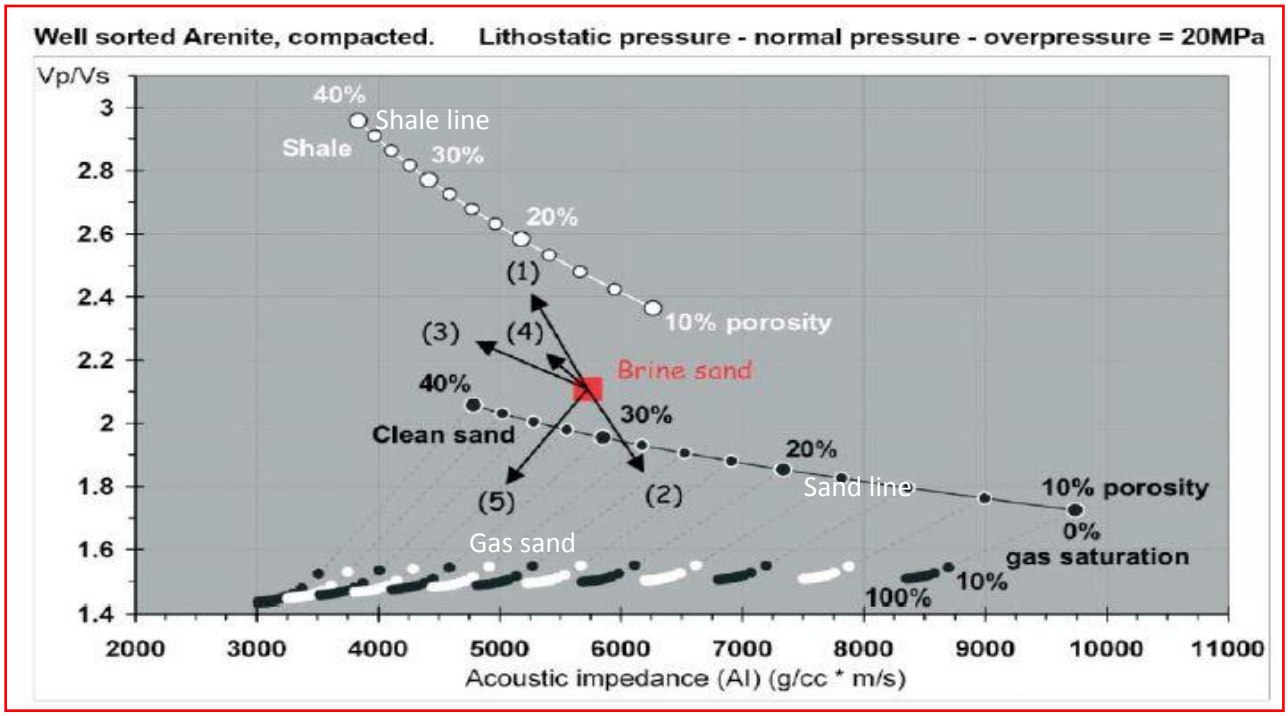

Figure 4.2: A rock physics template in the Vp/Vs versus AI cross-plot domain includes a rock physics model assuming uniform saturation. The black arrows show increasing: shaliness (1), cement volume (2), porosity (3), pore pressure (4) and gas saturation (5), (Adapted from Avseth and Ødegaard, 2004).

4.4 Dynamic (4D) Rock Physics Templates

Dynamic RPTs relate the relative changes in AI and Vp/Vs of the reservoir that are related to pore pressure and fluid saturation changes in its production life history. Here the predicted changes in pressure and saturation are displayed as a graduated template in a 4D attribute cross-plot to aid the interpretation of time-lapse results, (CGG, 2014).

In the same way as for static rock physics templates (RPTs), we use a given rock physics model and fluid substitution theories for different scenarios of change. The template has three variable parameters: porosity, pressure and saturation, where one or two are kept constant (in this project and in Figure 4.3, porosity is constant). We use the ratio of change rather than the 4D differences in order to fit the domain for the 4D RPT (Andersen et al., 2009) as described below. These changes in properties are given by:

$$AI_{change} = \frac{I_{P,monitor}}{I_{P,base}} \tag{4.1}$$

$$\left[\frac{V_p}{V_s}\right]_{change} = \frac{\left[\frac{V_p}{V_s}\right]_{monitor}}{\left[\frac{V_p}{V_s}\right]_{base}} \tag{4.2}$$

The 4D RPT in Figure 4.3 (left) relates two scenarios (base and monitor) for fluid and pressure changes in a reservoir. The RPT on right only shows how saturation and pressure changes but does not relate two scenarios unless the two scenarios have been plotted on the same template. In this project, the RPT on right was used other than the one on left because no scenarios of pressure and saturation changes were modeled. The models which matched the dataset were very insensitive to pressure changes. Pore pressure, effective pressure and confining pressure have been discussed in **Section 3.2.4.**

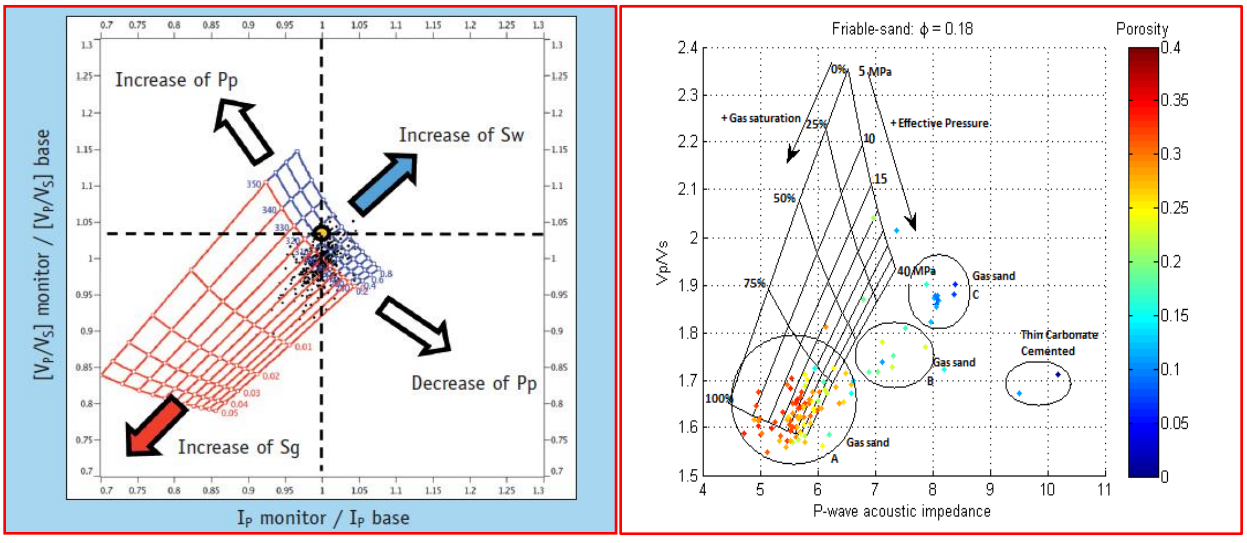

Figure 4.3: 4D RPTs in different cross-plot domains as shown above, pore pressure (P_p) and gas saturation (Sg) decrease in the direction of increasing effective pressure and brine saturation (Sw) respectively. The 4D RPT (right) was constrained at a constant porosity of 0.18. For the 4D RPT (left), the initial oil reservoir conditions are: Porosity= 0.3, Pp = 300 bar, Sw = 0.2, oil saturation (So) = 0.8, Sg = 0, (Figure on left was adapted from CGG, 2014).

The validity of the 4D RPT depends on the validation of the static RPT, as the dynamic template is derived directly from it (Andersen et al., 2009).

4.5 Homogeneous versus patchy saturation effect on a rock physics template

Application of Gassmann's equation usually assumes that all fluid phases are immiscible and homogeneously distributed throughout the pore space (homogeneous saturation). These assumptions are thought to be satisfied in systems which have come to equilibrium over geologic time. However, this equilibrium distribution of phases may be disturbed during drilling, production, and water flooding and the return to equilibrium may require time frames longer than those encountered during logging or between seismic surveys used in 4Dmonitoring (Smith, 2003).

Thus, it is reasonable to expect that fluids might not be homogeneously distributed throughout the pore space in a reservoir or borehole (Brie et al., 1995). Furthermore, in water-wet rock, water is preferentially drawn into the smaller size pores and cracks, leaving the larger voids or pores preferentially occupied by the hydrocarbons. This may lead to a segregation of phases and, perhaps more importantly, the inability of pore pressures to equilibrate in the time scale of wave propagation. Thus, conditions can and probably do exist where water and hydrocarbon distribution are not uniform and the application of the Reuss average for fluid mixture properties is inadequate. This class of nonuniform phase distributions is referred to as "*patchy saturation*" (Smith, 2003).

Homogeneous fluid distribution gives a famous effect where residual amounts of gas will cause almost the same seismic properties as the commercial amounts (Avseth et al. 2005). Thus this indicates that homogeneous distribution on an RPT is not a good indicator of small fluid saturation changes which would match exactly a given fluid substituted data. Also it means that it is hard to see the difference if one fluid is gradually replaced by another, Figure 4.4 (left).

Patchy saturation (big patches-Voigt) unlike homogeneous saturation gives a more linear change in seismic properties with increasing gas saturation (Avseth et al. 2005) as shown in Figure 4.4(right). Because of these differences and evaluation made previously between the two mixing types, in this project patchy fluid mixing type (Voigt) was used in the modeling of RPTs.

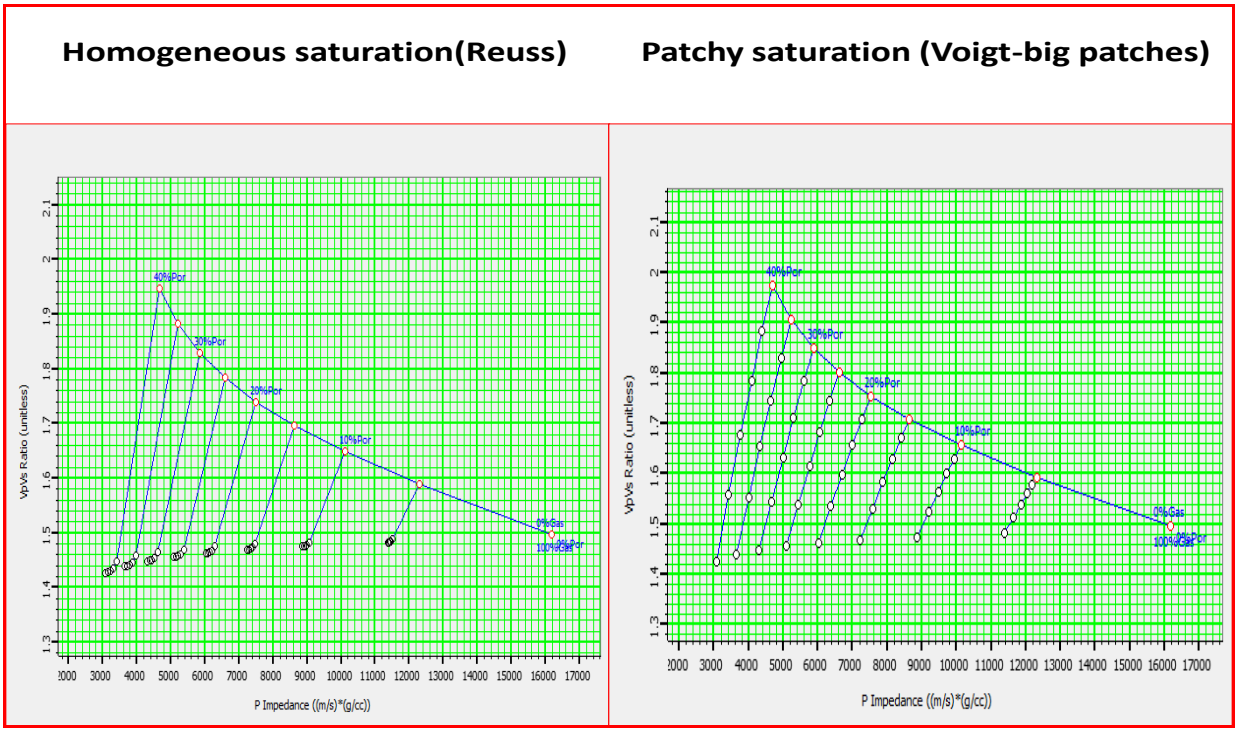

Figure 4.4: RPTs in a Vp/Vs versus AI cross-plot domain includes unconsolidated sand rock physics model, plot based on homogeneous fluid mixing (Reuss) and patchy saturation using big patches (Voigt or Brie constant=1)

4.6 Summary

In this Chapter, the method of RPTs (both static and dynamic RPTs) that has been used in this project in reservoir characterization of the data has been introduced and explained. The Chapter also has covered the effects from different fluid mixing models on the RPTs and how they may affect the sensitivity of the data, Figure 4.4. The fluid mixing type used in this project was taken to be patchy saturation-big patches (Voigt).

5.0 Reservoir characterization on data

5.1 Introduction

P- and S-wave velocity, density and other derived attributes were used to give information about the lithology, fluids and porosity for this study field. Several cross plots are presented in this Chapter using different attributes and rock physics models. The simplest work flow for reservoir characterization on data in this project is as follows in Figure 5.1.

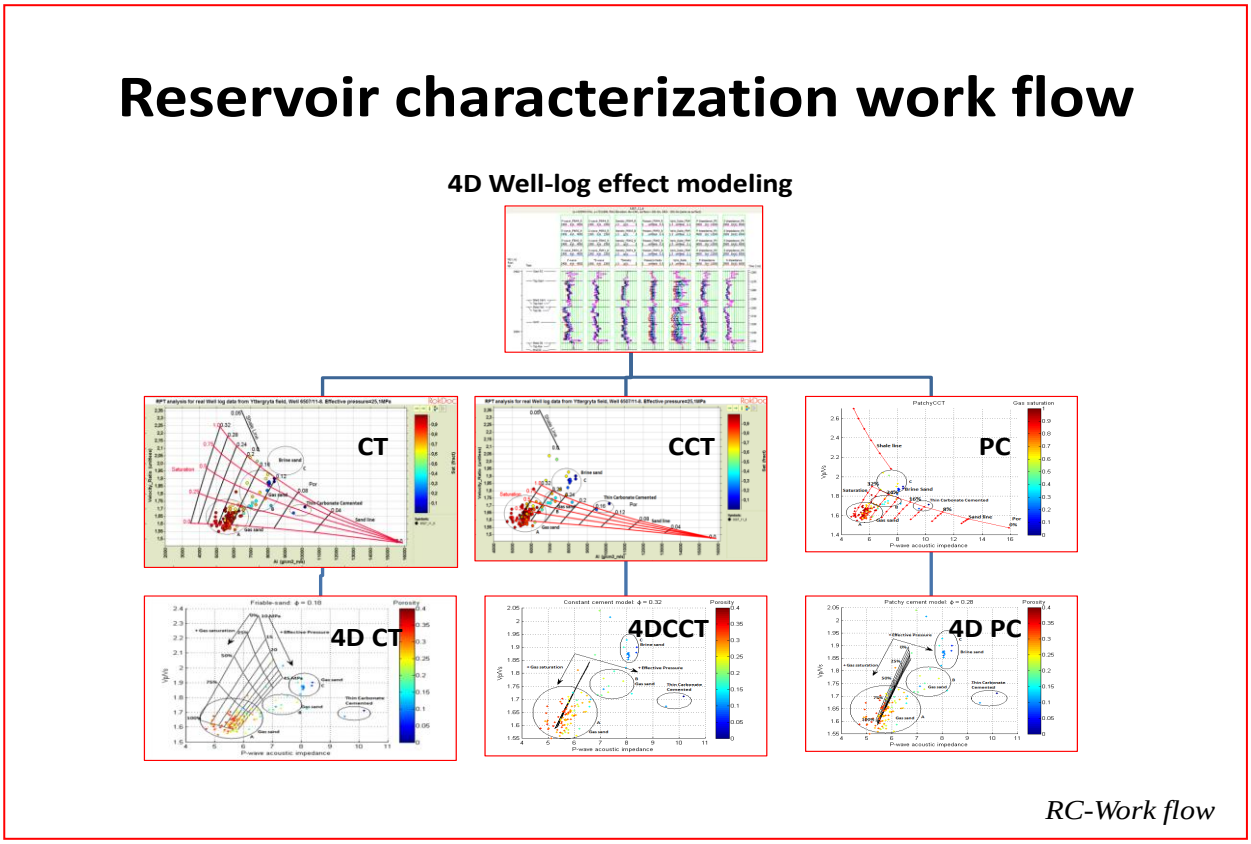

Figure 5.1: Reservoir characterization (*RC*) work flow on real well-log data using both static and dynamic rock physics templates based on different rock physics models (contact theory-CT, constant-cement theory-CCT and patchy cemented sandstone-PC).

5.2 Fluid-lithology detection and discrimination

During reservoir characterization, the first step was to discriminate between fluids and lithology in this field. This was done through cross-plotting by combining P- and S-wave velocities and density.

5.2.1 Using P- and S-wave velocity cross-plot

P- and S-wave velocity information is a good direct hydrocarbon detection method. In spite of the many competing parameters that influence velocities, the nonfluid effects on P- and S-wave velocities are similar (Avseth et al., 2005). Variations in porosity, shaliness, and pore pressure move the data up and down along the same trend, while changes in fluid saturation move data from one trend to another (Avseth et al., 2005). This was important in giving information on which formations contain hydrocarbons as illustrated in Figure 5.2.

The cross-plot points in Figure 5.2 are color-coded using the gas saturation log; the P- and S-wave logs (in curve display) are color-coded based on the two zones (gas and brine sands) defined in the cross-plot domain. These two distinct zones of data are separated following different trends which are perpendicular. The data in a red zone shows gas sands and the blue zone shows brine sands. By validating the cross-plot using well-logs, the two zones of data show that gas is found in Garn and Ile formations whereas brine is in the Ror formation and some in the Not formation.

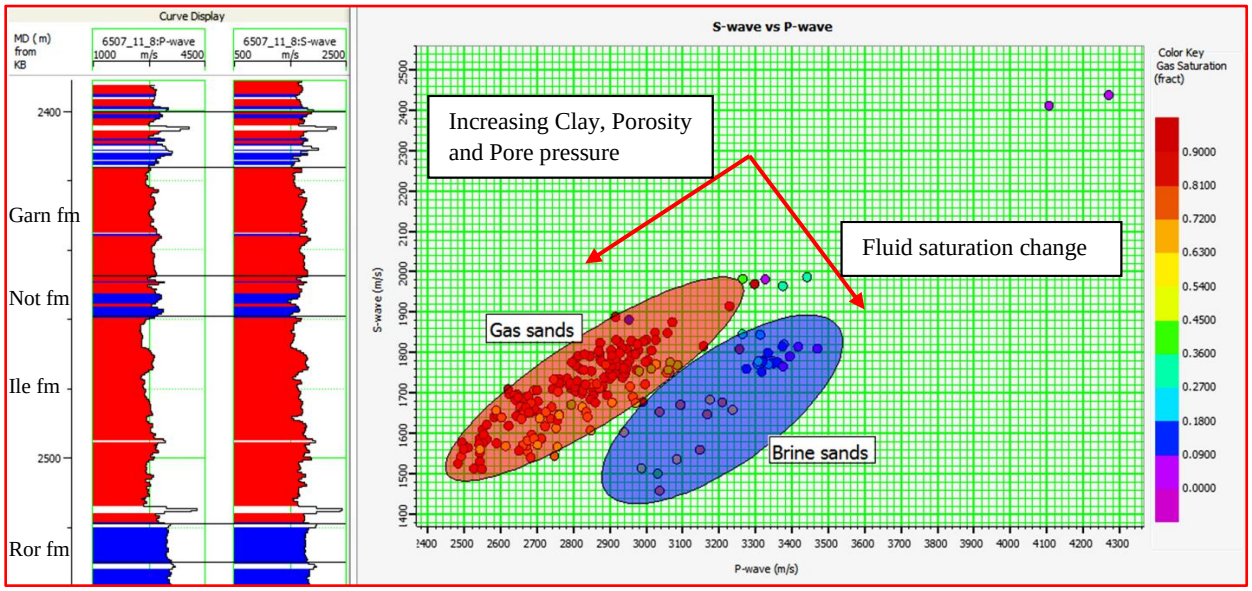

Figure 5.2: A cross-plot of S-wave (Vs) versus P-wave (Vp) velocities for water and gas-saturated sands. A significant separation between gas (red) and brine (blue) sands has been identified (Vp-Vs magic for direct hydrocarbon detection). The trend for saturation is perpendicular to that for porosity, clay and pore pressure as shown by the arrows.

5.2.2 Using P- and S-wave acoustic impedance cross-plot

The Figure 5.3 shows how different zones are separated due to different fluids and lithology.

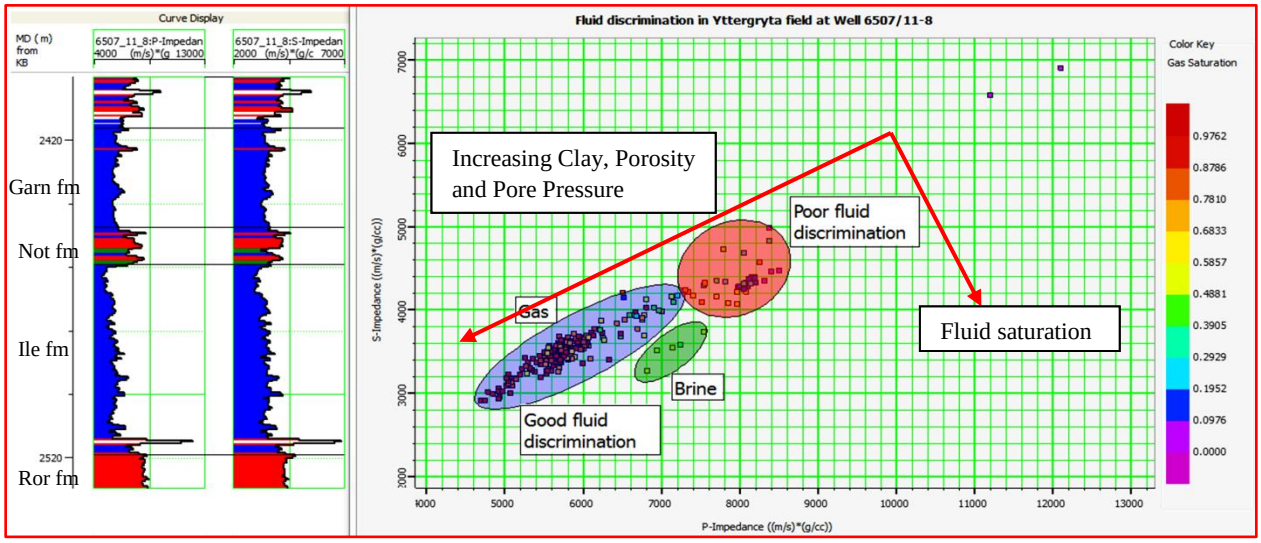

Figure 5.3: A cross-plot of S-wave against P-wave impedances for hydrocarbon detection in well 6507/11-8. Brine and gas-saturated sands are well separated (blue and green) when velocities are low (soft rocks) and poorly separated (red zone) when velocities are high. The fluid saturation trend is perpendicular to that of porosity, clay and pore pressure.

The cross-plot points in the Figure 5.3 are color-coded using gas saturation log; the P-and S-wave impedance logs (in the curve display) are color-coded based on the three populations defined in the cross-plot domain. The three zones can easily be identified in the log cross-plot domain where the blue zone represents gas sand, the green zone represents brine sand and the red zone represents brine though it is poorly discriminated. P-wave velocity alone is not a good enough indicator of lithology and fluid because of the overlap in velocity for various types of rocks (Rojas et al., 2005). Also P-wave impedance alone is highly affected by fluid effects and there is ambiguity in lithology separation. However, if combined with S-wave velocity the ambiguity is reduced. Therefore P-and S-wave impedances have been used to separate and detect pore fluids and lithology.

5.2.3 Using Vp/Vs and P- wave impedance (AI) cross-plot

Figure 5.4 has been used to identify the three (3) main zones (A, B and C) on the Vp/Vs versus AI cross-plot. Gas and brine sands have been identified and mapped on their corresponding reservoir positions as shown below. Thin Carbonate cemented sands are also visible at the base of Ile Fm and on the cross-plot domain.

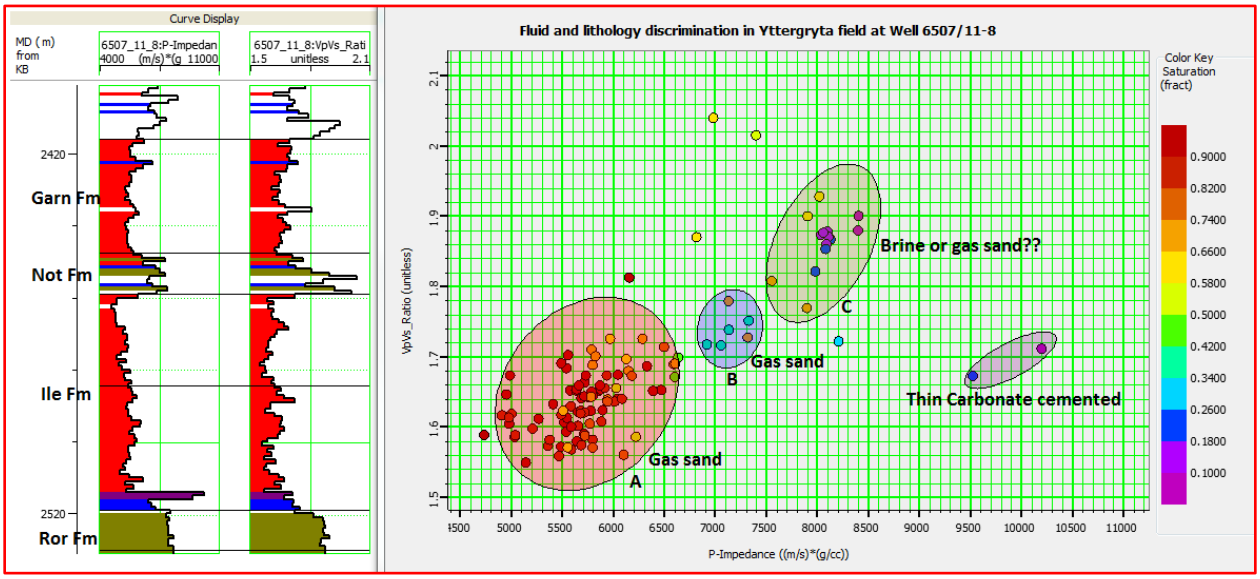

Figure 5.4: Shows a Vp/Vs versus AI cross-plot on which three (3) zones (A, B and C) have been interpreted and attributed to different types of lithology and fluids in Garn, Not, Ile and Ror formations. The data points have been color coded using gas saturation log. The Vp/Vs and AI logs in the curve Display have been color coded based on the three zones on the cross-plot. Clearly gas and brine sands can be seen in their respective reservoir intervals.

5.3 Reservoir property predictions from well-log data using RPTs

Both static and dynamic rock physics template (RPT) analysis was performed on data from the Norwegian Sea, gas sands were encountered in this well. The zone considered in this project is between 2400-2530 m (measured depth, MD from Kelly bushing, KB). The depth zone of interest considered in this research lies within the Fangst group which comprises of three main formations (Garn, Not and Ile) and some few meters in the Båt group (Ror Fm) as already discussed and as shown in Figure 5.4.

The zones (A, B and C) as identified in Figure 5.4 have been used consistently in all the RPT cross-plots and they will have the same meaning and data points. Cross-plots color coded using

gas saturation, porosity and shale content (volume of clay) logs have been presented. These three logs were logged from different depth (see Figure 3.6), so zone B has many points in all plots color coded with shale content log because it covers a larger depth than gas saturation and porosity logs.

The reservoir sandstone is unconsolidated with some cementation. For this reason, both friable sand and constant-cement models were applied on the dataset. In addition, a patchy cemented sandstone model was applied on the same dataset. The following parameters were used in the modeling of RPTs for the Yttergryta field in the Norwegian Sea.

Summary of the properties used in the modeling of RPT	
Effective pressure = 25.1 MPa	Brie constant = 1 (Big patches-Voigt)
Temperature = 91˚C	Critical porosity = 0.40
Brine salinity = 0.06 Mppm	Shear friction factor = 0.30
Gas gravity = 0.776 API	Coordination number = 8.64
P_c = 50 MPa, P_P = 10-45 MPa, intervals of 5 MPa. S_g=0-1.0 in intervals of 0.25	CCT cementation range, Porosity from (0.398-0.40)

Table 5.1: Acoustic properties for brine and hydrocarbons, and rock physics model inputs.

5.3.1 Static and dynamic RPT analysis of real data using constant-cement model

The constant-cement model was superimposed on Vp/Vs versus AI cross-plot domain containing data plotted for the 130 meter interval from Yttergryta field. Cross-plots from static RPTs color coded based on gas saturation (Figure 5.5), porosity (Figure 5.6) and shale content (Figure 5.7) logs are presented.

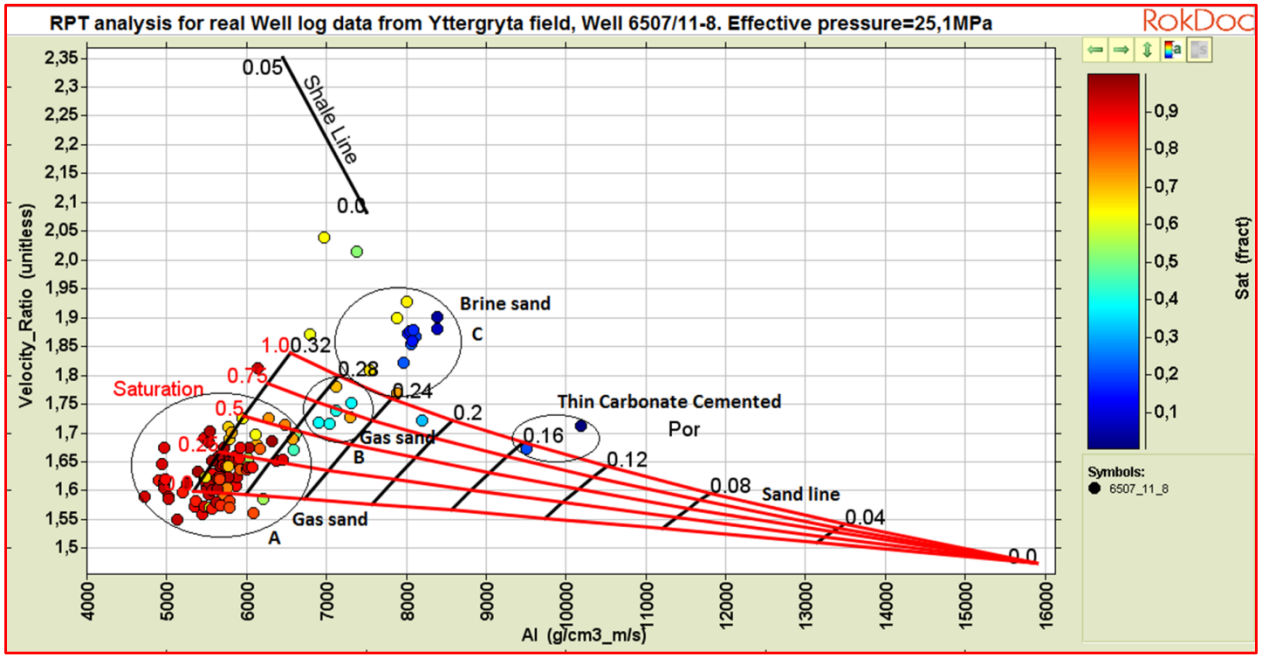

Figure 5.5: A constant-cement model superimposed on Vp/Vs versus P-wave acoustic impedance cross-plot domain. Data points are color coded based on gas saturation log. Zone A is a fully gas-saturated sand zone (50-100% gas), Zone B is a low gas sand zone (0-50% gas) and Zone C is a brine saturated sand zone (0% gas) based on RPT prediction. Thin carbonate cemented sands don't contain any gas.

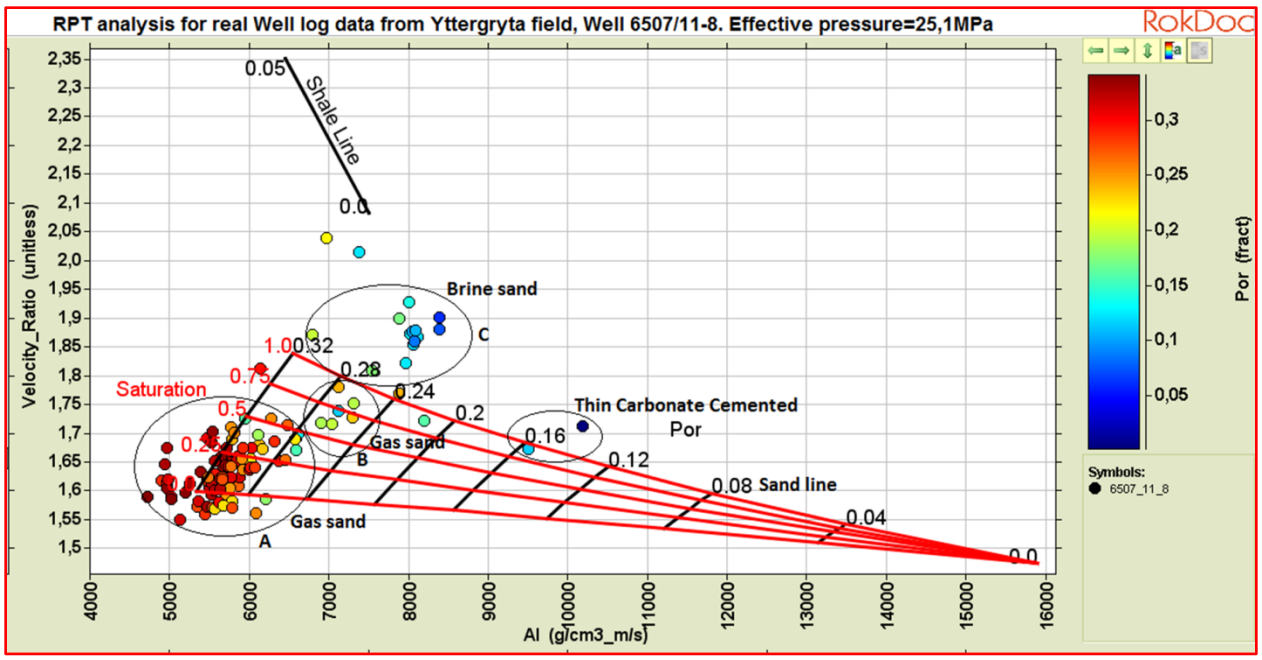

Figure 5.6: A constant-cement model superimposed on Vp/Vs versus P-wave acoustic impedance cross-plot domain. Data points are color coded based on porosity log. Based on the RPT interpretation, Zone A is a high porosity gas-sand zone (0.26-0.36), with porosities higher than those for Zones B (0.24-0.28) and C (0.24-0.32). Thin carbonate cemented sands have the lowest porosity (0.14-0.16).

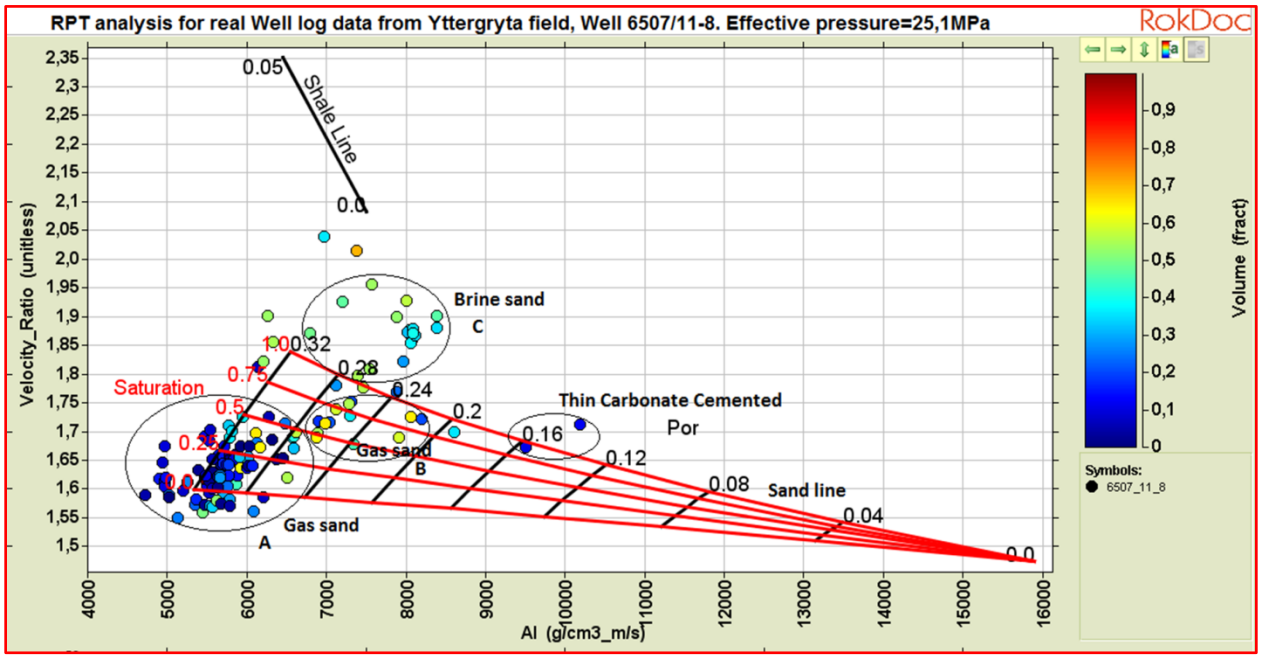

Figure 5.7: A constant-cement model superimposed on Vp/Vs versus P-wave acoustic impedance cross-plot domain. Data points are color coded based on shale content log. Zone A has very low shale content (clean sands) compared to Zones B and C. The trend for data points in Zone C is towards the shale line, an indicator of increasing shale content for points in zone B and C. Thin carbonate cemented sands contain almost no shale content.

Observations from the static RPTs based on the constant-cement model:

Zone A has an average gas saturation of above 80% according to the RPT prediction which matches well with the well-log measurement (around 80-100%) though some few points have close to 60% gas (yellow). The zone has an average porosity of about 0.32 from the RPT which matches with the observed porosity from well-log measurement of around 0.25-0.35. Some few data points in this zone have porosity close to 0.22 (yellow, based on well-log measurements), thus their porosity is overpredicted. The data points have low clay content with an average of about 0.1, so it can be regarded as a clean sand zone, however there some few data points with slightly higher clay content than the average.

Zone B has an average gas saturation of about 25% as predicted by the RPT which is lower than 40% gas as interpreted from well-log measurement. However the zone contains some few points with close to 70% gas (from well-log data interpretation) but plotting on and below the RPT's 25% gas saturation line, (underpredicted saturation). This is not a good match. The zone has an average porosity of about 0.26 and dominated by data points with porosity 0.18. This porosity is slightly in agreement with the measured porosities (0.14, 0.18 and 0.22). With respect to clay content, the zone has an average of about 0.5. Most of the data points in this region have 0.5 and some with 0.6 of clay content as interpreted from the color scale so it is not clean; however it is below the sand line.

Zone C is predicted by RPT to be fully brine saturated dominated by blue (0% gas) data points. But it contains some yellow data points (65% gas based on well-log data) but plotted above the brine sand line, (underpredicts saturation). The two interpretations are contradicting. The zone has porosities from 0.24-0.32 as predicted by the RPT which is higher than what the well-log data indicates (0-0.22). The zone has clay content from 0.4-0.6 which is an indicator that the sands are not clean. Also the trend of the points is towards the shale line.

Thin carbonate cemented regions have also been realized. They do not contain any gas, have the lowest porosity (0.14-0.16 from the RPT) and the highest acoustic impedance around 9.5-10.2 g/cc*km/s. The corresponding clay content is about 0.0 according to the well-log measurement. These carbonate cemented sands are well indicated from the logs at base Ile formation (see Figures 3.6, 5.4).

Since most of the data points plotted on average around porosity of 0.25 and 0.32, 4D RPTs for the data around these regions have been modeled for further study of saturation and pressure properties. The 4D RPTs have been constrained at a constant confining pressure of 50MPa (assumed), and pore pressure has been changed from 10-45 MPa in intervals of 5 MPa. Therefore effective pressure increases from 5-40 MPa in the same intervals of pressure. Gas saturation changes between 0-100% in intervals of 25%. Other parameters remained the same as for the static RPTs.

The 4D RPT in Figure 5.8 was modeled based on constant-cement static RPT (Figures 5.5, 5.6 and 5.7) and has been constrained at a constant porosity of 0.25. The focus is at data points in gas zone B and some in zone C. These points have gas saturation in the range 0-50% with porosity of about 0.25. Zone C plotted off the template and can be regarded as brine saturated sands, which are not clean. Pressure interpretation of the different data points was challenging since the model is insensitive to pressure changes and very stiff.

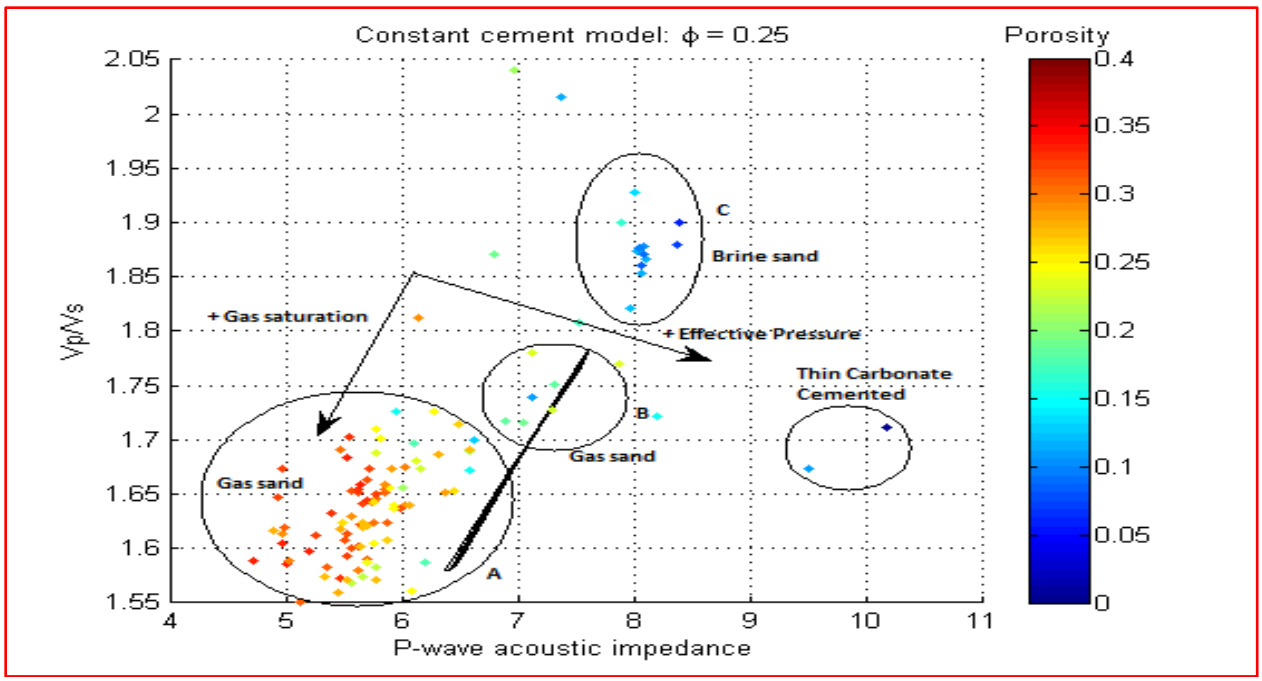

Figure 5.8: A 4D RPT modeled based on a constant-cement static RPT. Data points are color coded based on porosity log. From well-log measured porosity, data points in zone B have variable porosities ranging between 0.1-0.25 and those in zone C have relatively the same porosity ranging between 0.1-0.15, (lower than in zone B). Zone C points could be buried at a greater depth than zone B points, hence a difference in porosity.

The 4D RPT in Figure 5.9 was modeled based on the same model as in Figure 5.8 but constrained at a different constant porosity of 0.32. Other parameters remained the same as for the constant cement static RPTs already discussed.

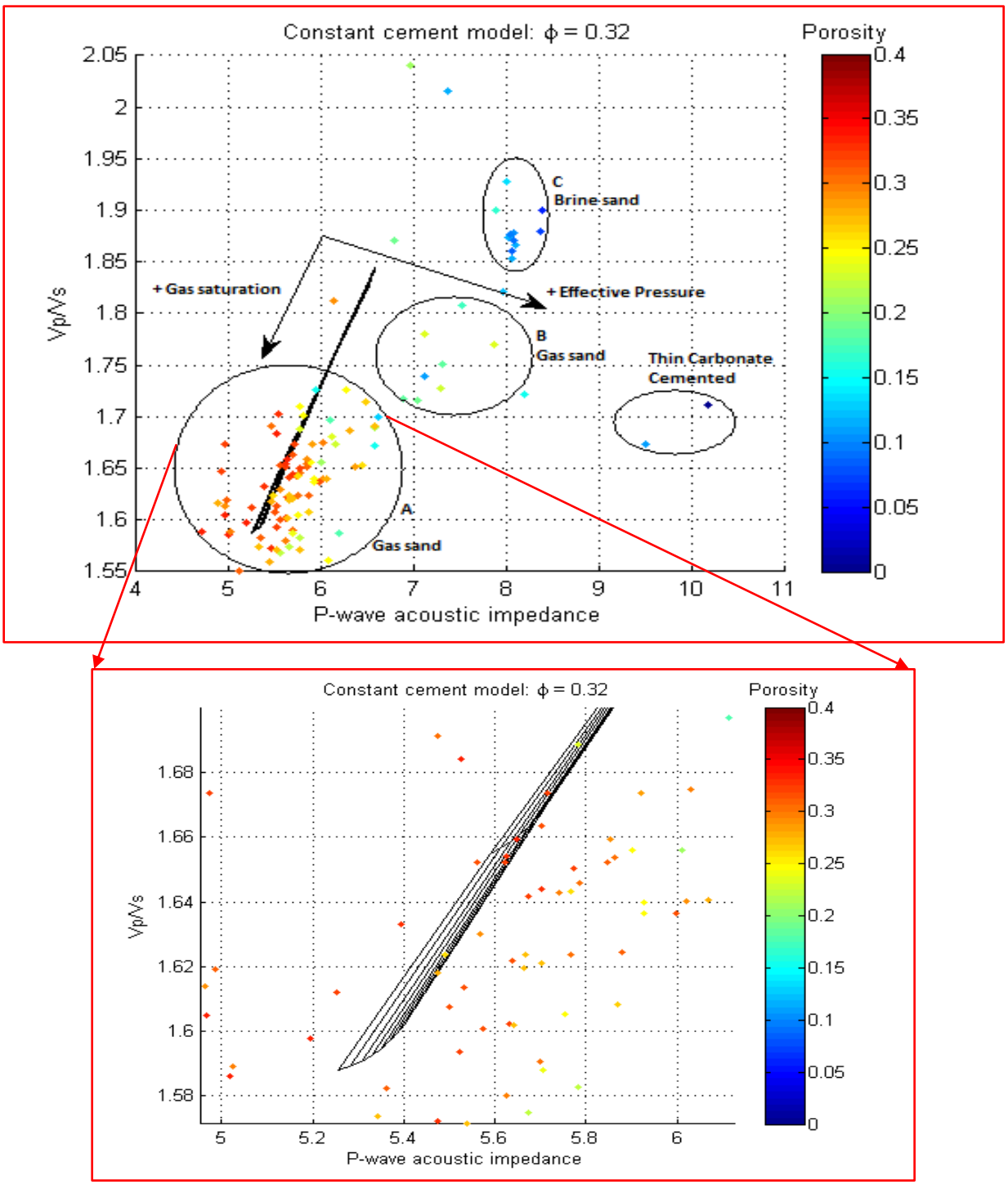

Figure 5.9: 4D RPT analysis for real well-log data using constant-cement model superimposed on a Vp/Vs versus AI cross-plot domain containing data plotted for the 130 meter interval from Yttergryta field (top) and zoomed (down). Data points are color coded based on porosity log. The zoomed zone is part of a gas saturated sand zone A. It has high porosity between 0.20-0.35.

5.3.2 Static and dynamic RPT analysis of real data using friable sand model

The friable sand model was superimposed on Vp/Vs versus AI cross-plot domain containing data plotted for the 130 meter interval from Yttergryta field. Cross-plots from static RPTs color coded

based on gas saturation (Figure 5.10), porosity (Figure 5.11) and shale content (Figure 5.12) logs are presented.

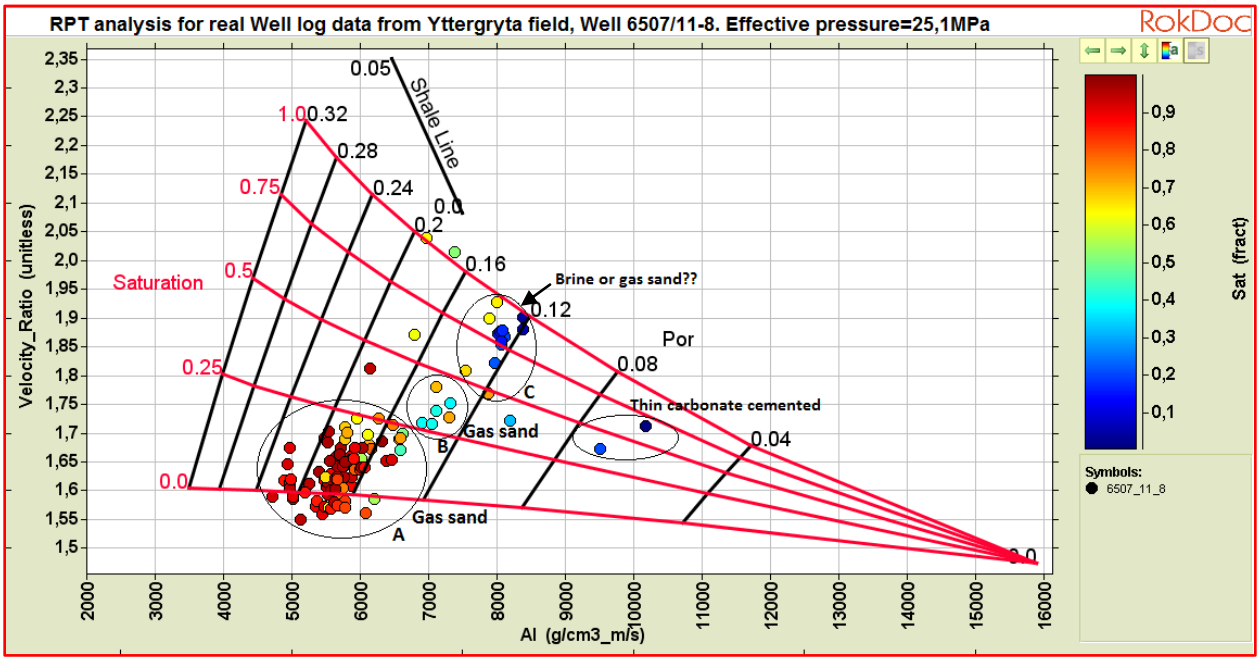

Figure 5.10: A friable sand model superimposed on Vp/Vs versus P-wave acoustic impedance cross-plot domain. Data points are color coded based on gas saturation log. Zone A is a fully gas-saturated sand zone (75-100% gas), zone B is a gas sand zone (50-75% gas) and Zone C is a low gas sand zone (0-50% gas). Thin carbonate cemented sands show some gas saturation (25% and 60%). All interpretations based on RPT. No brine sands predicted above the brine sand line in this case.

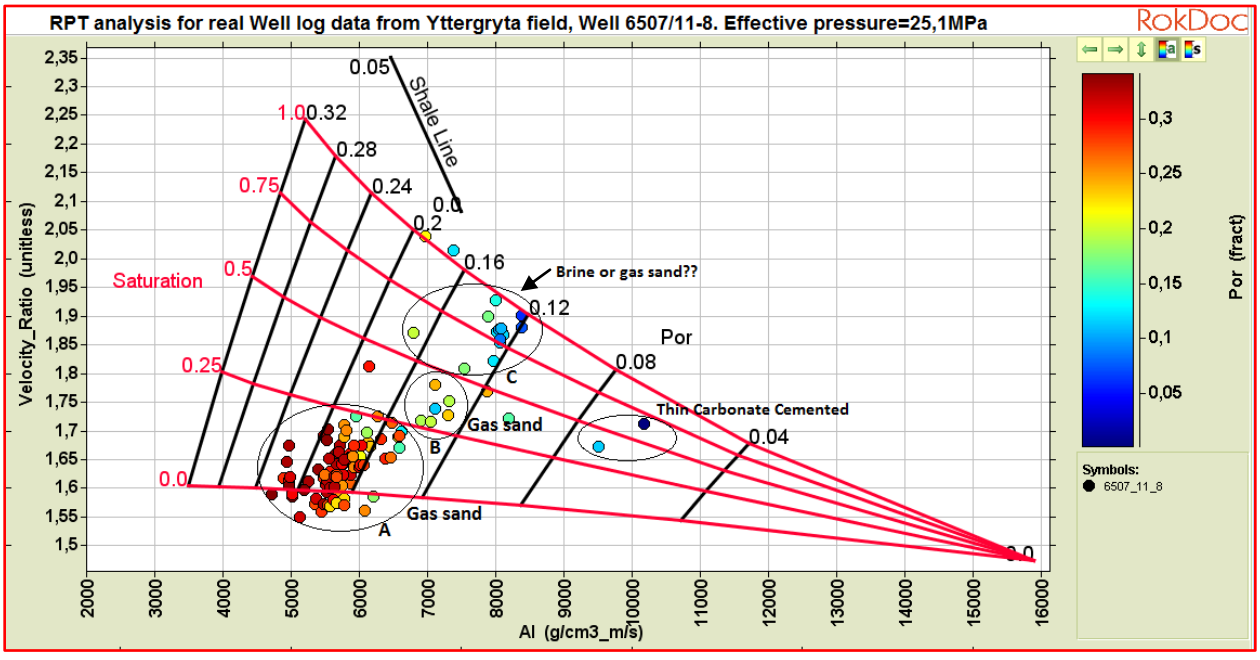

Figure 5.11: A friable sand model superimposed on Vp/Vs versus P-wave acoustic impedance cross-plot domain. Data points are color coded based on porosity log. Zone A is a high porosity (0.14-0.22) sand zone, zone B is a low variable porosity (0.12-0.14) sand zone. Zone C has almost the same porosity as zone B. Thin carbonate cemented rocks have the lowest porosity about 0.07.

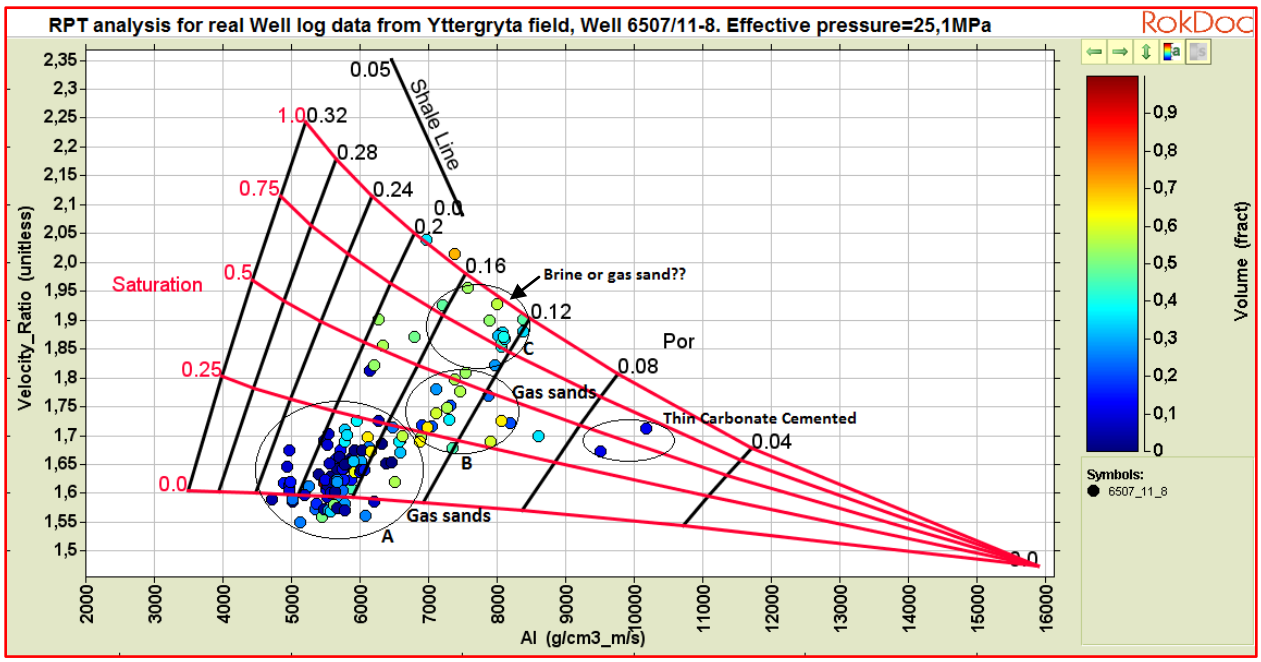

Figure 5.12: A friable sand model superimposed on Vp/Vs versus P-wave acoustic impedance cross-plot domain. Data points are color coded based on shale content log. Zone A has a very low shale content therefore can be regarded as clean sands to zones B and C.

Observations from the static RPTs based on the friable sand model:

Zone A has an average saturation of about 90% based on RPT interpretation which matches well with the well-log data measurements (80-100% gas); though there are some few points with close to 65% gas (yellow). There is no good match between the porosity predicted by the RPT (0.14-0.22) and the well-log measurements (0.25-0.35). The model underpredicts porosity. The zone also contains some few points with porosity close to 0.22 (yellow) but plotting around 0.18 on an RPT. Zone A has clay content of about 0-0.2 with an average of 0.1. The zone can be regarded as clean sand zone.

Zone B has an average saturation of 60% from the RPT which is higher than the well-log measured saturation of 40% though there are some data points with about 65% gas. The zone has an average porosity of 0.14 (from RPT) and 0.18 (green) from well-log measurements, the porosity is underpredicted. The zone also contains some data points with porosity <0.05 (blue) which is far smaller than what is predicted by the RPT (0.12-0.13). It has clay content of about 0-0.6 with an average of 0.5.

Zone C has an average gas saturation of 25% from the RPT which is slightly in agreement with the well-log measurements; however the zone contains more data points (yellow) with saturation close to 65% plotting around 50% and 10% saturation lines on the RPT. The zone has an average porosity of 0.13 from the RPT which is slightly higher than the measured porosities. The zone contains other points which match the well-log measured porosities. The zone has shale content between 0.4-0.6, so the sands are not clean.

Most of the data points plotted on average around porosity of 0.12 and 0.18, so 4D RPTs for those data zones were modeled to study saturation and pressure properties. These 4D RPTs were constrained at a constant porosity of 0.12 and 0.18, (Figures 5.13 and 5.14 respectively) and other parameters remained the same as for the static RPTs.

In Figure 5.13, most of the data points from zone A was not captured by the template and has very low Vp/Vs. It is classified as a gas sand zone with very high gas saturation. Zone B is also a gas sand zone with effective pressure between 10-25 MPa, gas saturation between 50-75% and slightly higher Vp/Vs compared to zone A. Zone C has the same effective pressure range with the lowest gas saturation between 0-35% and very high Vp/Vs. This is an indicator that the zone C is brine dominated.

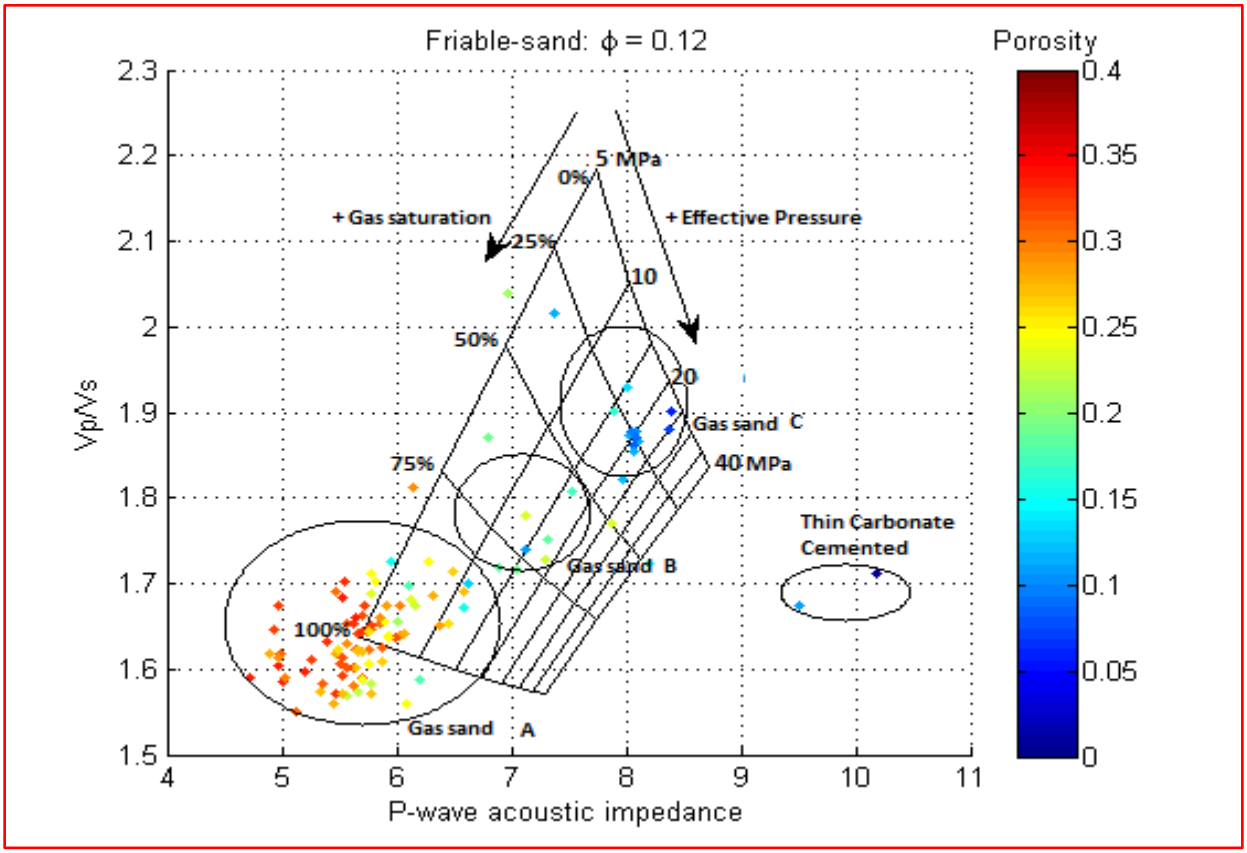

Figure 5.13: 4D RPT modeled based on the friable sand static RPT constrained at porosity of 0.12. Data points are color coded based on porosity log. It can be observed that data points in zone C have porosities between 0.1-0.15 with an effective pressure between 15-25 MPa with very low gas saturation. Gas sand zone B has relatively high porosities with slightly lower effective pressure and high gas saturation. Most of zone A data points plotted off the template because they have high porosities (between 0.15-0.35) than what the RPT was constrained at.

From Figure 5.14, zone A has most of its data points falling between 10-40 MPa of effective pressure and have gas saturation between 75-100% with a very low Vp/Vs. According to the color scale, these points have a porosity range of 24-32%. Zone B and C data points plotted off the template and have porosity of about 0.12.

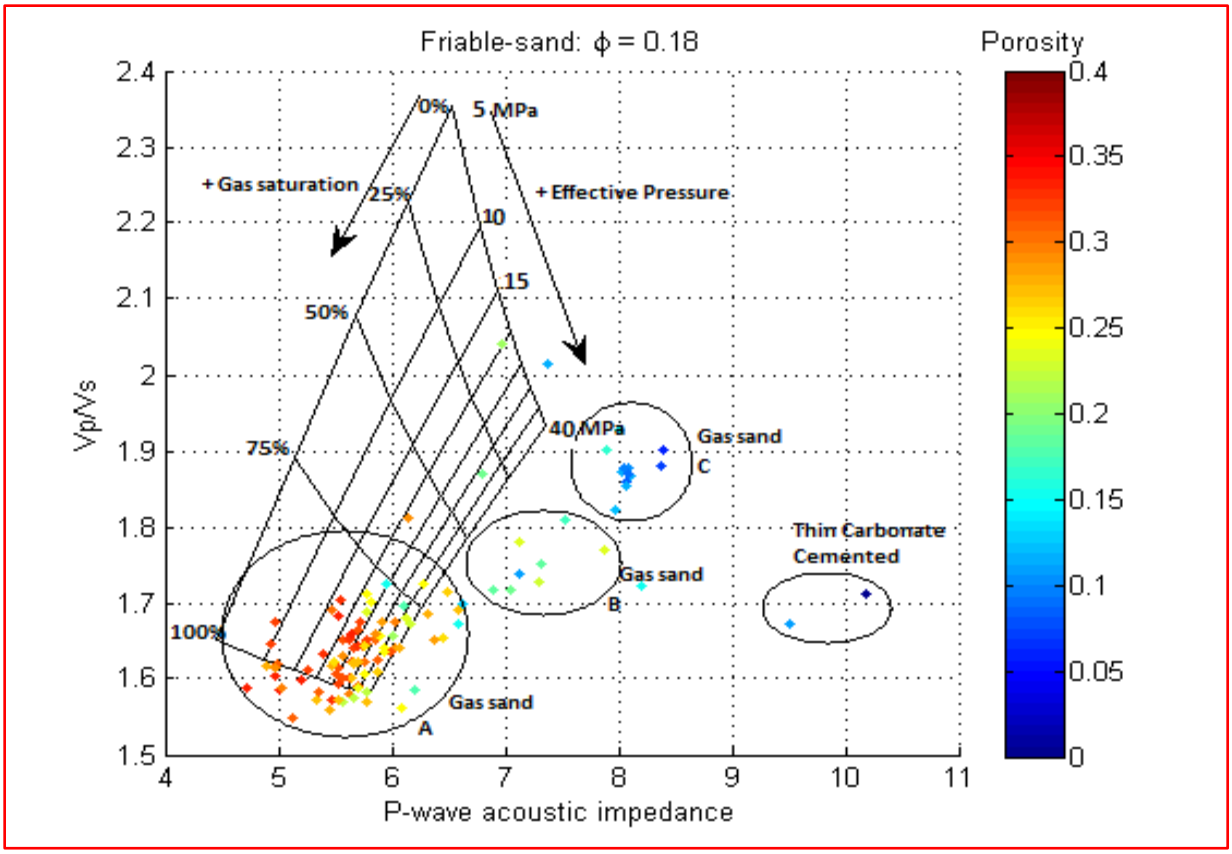

Figure 5.14: 4D RPT modeled based on the friable sand static RPT constrained at porosity of 0.18. Data points are color coded based on porosity log. Zone A is a high porosity gas saturated zone with relatively high effective pressure between 10-40 MPa. Zones B and C plotted off the template because they are of lower porosities than what the template was constrained at.

5.3.3 Static and dynamic RPT analysis of real data using patchy cemented sandstone model

A patchy cemented sandstone model was superimposed on Vp/Vs versus AI cross-plot domain containing data plotted for the 130 meter interval from Yttergryta field. Zones A, B and C are as interpreted in the previous cases were tested and predicted using a patchy cemented sandstone model.

Plots with different color coding using gas saturation (Figure 5.15), porosity (Figure 5.16) and shale content (Figure 5.17) logs have been used in the discussion. Gas saturation changes from 0-100% in intervals of 25% and porosity from 0-32% in intervals of 4%.

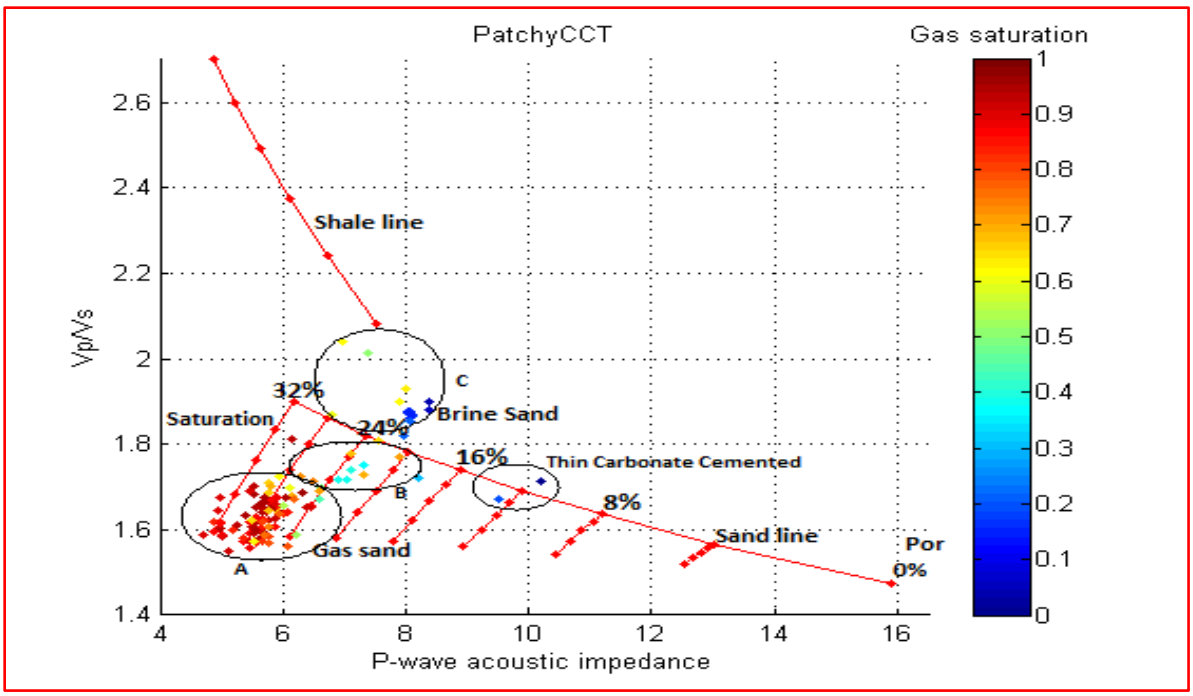

Figure 5.15: A patchy cemented sandstone model superimposed on Vp/Vp versus P-wave acoustic impedance cross-plot domain. Data points are color coded based on gas saturation log. Zone A is a fully gas saturated sand zone (50-100% gas), zone B is a slightly low gas sand zone (0-50%) and zone C is above the brine sand line so it can be interpreted as brine sand zone, all interpretations based on RPT predictions.

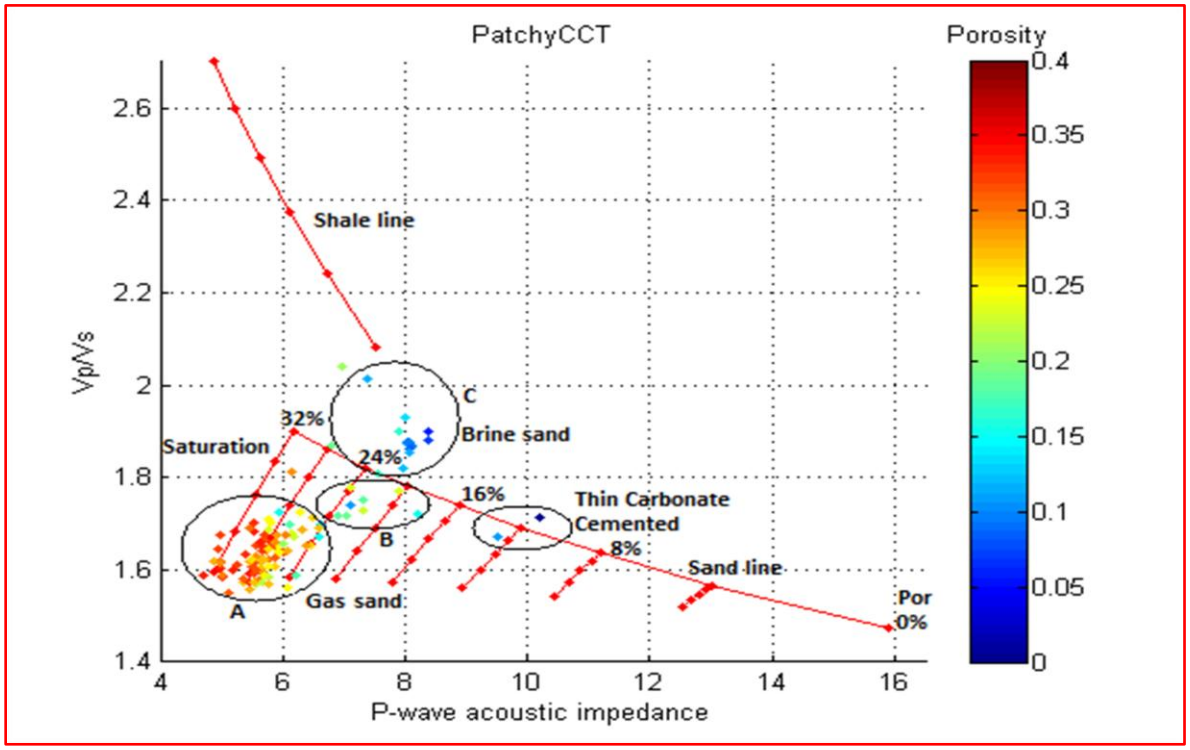

Figure 5.16: A patchy cemented sandstone model superimposed on Vp/Vp versus P-wave acoustic impedance cross-plot domain. Data points are color coded based on porosity log. Zone A is a high porosity sand zone (24-34%) compared to other zones B (18-24%) and C (20-32%). Thin carbonate cemented sands have the lowest porosity of about 12% as predicted by the RPT.

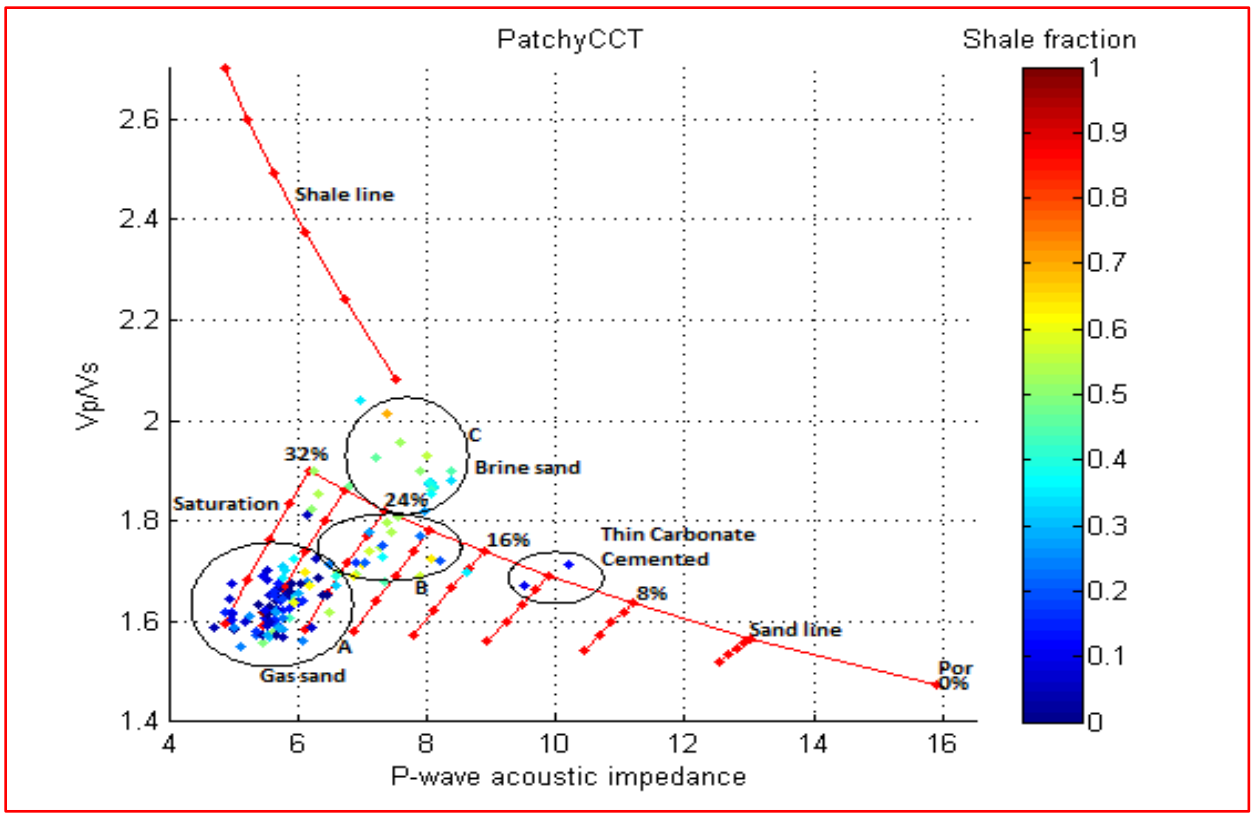

Figure 5.17: A patchy cemented sandstone model superimposed on Vp/Vp versus P-wave acoustic impedance cross-plot domain. Data points are color coded based on shale content log. Zone A has the lowest shale content compared to zones B and C based on RPT interpretation. Zone C data points have a tendency of moving towards the shale line, which could be another indicator that it's not clean brine sand. Thin carbonate cemented sands also have very low shale content as predicted from the RPT.

Observations from the static RPTs based on the patchy cemented sandstone model:

Zone A data based on the RPT prediction, has an average gas saturation of about 96% which matches with the measured well-log saturation. The zone has an average porosity of 28% from the RPT which matches the well-log measured porosity. This zone has very low shale content (0.0-0.2) however it contains some few yellow points whose shale content is around 0.5-0.6. But on average the zone can be regarded as clean sands.

Zone B data points have an average gas saturation of 40% (same as well-log reading). It has porosity range of 18-24% as estimated from the RPT which agrees with the color scale for most of the data points. However it contains some blue points which when interpreted by the color scale would be having 0% porosity which contradicts with 23% on the RPT. This zone has shale content is ranging from 0.0-0.5, which is an indicator that it is not clean. The zone is dominated by data points with shale content close to 0.2.

Zone C plots above the pure sand line and can be interpreted as pure brine sands (0% gas) on the RPT. It shows a mixture of blue data points (0% gas) and yellow data points (some traces of gas) based on well-log measurement. These yellow points move towards the shale line. The zone has porosity range of 20-28% from the RPT (with 0-20% porosity and many data points around 5%

as interpreted from color scale). This zone has shale content from 0.4-0.7 and can be taken as dirty sands with some shale. The trend of the data points in this zone is moving towards shale line.

Thin carbonate cemented sands have also been interpreted and do not contain any gas. This region has porosity of around 12% from RPT which contradicts with the well-log data prediction (0% porosity). This region has almost 0.0 shale content and have the highest acoustic impedance around 10 g/cc*km/s.

Further study of saturation and pressure was done by modeling 4D RPTs for most data around porosity of 0.23 and 0.28, Figures (5.18 and 5.19). Other parameters remained the same as for the static patchy cemented sandstone RPTs.

The 4D RPT in Figure 5.18 focuses on data points in gas zone B and some in zone C. These points have gas saturation in the range 0-50% with porosity of about 0.23. Zone C plotted off the template and can be regarded as brine saturated sands, which are not clean.

Figure 5.19 focuses on data points in zone A which have average porosity of 0.28. This zone is zoomed to further see the properties (saturation, pressure) of the points in details.

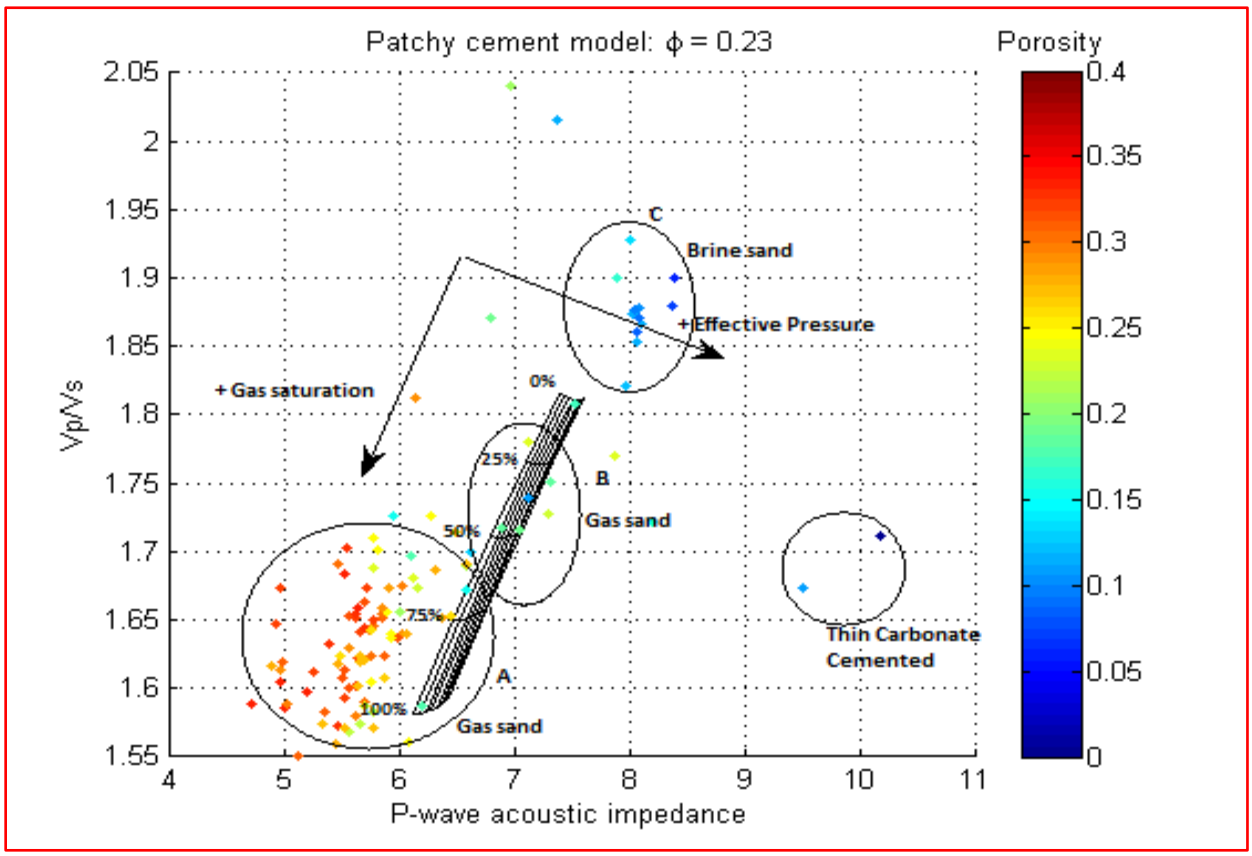

Figure 5.18: 4D RPT modeled based on patchy cemented static RPT constrained at porosity of 0.23. Data points are color coded based on porosity log. Zone A data points have high porosity than what the RPT is constrained at, so they plot off the template. Zone B and C have relatively the same porosity range and effective pressure but with different pore fluids and lithology as interpreted from the RPT and color scale.

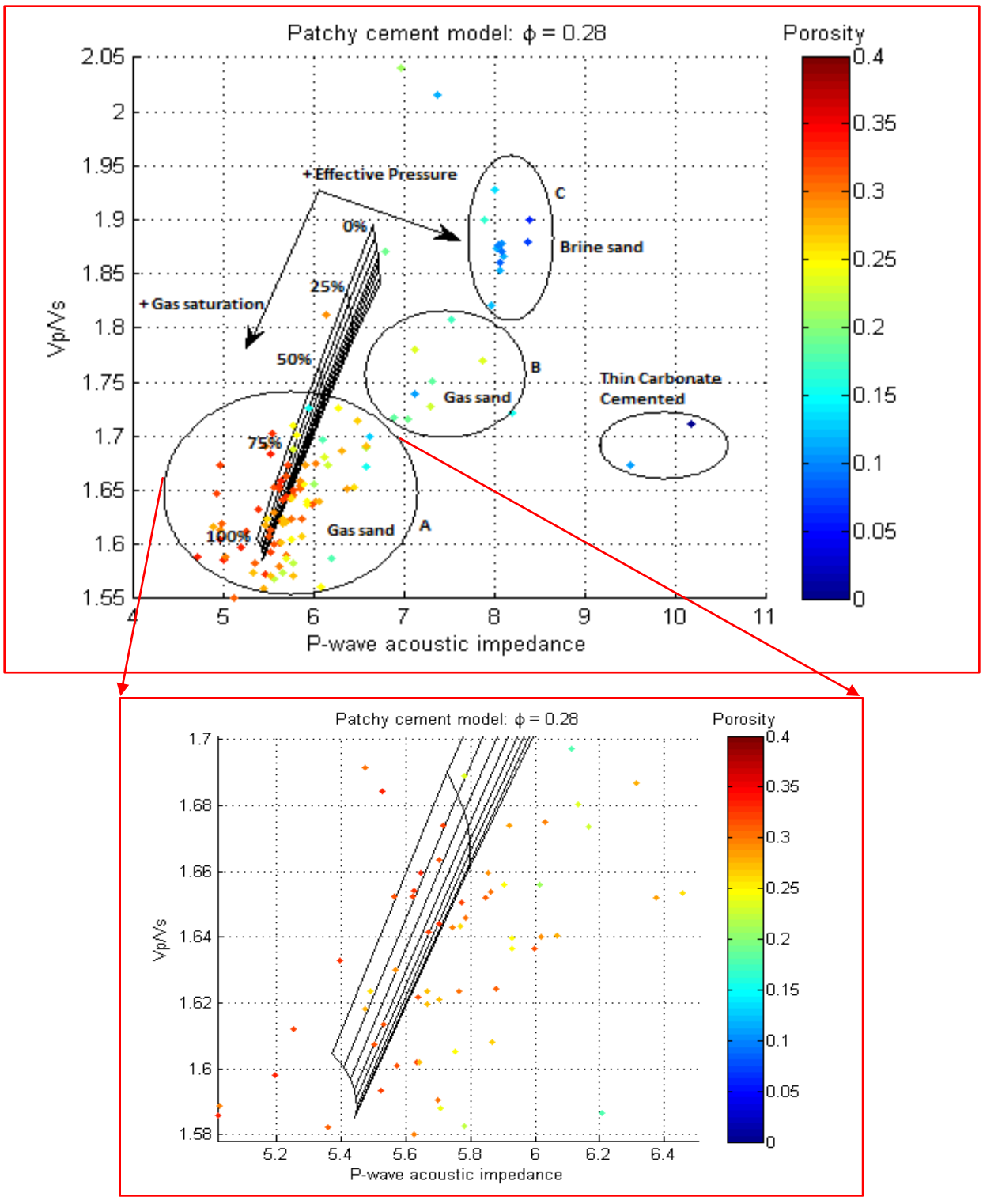

Figure 5.19: 4D RPT modeled based on patchy cemented static RPT constrained at porosity of 0.28, (top) and zoomed (bottom). Data points are color coded based on porosity log. This RPT was modeled to capture data points in zone A with high porosities between 0.2-0.35 with an average of 0.28. Zones B and C plot off template because they are of lower porosity than what the RPT was constrained at. The zoomed zone A data points have variable effective pressure distributed all over the template, very low P-wave acoustic impedance and Vp/Vs values.

5.4 Summary

This sub-study has demonstrated an integrated methodology of using rock physics templates to understand pressure, fluid and lithology effects in gas sandstones which are partly cemented in Yttergryta field in the Norwegian Sea. Different cross-plots of Vp/Vs versus AI with different models (contact theory, constant-cement and patchy cemented sandstone) have been discussed.

Combining P- and S-wave and density information can be very important in separation of fluid effects and lithology as it has been shown in this chapter. Low Vp/Vs values are directly related to sandstones with low clay content (like zone A).

Generally the sands in zone A can be regarded as tight sandstones with low Vp/Vs, (lower than 1.75). There is a small increase in Vp/Vs for sandstones with more clay (like zone B) and shales themselves have significantly higher Vp/Vs than sandstones (higher than 1.75 like in zone C). From this Chapter, both Vp/Vs and AI have been combined to show that there is a decrease and increase in both Vp/Vs and AI for gas and brine saturated sandstones respectively.

4D rock physics templates have been used in the characterization of this data. It has been noted that when saturation and pressure change, the data points will move accordingly. For example if pore pressure was increased this would mean a corresponding equal decrease in effective pressure. So the points will shift on the template in the direction of decreasing effective pressure. The same applies if there were changes in the fluid saturation, data points would move according to the directions indicated on the template whether increasing or decreasing gas saturation.

6.0 Applications of RPTs in 4D Seismic Reservoir Monitoring on data

6.1 Introduction

In this sub-study, we explore and demonstrate the power of RPTs in qualitative reservoir characterization and monitoring. 4D well-log effects have been modeled through fluid substitution by assuming different cases where one fluid is replaced by another. Fluid substitution modeling based on the Gassmann's theory was done by altering fluid contacts and saturations of the assumed output logs. This was followed by monitoring how this impacts the velocities, density and subsequent AVA synthetics. Different scenarios are presented and discussed in which pore fluids are substituted in some parts of the reservoir or in the whole reservoir. It is assumed that pores are filled with only two types of fluids; gas and brine, oil and brine or gas and oil. Figure 6.1 gives a brief overview of the most important steps in 4D seismic reservoir monitoring in this Chapter.

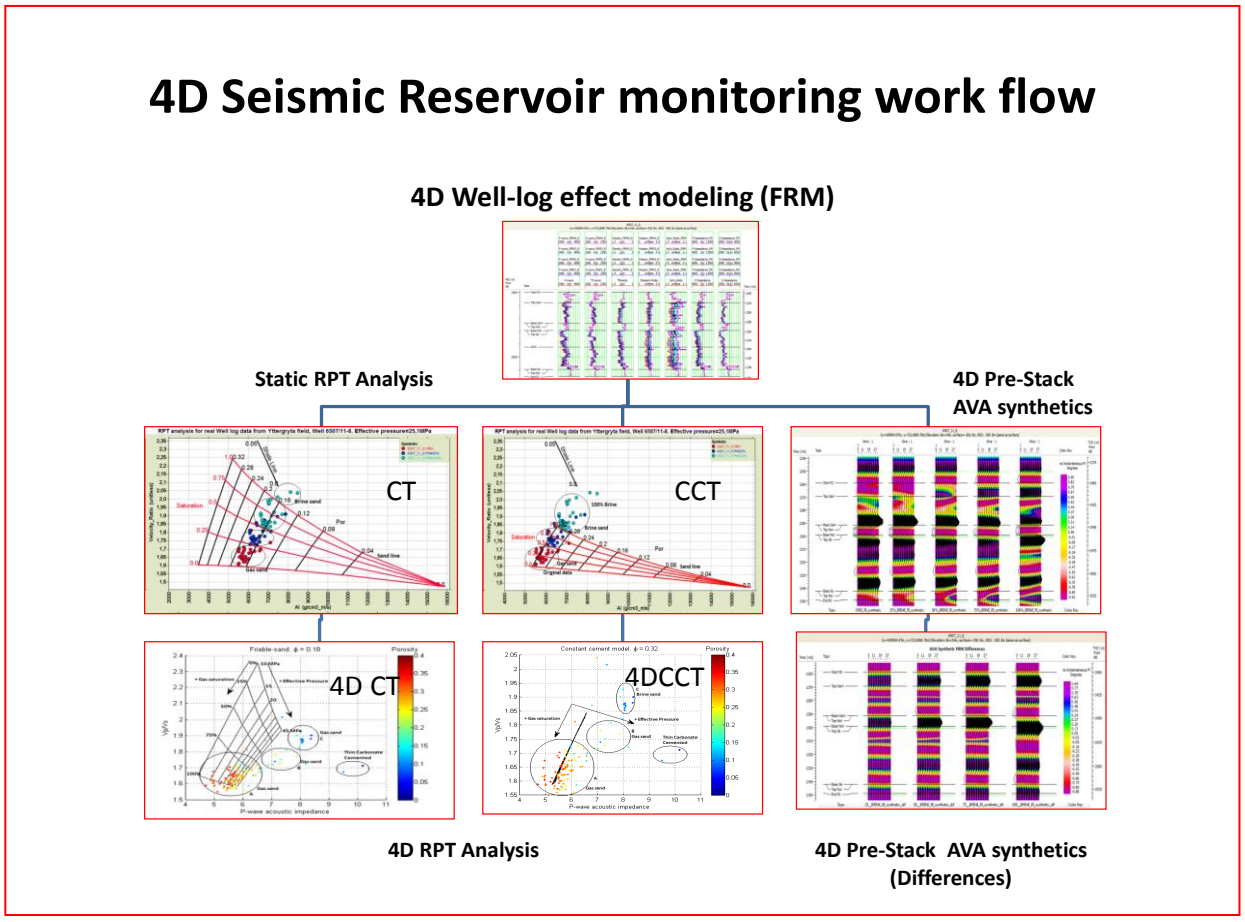

Figure 6.1: 4D well-log effects were modeled using Gassmann's model and corresponding AVA synthetics were computed based on Zoeppritz equations to see the effects of fluid substitution on seismic. The differences between the base and monitor were computed for the corresponding synthetics and later both static and dynamic rock physics templates were applied to monitor these fluid changes as realized on the synthetics.

Table 6.1 presents the reservoir constituent properties used in modeling of data from Yttergryta field in the Norwegian Sea.

Constituents	**Density [g/cm^3]**	**Bulk moduli [GPa]**	**Shear moduli [GPa]**
Quartz	2.65	36.8	44
Clay	2.6	15	5
Brine	1.02	2.77	0
Gas	0.21	0.06	0

Table 6.1: Reservoir constituent properties used in modeling of data from Yttergryta field in the Norwegian Sea

In the fluid substitution process, sandstone as a rock type and constant average gas saturation (approximately 96% gas, in-situ, based on saturation log) were considered in the whole reservoir zone.

6.2 Case 1: Gas-brine changes in Garn Fm

In this scenario, gas is being substituted with 25%, 50%, 75% and 100% brine in Garn formation from 2416-2447.50 m, MD from KB. The goal is to create new well-logs after brine substitution in Garn formation where gas sands have been replaced by brine sands and also to see the effect of fluid changes on seismic data through AVA synthetics.

In-situ fluids		Output fluids	
type	percentage	type	Percentage
Gas	96%	Gas	75, 50, 25, 0%
Water	4%	Water	25, 50, 75, 100%
Oil	0%	Oil	0%

Table 6.2: Case 1 FRM specifications

6.2.1 4D well-log effect modeling in Garn Fm

Figure 6.2 shows all well-logs: P-and S-wave velocities, density, Poisson ratio (PR), Vp/Vs, P- and S-wave impedances (AI and SI respectively) before and after fluid substitution at different brine saturations in their respective order. Gas in Garn formation was gradually substituted with brine. Results show an increase in P-wave velocity, density, PR, Vp/Vs, AI, SI and a slight decrease in S-wave velocity as brine replaces gas in this formation.

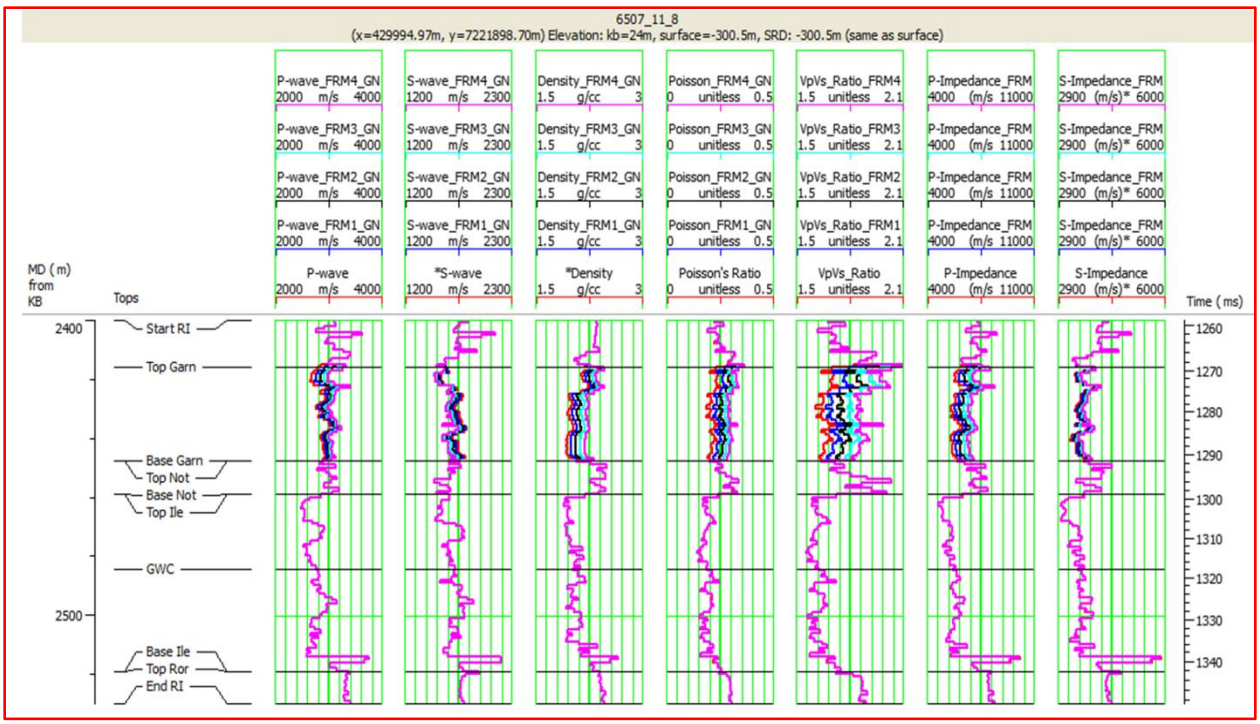

Figure 6.2: FRM results in Garn Fm (FRM1, 2, 3, and 4); represent 25%, 50%, 75% and 100% brine saturations and the original logs are in red. All logs increase with increasing brine except S-wave which acts in the opposite.

6.2.2 Brine substitution effects on seismic in Garn Fm

Using a zero phase and 25 Hz Ricker wavelet for angles from 5-30 degrees (near and far), AVA synthetics were computed using Zoeppritz equations for: original, 25%, 50%, 75% and 100% brine substituted well-logs (Figure 6.3). This was done to see how changes in fluid saturation in a reservoir can affect seismic data.

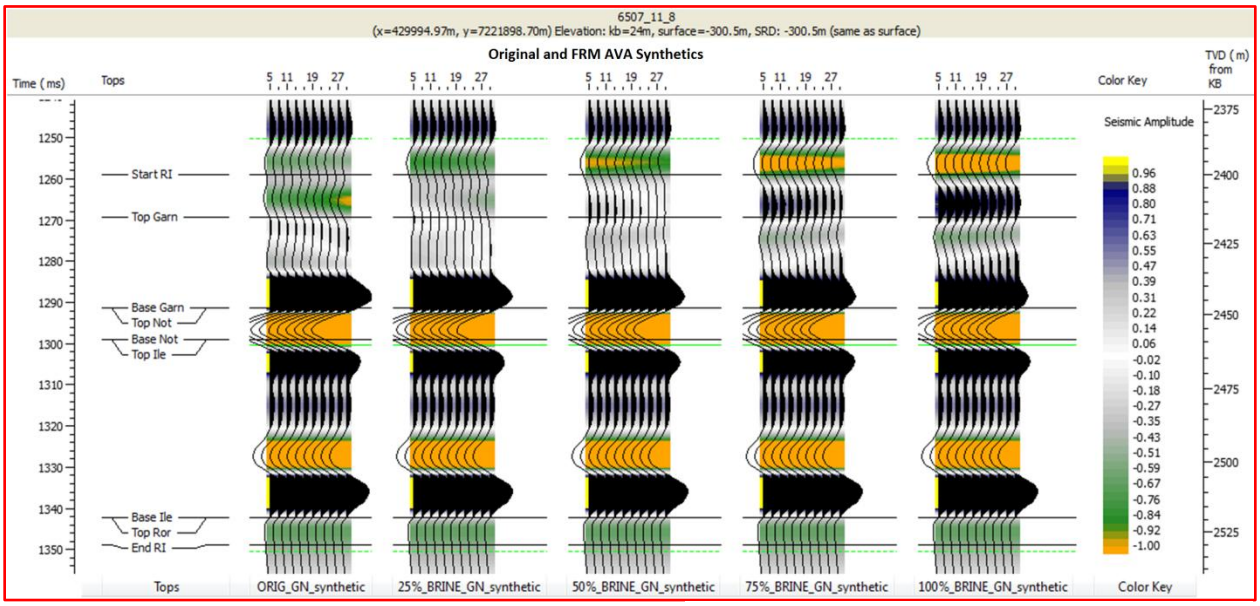

Figure 6.3: Effect of brine substitution in Garn Fm on seismic, AVA synthetics for: original, 25%, 50%, 75% and 100% brine saturated well-logs. There is an increase in amplitude (from negative to positive) as brine saturation increases. The amplitude almost reaches zero at 25% brine saturation and then starts to increase with further increase in brine substitution. At 100% brine saturation, there is a total phase reversal at the top of Garn formation since the whole formation is now brine saturated.

6.2.3 4D brine effects on seismic in Garn Fm

In order to further appreciate the effects of fluid substitution on seismic, the differences between the original AVA synthetics (base) and the brine substituted synthetics (monitors) were computed as shown in Figure 6.4.

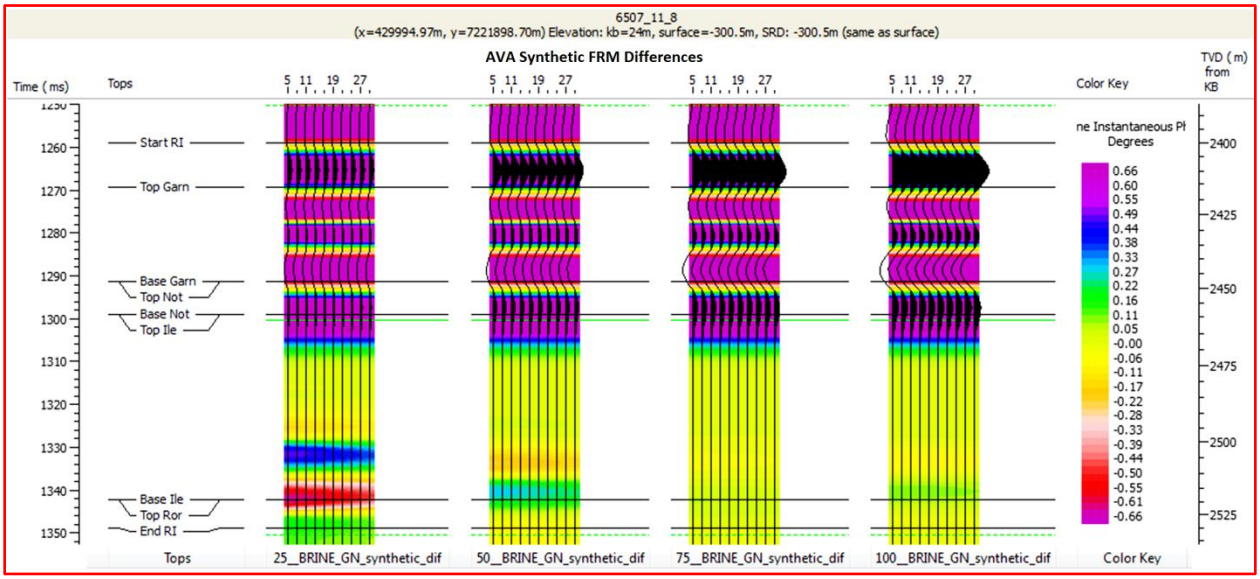

Figure 6.4: Computed 4D differences on seismic in Garn formation for 25%, 50%, 75% and 100% brine substitution; color scale is Cosine instantaneous phase. Positive seismic amplitude increases at the top of Garn FM and increasing negative seismic amplitude at its base as brine fills up the formation.

6.2.4 Stacking the observed 4D differences

The synthetic 4D differences were stacked to further analyze how seismic amplitudes change with increasing brine saturation in the Garn formation, Figure 6.5.

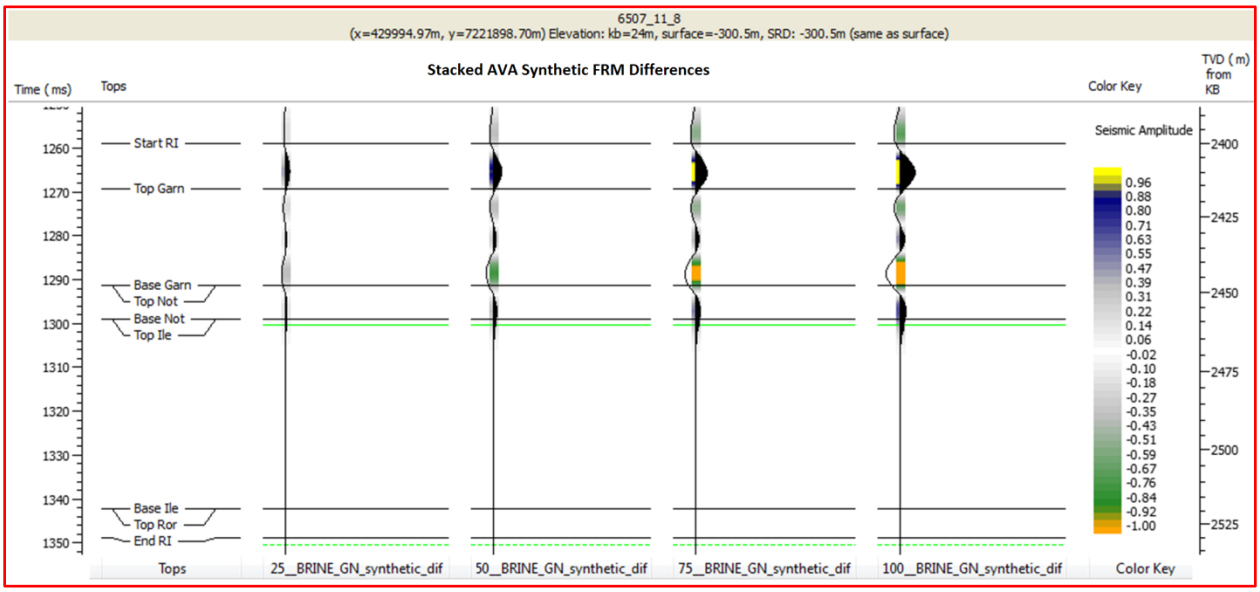

Figure 6.5: Stacked AVA synthetics differences in Garn FM for: 25%, 50%, 75% and 100% brine substitution. There is a good noticeable increasing positive seismic amplitude at the top of Garn FM and increasing negative seismic amplitude at its base as brine fills up the formation.

6.2.5 RPT analysis for fluid saturation changes in Garn Fm.

Fluid substituted well-log data from this formation was used to demonstrate the power of an RPT in reservoir monitoring. Two models have been applied in the demonstration of reservoir monitoring though they don't fit the data very well. The idea was to emphasize the relevance of selecting an appropriate model for a given data to avoid wrong predictions from the RPTs.

According to Figures 6.6 and 6.7, generally Vp/Vs and AI in gas sands are lower compared to those in brine saturated sands. When gas is replaced by brine, there is an increase in Vp/Vs and AI since the rock becomes stiffer and density also increases. This make the data points move along the saturation lines. Red, blue and green points show that they are of different saturations but with the same porosity (porosity is assumed to remain constant during fluid substitution), Figures 6.6 and 6.7.

Blue data points (50% brine) were expected to plot on average around 0.5 saturation line but rather plot on the RPT between: 0.5-1.0 (on CCT) and 0.25-0.5 (on CT) saturation lines in Figures 6.6 and 6.7. This means saturation is over- and underestimated according to FRM respectively. The green data points (100% brine) plotted above and below the brine sand line on the CCT (good match) and CT (wrong match) respectively. Such differences in the modeled saturations and the predicted saturations show that the models don't fit the data well.

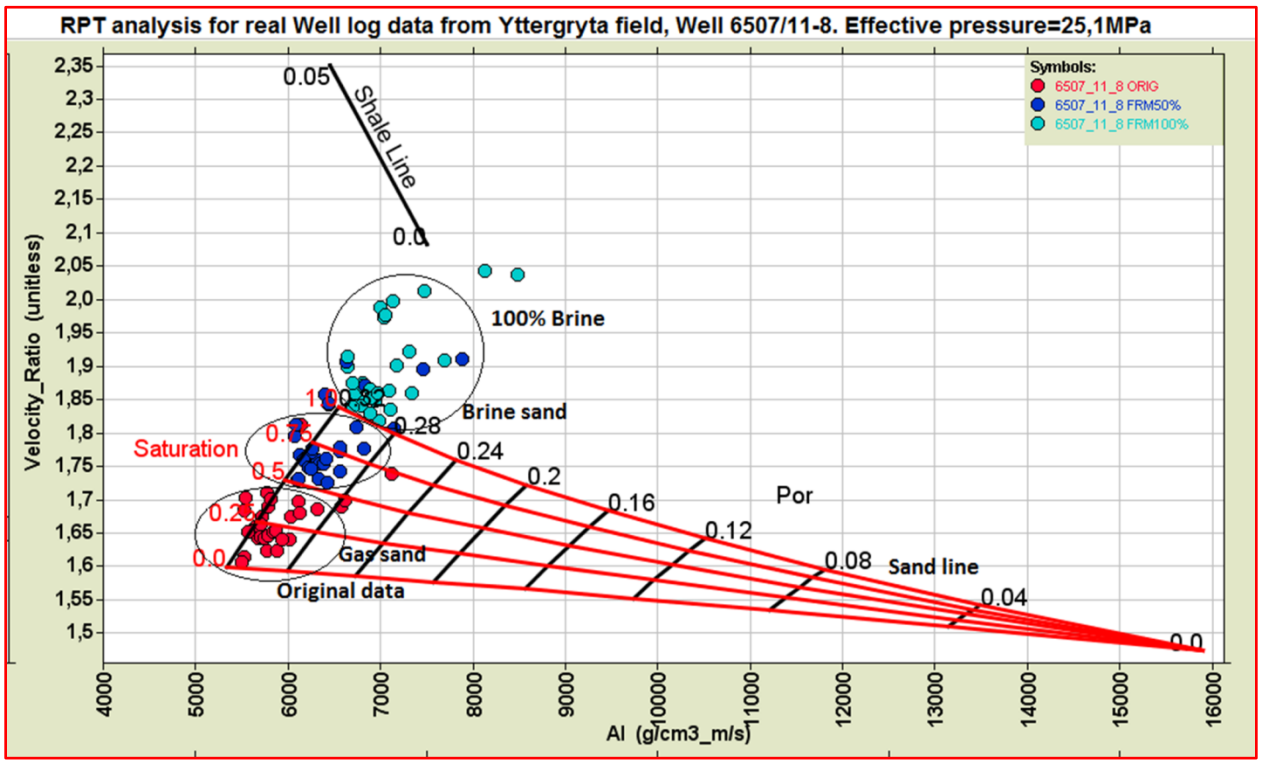

Figure 6.6: RPT analysis for: original data, 50% and 100% brine substituted data in Garn FM using a constant-cement model. Plotted well-log data is from Garn FM only and color code is according to brine percentages. Notice the increasing AI and Vp/Vs as brine saturation increases; this causes the data points to move along the saturation lines. When brine replaces gas, the rock becomes more stiffer than before and the rock bulk density increases hence an increase in AI and Vp/Vs.

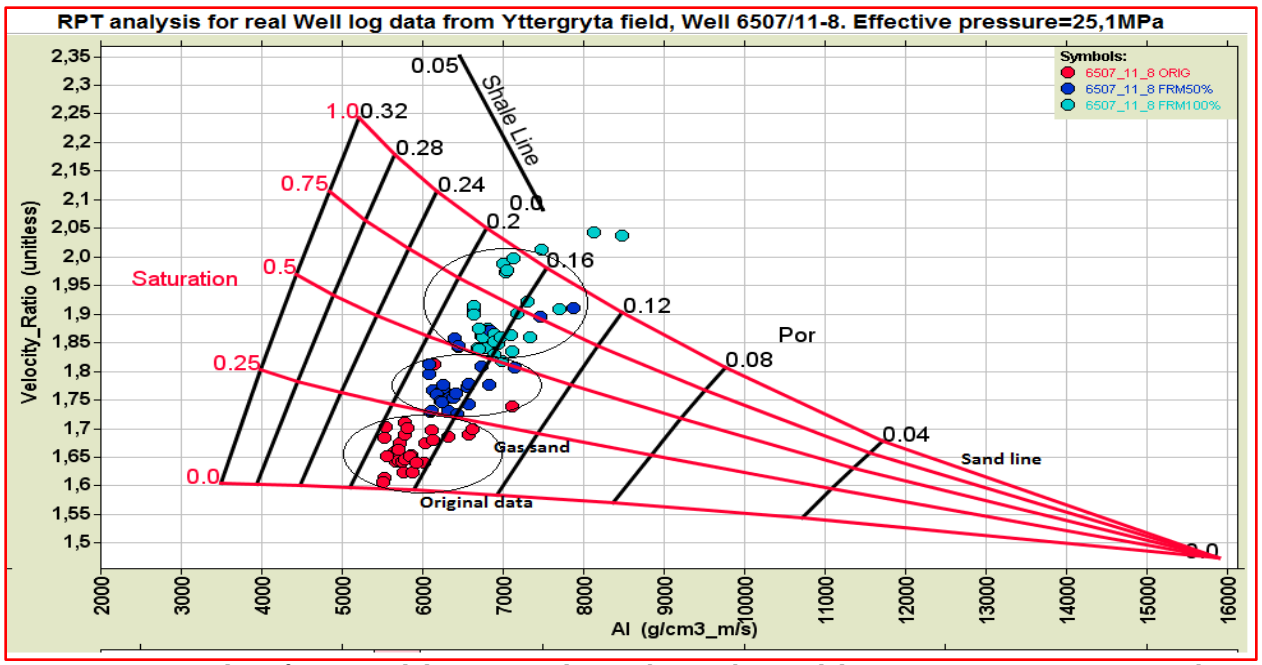

Figure 6.7: RPT analysis for: original data, 50% and 100% brine substituted data in Garn FM using a contact theory model. Well-log data plotted is from Garn FM only and color code is according to brine percentages. Data points move up along saturation lines as brine saturation increases. Green data points (100% brine saturation), this zone would have plotted above the pure sand line but it does not, (indicating that the model does not fit the data).

6.3 Case 2: Gas-water contact monitoring in Ile Fm

This case assumes shifting of the gas-water contact (GWC) from the initial position at base Ile to a new position marked 'GWC' in Figure 6.8 at a depth of 2160 m, MD from surface in the Ile Fm. New well-logs were generated and compared with the original logs. AVA synthetics before and after fluid substitution were computed using the same inputs as before and this was followed by computation of the difference between the two events to show the effect, Figure 6.8.

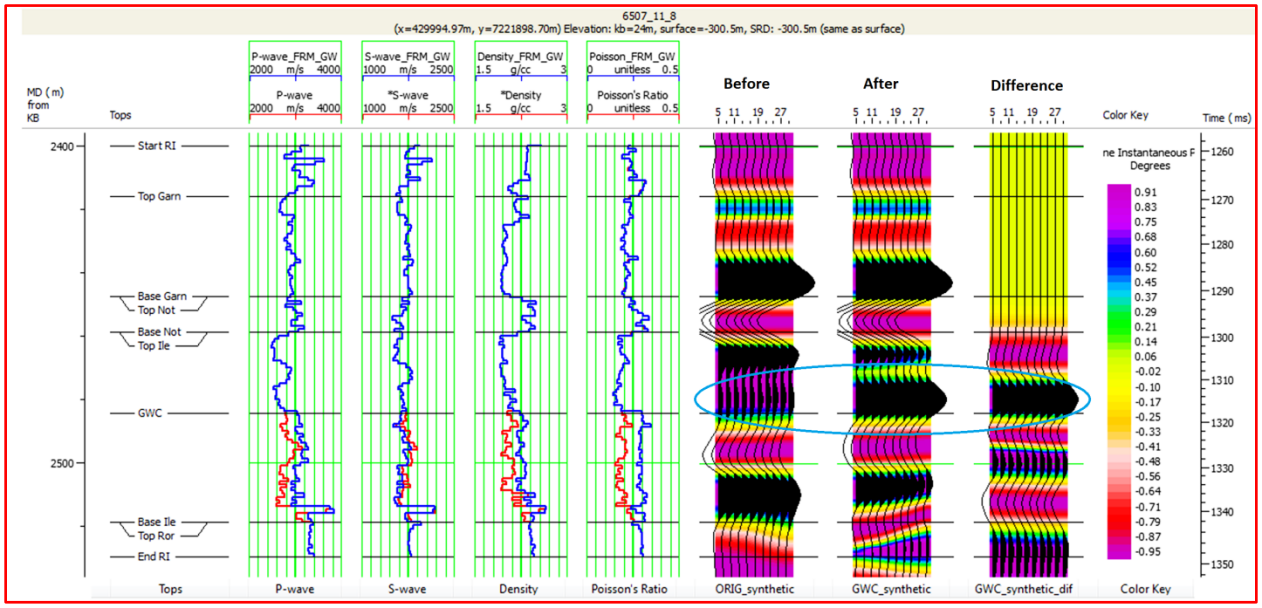

Figure 6.8: Effect of changes in gas-water contact from base Ile to a new position (GWC) on seismic. Original logs are in red and the FRM logs in blue. The blue marking on the synthetics shows a new strong reflector at GWC due to the increase in acoustic impedance as you move from the gas sands above to the underlying brine saturated sands.

6.3.1 RPT analysis for the gas-water contact in Ile Fm

RPT has been used here to demonstrate its ability in monitoring of fluid contacts. Data from FRM modeling (**Section 6.3)** has been used. The same models as before have been applied to evaluate this scenario as shown in Figures 6.9 and 6.10.

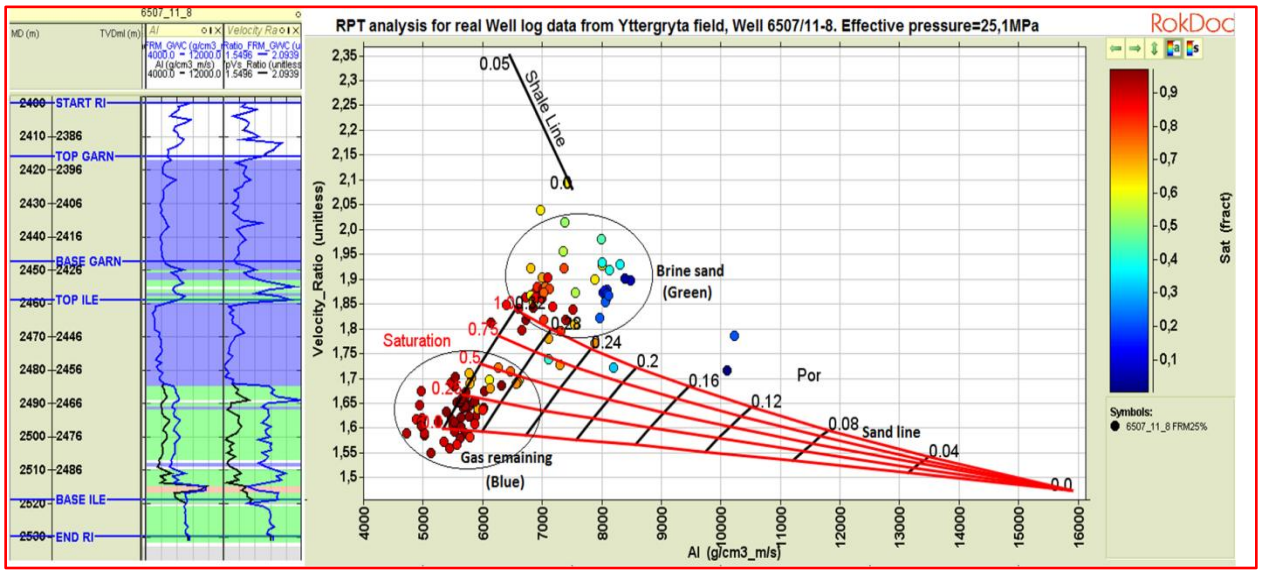

Figure 6.9: RPT analysis for monitoring of fluid contact in Ile Fm from base to a new position using CCT model. The plotted data on the RPT has been mapped onto the well-logs aside. The green-lower and blue-upper parts show portion of the reservoir that has been replaced with brine and still containing gas respectively. The data in the brine sand region on the RPT would be interpreted as full of gas but it is not, it is the gas which was originally in the reservoir but later replaced with brine as the contact moved to a new position.

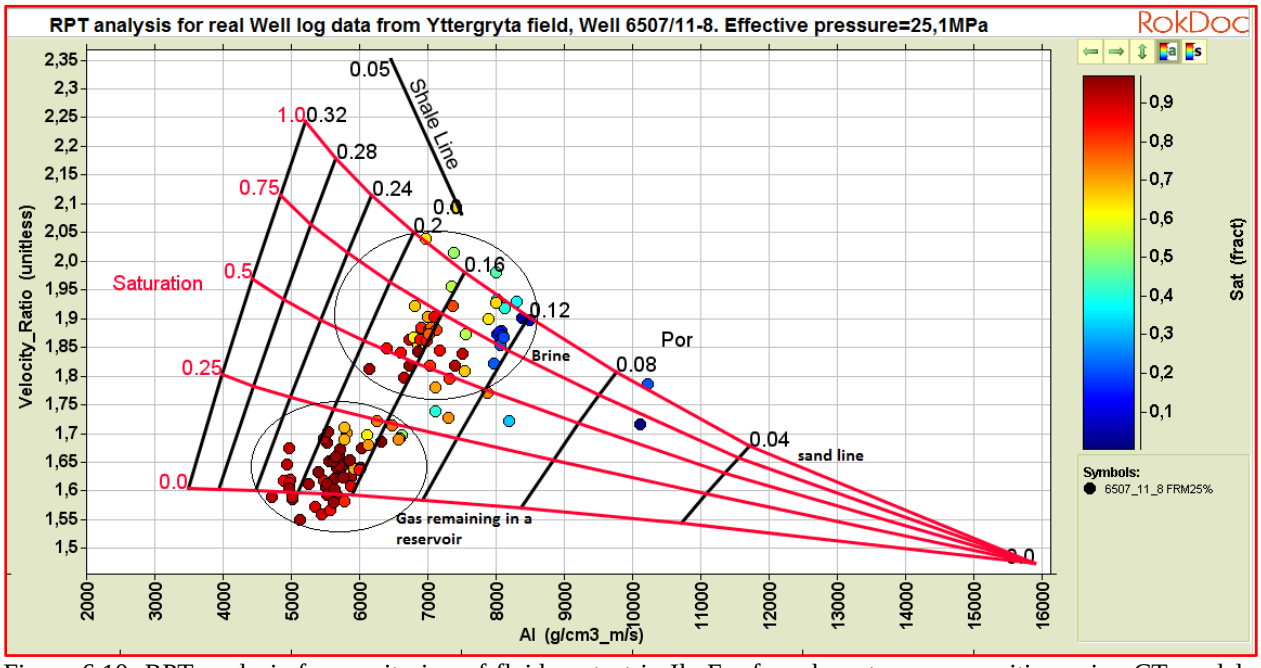

Figure 6.10: RPT analysis for monitoring of fluid contact in Ile Fm from base to a new position using CT model. The brine zone on the RPT was supposed to plot above the sand line (as in Figure 6.9) but it doesn't indicating a mismatch between the model and the dataset. The RPT shows also some gas remaining in the reservoir with the lowest Vp/Vs and AI. The color scale can be interpreted as in Figure 6.9.

6.4 Case 3: Gas-oil changes in the whole reservoir

In this case, gas has been substituted with oil in the whole reservoir from 2416-2519 m, MD from KB. Oil properties were considered as; density = 0.75 g/cc, bulk modulus =1 GPa. The Not formation has been skipped in the fluid replacement modeling.

In-situ Fluids		Output Fluids	
type	percentage	type	Percentage
Gas	96%	Gas	0%
Water	4%	Water	4%
Oil	0%	Oil	96%

Table 6.3: Case 3 FRM specifications

6.4.1 4D well-log effect modeling from Garn to Ile Fm

Gas in the whole reservoir has been substituted with oil as shown in Figure 6.11. Results show almost the same trend as seen before where brine replaces gas in the reservoir but in this case P-wave velocity does not greatly increase because of the somehow small contrast in the elastic properties between oil and gas. AVA synthetics using both gas and oil filled logs were computed and the difference taken as shown in Figure 6.11.

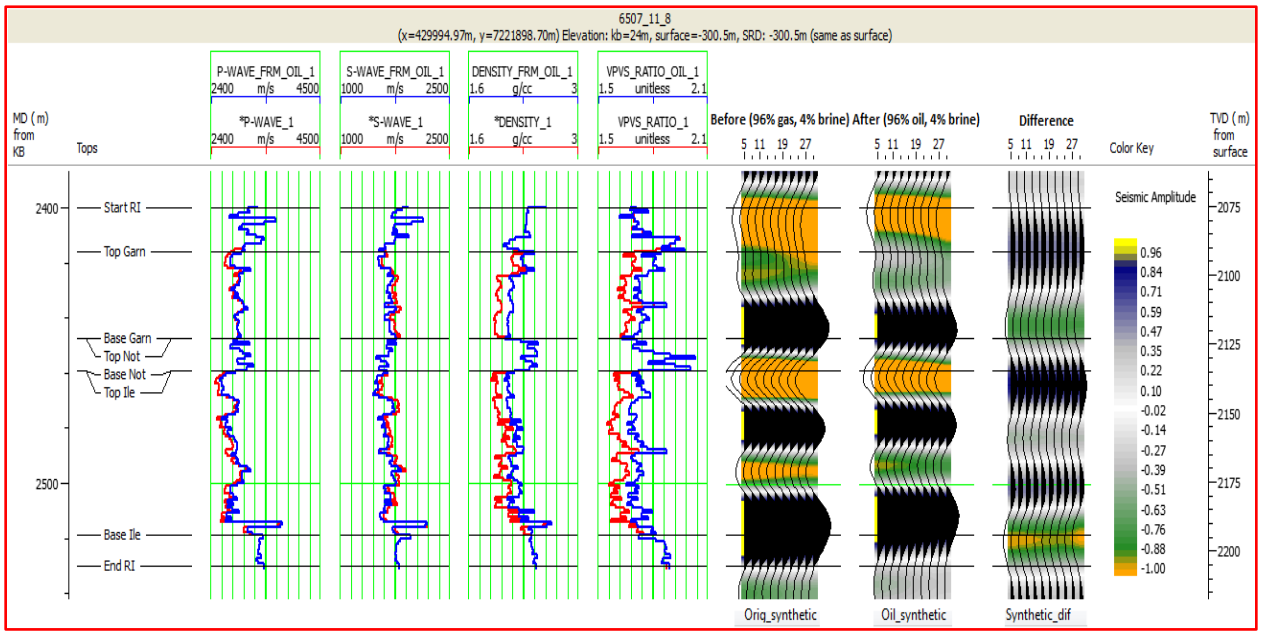

Figure 6.11: FRM results: blue and red well-logs are the oil (fluid substituted) and gas (original) saturated logs respectively. There is an increase in P-wave velocity, density, and Vp/Vs logs and a decrease in S-wave log as oil replaces gas in the reservoir. The increase in P-wave velocity is not large.

6.4.2 Stacking the AVA synthetics

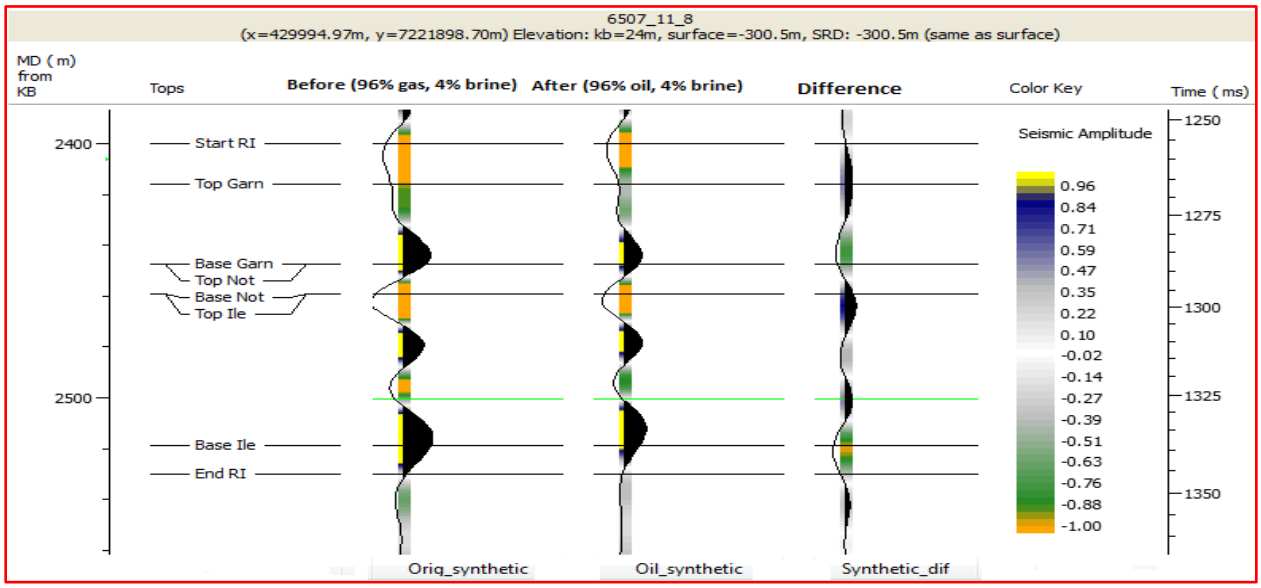

Figure 6.12: The stacked AVA synthetics for original (gas filled), oil filled and the difference. There is no phase reversal but a time shift is realized. Amplitude change is small because of the somehow low elastic property contrast.

6.4.3 RPT analysis for gas-oil substitution from Garn to Ile Fm.

The modeled gas to oil well-log data from the whole reservoir was plotted on an RPT based on oil-gas mixture as shown in Figure 6.13. Results show no good separation between the two populations of the data (the gas saturated sands-black with 96% gas and 4% brine, and oil saturated sands-blue with 96% oil and 4% brine). This is because of the somehow low elastic property contrast between gas and oil compared to that of gas-brine.

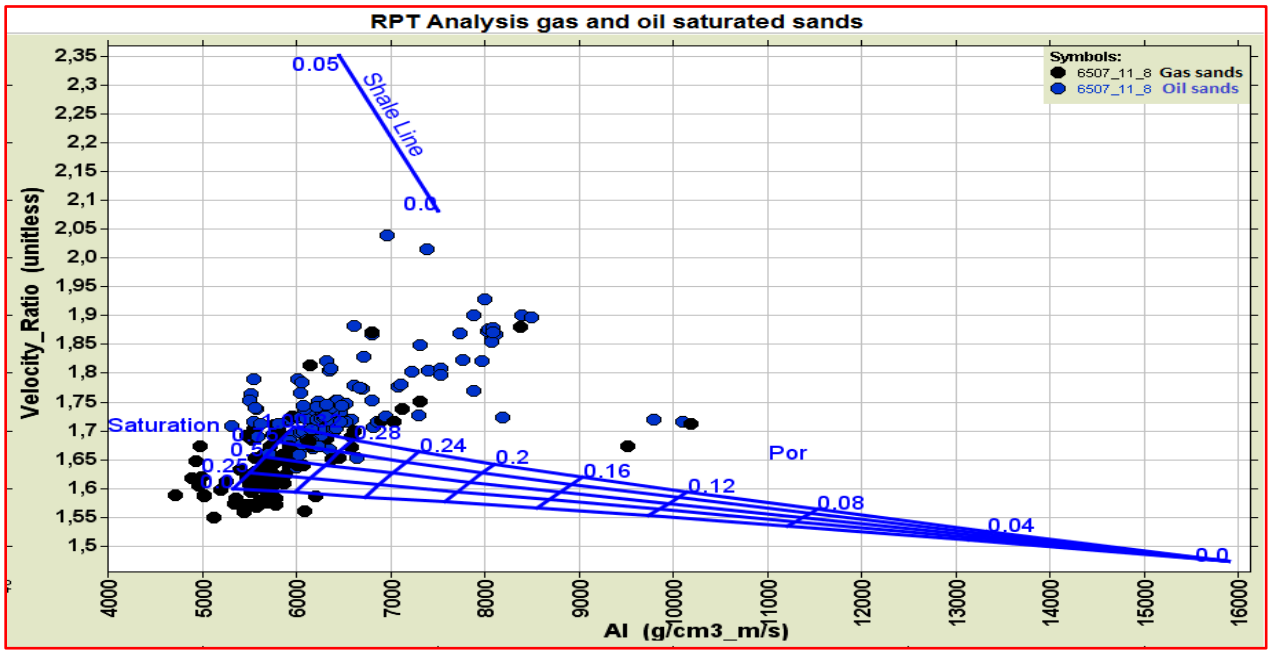

Figure 6.13: RPT analysis for gas-oil substituted well-log data using CCT model. Notice the poor discrimination between gas (black) and oil (blue) filled sands on the RPT due to the somehow low elastic property contrast between gas and oil.

6.5 Summary

Several differences have been observed (increments and decrements) in well-logs from fluid substitution results in this chapter. In all the FRM we considered gas being replaced with brine.

Increase in density log:

Brine has a higher density compared to oil and gas, ($\rho_b > \rho_o > \rho_g$). When rocks whose pores are originally filled with gas become filled with brine after some time, they become denser than before and the reverse is true. The order is: $\rho_{sat\_brine} > \rho_{sat\_oil} > \rho_{sat\_gas} > \rho_{dry}$ and this explains why in all the results as gas was being replaced by brine, density log increased.

Decrease in S-wave velocity log:

Gassmann's fluid substitution assumes that $\mu_{dry} = \mu_{sat}$ (shear modulus is independent of the saturating fluids). Based on this assumption and the fact that when gas is replaced by brine the rock becomes denser than before, this causes S-wave velocity to slightly decrease and the reverse is true. This explains why in all the above FRM results S-wave velocity log slightly decreased with increasing brine/oil saturation.

Increase in P-wave velocity log:

Brine has a very low compressibility coefficient, C (hence a high incompressibility (K) or bulk modulus, since K=1/C) compared to oil and gas. The order of magnitude of bulk moduli for brine, oil and gas is $K_b > K_o > K_g$. When rocks whose pores are originally filled with gas become filled with brine after some time, such rocks become stiffer than before and the reverse is true. In this case bulk modulus increases, shear modulus remains constant and density increases. This causes a conflict between bulk modulus and density, however in most cases the increase in density is small compared to that in bulk modulus and so P-wave velocity increases as observed in the results.

The remaining parameters: Vp/Vs, AI, SI, PR can then be calculated and studied based on the above changes in Vp, Vs and density. Generally in these results, all these logs shown a steady increase as gas was replaced by brine.

RPT changes in reservoir monitoring:

As already discussed above, when gas is gradually being replaced by brine, there is a steady increase in Vp/Vs and AI. If both original and FRM data are plotted on the same template, data will move along the saturation lines.

7.0 Discussion

7.1 Introduction

This study has mainly focused on two main areas as listed below:

- Reservoir characterization by predicting reservoir properties using RPTs
- Application of RPTs in 4D seismic reservoir monitoring applied on Yttergryta field

During this study there are some pitfalls encountered. The following section discusses the encountered pitfalls and how they were solved in the project.

7.2 Pitfalls and suggested solutions

The pitfalls encountered in this project generally were attached to: rock physics models, well-log data and rock physics modeling.

Pitfalls from rock physics models:

- Constant-cement model does not include pressure sensitivity. Instead, it assumes that the cemented grain contacts immediately lose pressure sensitivity as the cementation process initiates (Avseth and Skjei, 2012a), and this is not so true for real rocks.
- Hertz-Mindlin also has several short-comings (Bjørlykke, 2010). Firstly, the model assumes that the sediment grains are perfect, identical spheres, which is never found in real samples. Secondly, the ultrasonic measurements might suffer from scaling issues, core damage and so on. Thirdly, cementation effects are not included in the Hertz-Mindlin model. It is therefore important to note that there are major uncertainties regarding the actual dependency between seismic velocity and pore pressure change.

Pitfalls from well-log data:

- Many errors may occur in well-log measurements like: Vp, Vs and rho. Well-log data is subject to different sources of errors, which could inconvenience the geoscientist interpretation of data to give wrong results.
- Also porosity, shale content and saturation logs are logs that are created from transforming actual measurements (e.g. Resistivity analysis maybe influenced by misinterpretation).This means that the calibrated model may also be affected respectively.
- The well-logs also used in this project were logged starting from different depths. Water/gas saturation and porosity logs started from a depth of 2416 MD from KB at top Garn whereas volume (shale content) log started at a depth before top Garn (see Figure 3.6). These logs were used as color scales on the different RPTs presented. Notice that in all RPTs whose color scale is shale content/volume log, zone B has much data points compared to zone B in other plots whose color coding is either porosity or gas saturation. This is because of the difference in logging depth.

Pitfalls from modeling process

During modeling of RPTs many uncertain model parameters can be considered and these may include but not limited to; shear reduction factor, cementation factor (porosity range), sensitivity

and others. It is important to address these factors and how they were adjusted to fit the data and their effects because they may lead to uncertainties in the results.

- **Reduced shear effect (F)**

CT and CCT models are found to often overpredict shear stiffness in unconsolidated and cemented sandstones respectively. This overprediction of shear stiffness has an effect of increasing velocities. A reduced shear factor (F) has to be adjusted to honor this "reduced shear effect" in the models. F varies between 0 and 1 representing the boundary conditions between no-friction (Walton smooth contact theory) and no-slip (Walton rough or Hertz-Mindlin contact theory) conditions (Avseth and Skjei, 2012a). Also this factor has to be adjusted in the constant-cement model for good results.

Figure 7.1 shows how S-wave velocity is affected by increasing shear reduction factor. The same effect is observed on P-wave velocity (figure not shown) though to a less extent compared to S-wave velocity. This means that S-wave velocity is most likely to be overpredicted than P-wave velocity when a wrong factor is applied on a given dataset. This is because S-wave velocity depends on density and shear modulus (which is directly proportional to the reduced shear factor). The same effect was observed when a CT model was used though the trends were lower than those of a CCT model (figure not shown).

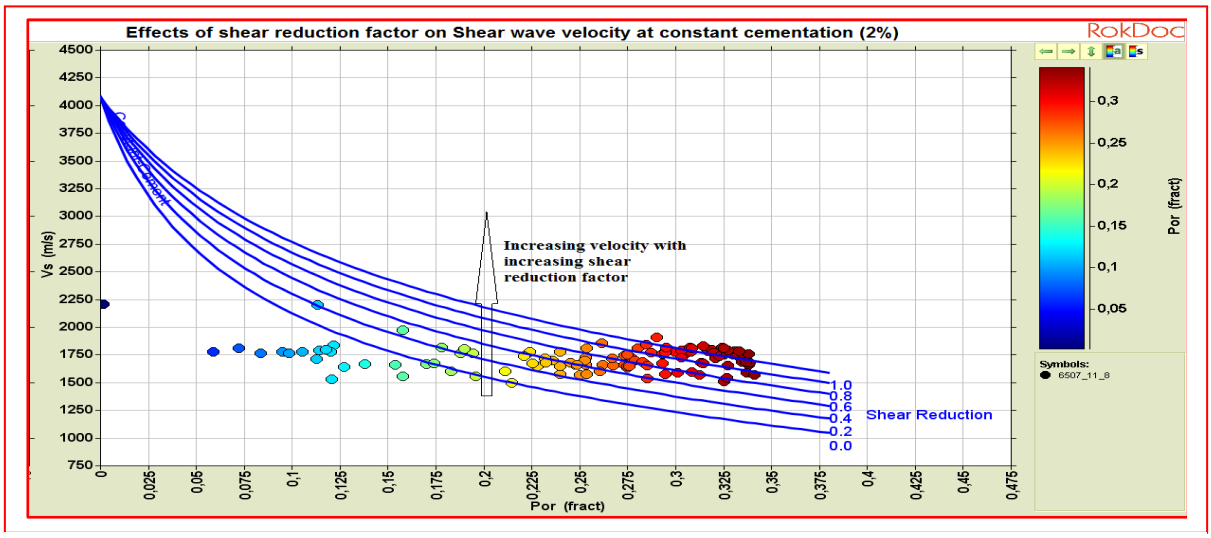

Figure 7.1: Effect of reduced shear friction factor on S- wave velocity at constant cementation of 2% using CCT model. It was noticed that S-wave velocity is affected more strongly compared to P-wave velocity (figure not shown) as the shear reduction factor increases.

These shear effects on P- and S-wave velocity directly affect the Vp/Vs and AI thereby making wrong estimates (over/underestimates) from the model as shown in Figure 7.2. In this project, shear reduction factor has been adjusted from F=1 to F=0.3 to fit the dataset from Yttergryta field in the Norwegian Sea. If this factor was not reduced, it would give very wrong interpretations based on the template as it can be seen from Figure 7.2.

Looking at Figure 7.2, a 90% gas saturation data with an average porosity of 18% from a blue CT model (F=0.3) would be interpreted as a 60% gas saturation data with an average porosity of 26% from a black CT model (F=1). This would be a large underestimation of the results. The

same trend is observed on a CCT model (figure not shown) when F=0.3 and F=1, no gas sands would be realized in such a case of F=1 and the model would completely fail to match the dataset. The match between the fluid and lithology trends on the templates for CCT and CT gives some good reasonable meaning with respect to the well-log data plotted when F=0.3 not F=1.

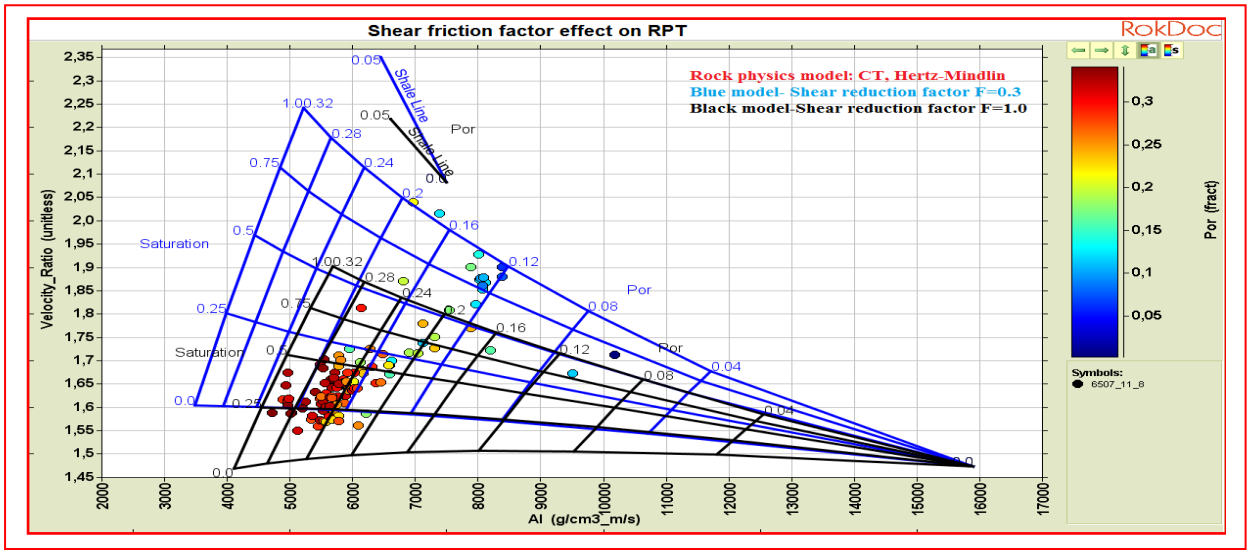

Figure 7.2: Effect of shear reduction factor on Vp/Vs, AI and how it may affect the predictions from the rock physics models. The RPT is based on contact theory (Hertz-Mindlin) model. The RPT shows how the results would be affected if the shear friction factor was not adjusted. For Yttergryta data set, a shear friction factor, F=0.3 was found to fit the data.

- **Cementation factor (range) effect:**

As porosity reduces due to increasing cement volume, this stiffens the rock frame and seismic velocities also increase. Figure 7.3 shows how P-wave velocity is affected by increasing cement volume at a constant shear friction factor with respect to porosity. Velocity increases when cement volume is low: 1%, 2%, 4% and 8% and further increase in cement to 14% causes almost no increase in velocity, this could be because all small cracks, pores and fractures have been filled with cement and are closed so that further addition of cement causes almost no effect.

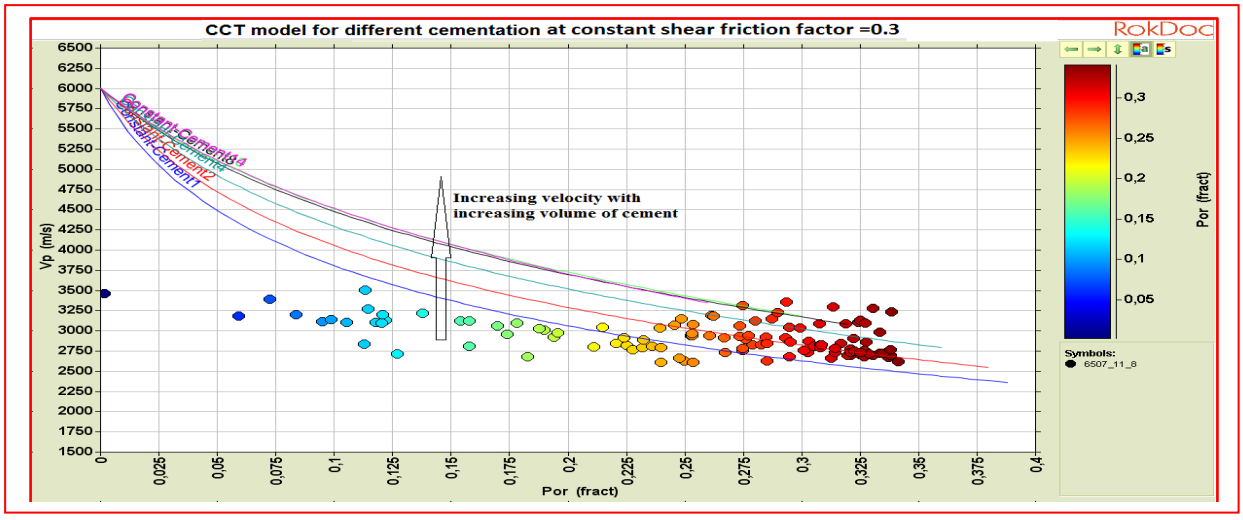

Figure 7.3: Effect of increasing cement volume in a rock on seismic velocities. Cement is increasing in volumes of 1%, 2%, 4%, 8% and 14%. In this project cementation of 8% for the CCT model was used (approximate porosity range was from 0.398-0.40).

7.3 Fluid sensitivity, reservoir characterization and monitoring analysis

The reservoir zone in the study field was unconsolidated, partly clean and partly dirty sandstone with some cementation. Hence, three models were tested on this dataset in this project; friable sand model (CT), constant cement model (CCT) and patchy cemented sandstone model (PC). CT model which is based on Hertz-Mindlin theory was used in order to determine the sensitivity of seismic velocity to pressure. The CCT model was used to assess the degree of cementation and the third model (patchy cemented sandstone model) was later tested to see how it matches the dataset.

- **Fluid sensitivity analysis:**

Constant-cement (CCT) model assumes a stiffer rock frame and so there is small fluid sensitivity compared to friable (CT) sand model. In CCT model cementation was applied between porosity range of 0.398-0.40. The results show that for a CT model, Vp/Vs and AI increases dramatically with just little addition of brine saturation compared to the same effect in CCT. Figure 7.4 shows plots of bulk modulus against porosity (top) for CCT and CT models, and rock physics templates (bottom) based on those models. CCT has a linear trend and a hard break in the plot for porosities between 0.398-0.40. This is because of the not small enough sampling steps, otherwise it should be non-linear and smooth.

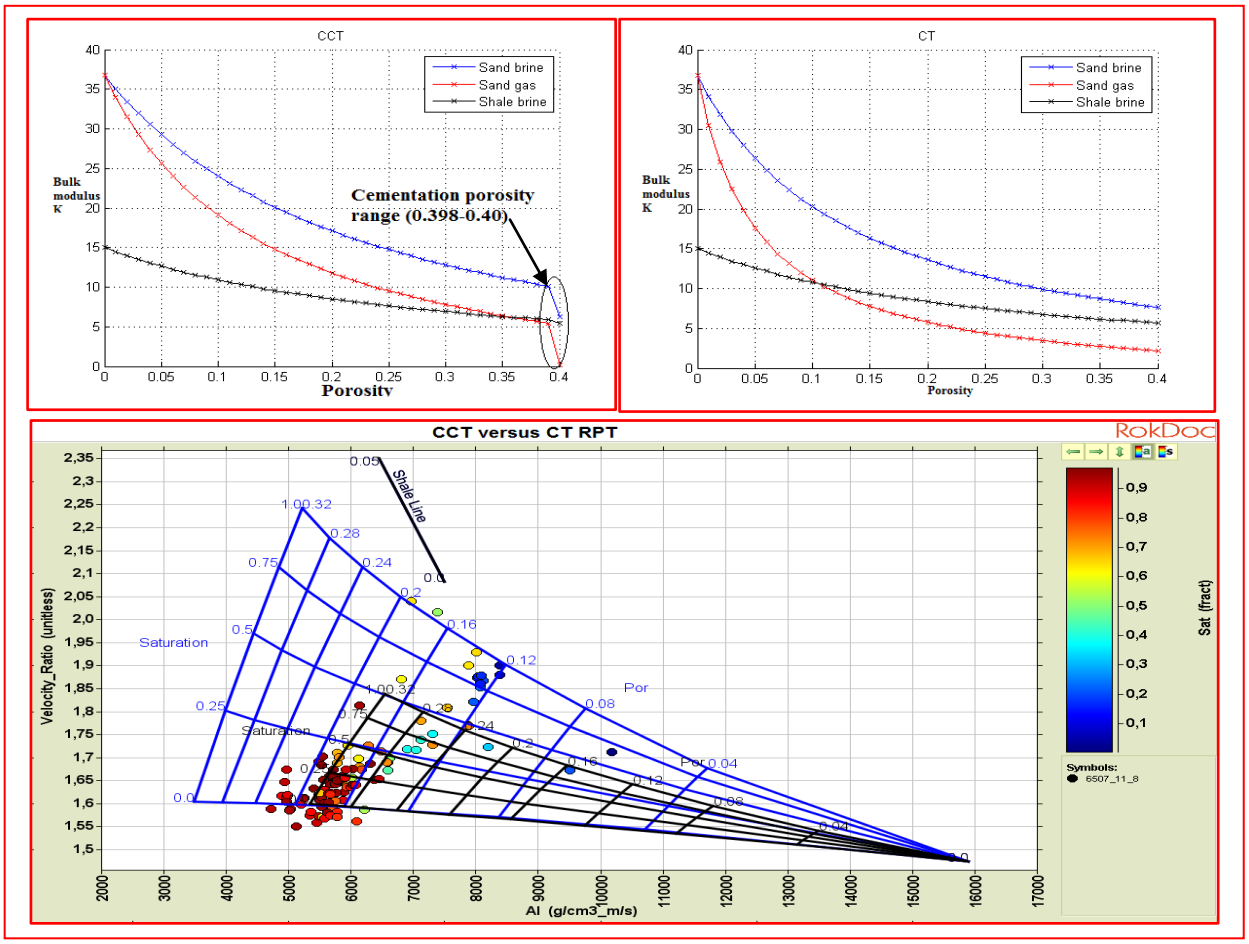

Figure 7.4: Sensitivity analysis of the two models: CCT and CT models at the same inputs and cementation is 8% for the CCT model. The CCT RPT model overpredicts porosity (average 32%) while the CT RPT model underpredicts it (18%).

- ***Patchy cemented sandstones analysis:***

Patchy cementation is where some grain contacts are cemented and others are loose. A patchy cemented sandstone model was applied to this dataset to see how it matches the data after testing using CCT and CT. The data used in the entire project is from the interval of 2400-2530 m, MD of KB, so the sand and shale in this well at this depth are believed to be compacted.

Also quartz cementation tends to occur at temperatures beyond 80 ºC (Bjørlykke, 2010) and in this well, the temperature in the working interval was 91 ºC, this may suggest why the sands were partially cemented. These conditions may try to explain the nature of the lithology in each of the formations as noted in **Section 2.5** where some formations contain carbonate cemented sands. With such observations and conditions, it is easy to understand why the two models, CCT and CT didn't fit this dataset whereas a patchy cemented sandstone model had a relatively good match.

- ***Reservoir monitoring analysis:***

Evaluation of the three models in reservoir monitoring was tested by plotting the original data (96% gas, 4% brine), brine substituted data (50% brine, 50% gas) and fully brine saturated data (100% brine, 0% gas) as shown in Figure 7.5. Results showed that CT model (not shown in Figure 7.5) underpredicted the modeled saturations, CCT model slightly matched it and a patchy cemented sandstone model was later tested. The results showed a good match between the RPT predicted and the modeled saturations for patchy cemented model. The zones on Figure 7.5 represent the original data and the modeled saturations (50% and 100% brine) as labeled on the RPTs. The color scale does not apply on the RPT for a patchy cemented sandstone model.

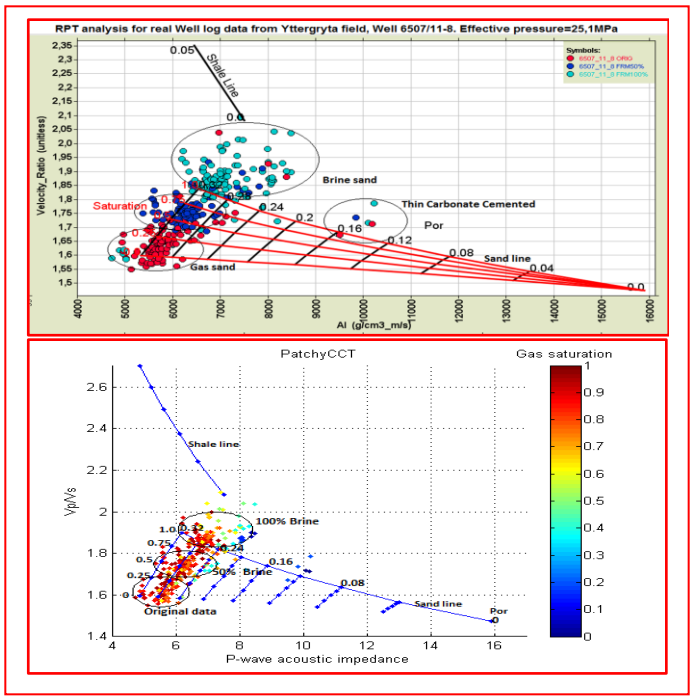

Figure 7.5: RPT analysis for both original, 50% and 100% brine substituted data in the whole reservoir interval. CCT (middle) and patchy cemented sandstone model (bottom). It can be noted that the modeled saturations are perfectly matched with respect to the RPT saturations in case of patchy cemented sandstone model compared to constant-cement model. RPT based on friable sand model was left out because of a very poor match.

Because only sandstone was assumed as the rock type for the whole matrix in fluid substitution modeling (which is slightly not true in reality), there is a possibility for all the three models to have predicted better results if different rock matrix properties were specified.

7.4 Rock physics template interpretation of the "*What ifs*"

The reservoir interval and all formations considered in this project were filled with gas, therefore the models described in Chapters 5 and 6 best fit brine-gas fluid mixture. However if the reservoir contained oil instead of gas, a brine-oil fluid mixture would be considered. Because the elastic behavior of oil and gas are significantly different (Batzle and Wang, 1992) as demonstrated in Figure 7.6. The property contrast between oil and brine are significantly smaller than for gas and brine.

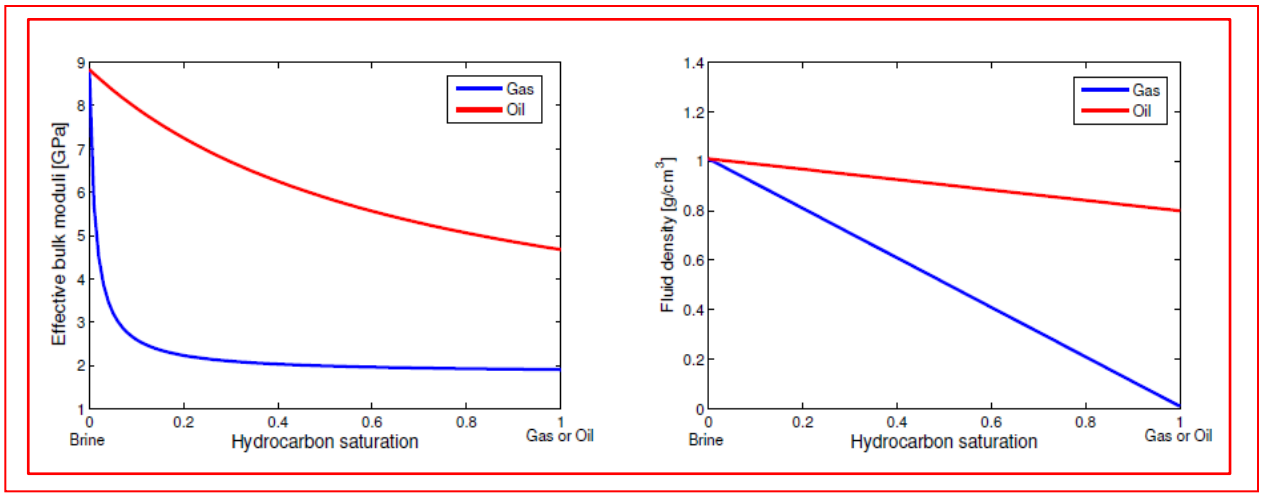

Figure 7.6: The effective bulk moduli (left) and fluid density (right) between gas and oil substitution modeled by the Gassmann's model. The bulk moduli of gas and oil used here are: 0.03 GPa and 1 GPa respectively. The density of brine, gas and oil used here are: 1.01 g/cm3, 0.01 g/cm3 and 0.8 g/cm3 respectively. (Figure adapted from Bredesen, 2012)

If a well contains only gas and brine, it is very easy to interpret the results based on a gas-brine mixture RPT, since the two have a large elastic property contrast. A good separation between brine and gas sands can be seen on the RPT (Figure 7.7, left). However if a well contains oil instead of gas as modeled in this case, where oil sands are replaced by brine sands it can be a bit challenging. This is because of the low property contrast between oil- and brine-saturated rock, so discrimination of brine and oil on an RPT can be difficult (Lumley, 2001), Figure 7.7 (right).

A further challenging situation in reservoir monitoring using RPT is when a well contains gas, oil and brine. It can be difficult to distinguish between the three; gas sands (black), brine sands (light blue) and oil sands (red). Oil sands plot as low gas saturation sands (Avseth et al., 2005) as shown on Figure 7.7. The RPT is based on a gas-brine mixture.

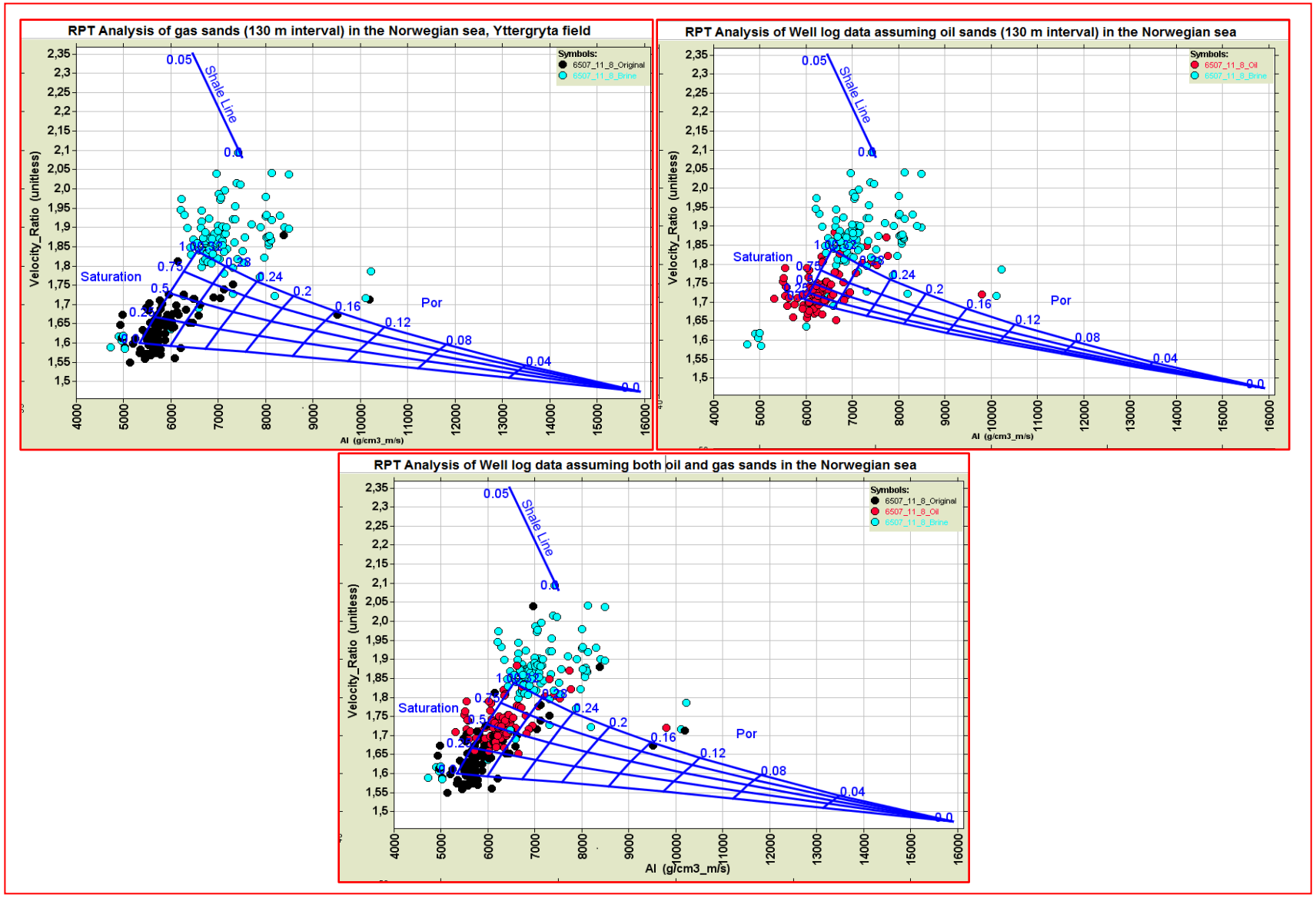

Figure 7.7: RPT analysis for gas/brine (top-left), oil/brine (top-right) and gas/oil/brine (bottom) on their respective templates using a CCT model. Light blue shows 100% brine data, red for 96% oil and black data for 96% gas. Oil sands (red data) plot as low gas saturation sands because of the low property contrast (as shown in figure, bottom).

7.5 Rock physics model evaluation

Rock physics models have been evaluated based on their predictions with respect to the well-log measured properties. Table 7.1 gives the summary of the evaluation of the three (3) models applied in this project.

Zones on the RPT	Predicted properties by RPT Versus well-log data measurements											
	CT			CCT			PC			Well-log measurements (color scale interpretation)		
	S_g	Ø	$Litho, V_{sh}$	S_g	Ø	$Litho, V_{sh}$	S_g	Ø	$Litho, V_{sh}$	S_g	Ø	$Litho, V_{sh}$
Zone A	75-100	14-22	Gas sands	50-100	26-36	High gas sands	50-100	24-34	Gas sands	80-100	25-35	0-0.2
Zone B	50-75	12-14	Gas sands/shaly	0-50	24-28	Low gas sands/shaly	0-50	18-24	Gas sands	40	14,18,22	0-0.6
Zone C	0-50	12-14	Very low gas sands/shaly	0	24-32	Brine sands/shaly	0	20-28	Brine sands/shaly	0, 65	0-22	0.4-0.6

Table 7.1: Summary of the RPT predictions based on different rock physics models and real well-log measured properties. S_g is gas saturation (%), Ø is porosity (%) and $Litho, V_{sh}$ is lithology/volume of shale.

- Zone C is predicted as gas (0-50%) in case of CT model and pure brine (0% gas) plotting above the brine sand line in case of CCT and PC.
- According to Figure 5.4, zone C data comes from two (2) regions. The first region is the Not formation which has some gas almost 65% (see Figure 3.6, **Section 3.3.1**, geophysical well-log interpretation). In this case, the CT model prediction (0-50% gas) slightly matches the well-log measured saturation. The second region is the Ror formation which is brine saturated (0% gas) below Ile formation and some parts in the Not formation. In this case, the CCT and PC model which predicted zone C as brine saturated and plotting above the brine sand line match well with the observations.
- The three model predictions are reasonable since the Not formation has both gas and some brine, also the Ror formation is brine saturated as predicted by the CCT and PC.

8.0 Conclusions

This study has demonstrated the applications of rock physics templates (static and dynamic) in reservoir characterization and monitoring based on three models. The study has been performed on real well-log data from Yttergryta field of the Norwegian Sea to predict lithology, porosity, pressure and saturation changes.

The three reasonable models which were applied on the dataset are: constant-cement model, friable sand model and patchy cemented sandstone models. The following are some of the conclusions from this study on each model:

- **Constant-cement model**
  This model was found to overpredict both porosity (average 32%) and gas saturation (100%). Some points plotted off the template but could be considered as gas sands.
- **Friable sand model**
  Large differences between the predicted and the well-log measurements were observed. The model was found to underpredict porosity (18%) and gas saturation on average 96% was predicted. No brine sands were predicted.
- **Patchy cemented sandstone model**
  This model demonstrated a high degree of consistency. The model predicted on average: 96% gas saturation and 28% porosity (good match with the well-log measurements). The predicted lithology and fluid zones on the template were also checked for consistency using well-logs.

4D RPTs presented in this study have demonstrated how saturation and pressure would change if there were such changes in a reservoir.

From the rock physics model evaluation (based on Table 7.1) and findings, patchy cemented sandstone model proved to perfectly fit the well-log dataset from Yttergryta field, Norwegian Sea. It was able to predict the exact average porosity, 28% (referenced from NPD, 2014), reservoir fluids (gas and brine), average gas saturation as 96% and lithology as patchy cemented sandstones.

8.1 Recommendation for further study

Below are some recommendations for further study:

- Interpreting seismic inverted data from this field using the same RPTs to compare the results with those obtained by using well-log data, as this will also help to extrapolate the reservoir properties away from the well, since well-log data is much focused near the wellbore unlike seismic which covers a large area beyond wellbore.
- It would be extremely useful to apply the same workflows designed in this project to fit well 6507/11-8 on well 6507/11-9 since they are in close vicinity to test the sensitivity of an RPT towards variations in geological settings.

Appendix 1: List of figures

Appendix 2: Figures, tables and equations

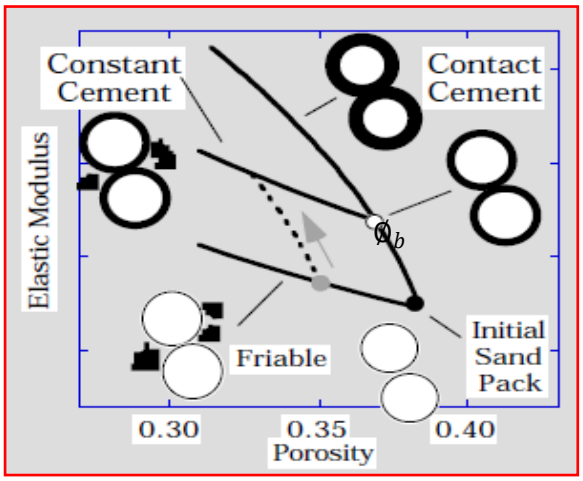

Figure A: Some common rock physics models (Avseth et al., 2005)

Coefficients for water properties computation	
$w_{00} = 1402.85$	$w_{02} = 3.437 \times 10^{-3}$
$w_{10} = 4.871$	$w_{12} = 1.739 \times 10^{-4}$
$w_{20} = -0.04783$	$w_{22} = -2.135 \times 10^{-6}$
$w_{30} = 1.487 \times 10^{-4}$	$w_{32} = -1.455 \times 10^{-8}$
$w_{40} = -2.197 \times 10^{-7}$	$w_{42} = 5.230 \times 10^{-11}$
$w_{01} = 1.524$	$w_{03} = -1.197 \times 10^{-5}$
$w_{11} = -0.0111$	$w_{13} = -1.628 \times 10^{-6}$
$w_{21} = 2.747 \times 10^{-4}$	$w_{23} = 1.237 \times 10^{-8}$
$w_{31} = -6.503 \times 10^{-7}$	$w_{33} = 1.327 \times 10^{-10}$
$w_{41} = 7.987 \times 10^{-10}$	$w_{43} = -4.614 \times 10^{-13}$

Table A: Constants (ω_{ij}) for water properties computations

Equation set 2.1

$S_n = A_n(\Lambda_n)\alpha^2 + B_n(\Lambda_n)\alpha + C_n(\Lambda_n), A_n(\Lambda_n) = -0.024153\Lambda_n^{-1.3646}$
$B_n(\Lambda_n) = 0.20405\Lambda_n^{-0.89008}, \; C_n(\Lambda_n) = 0.00024649\Lambda_n^{-1.9864}$

$S_\tau = A_\tau(\Lambda_\tau, \nu_s)\alpha^2 + B_\tau(\Lambda_\tau, \nu_s)\alpha + C_\tau(\Lambda_\tau, \nu_s)$

$A_\tau(\Lambda_\tau, \nu_s) = -10^{-2} \times (2.26{\nu_s}^2 + 2.07\nu_s + 2.3)\Lambda_\tau^{0.079{\nu_s}^2 + 0.1754\nu_s - 1.342}$

$B_\tau(\Lambda_\tau, \nu_s) = (0.0573{\nu_s}^2 + 0.0937\nu_s + 0.202)\Lambda_\tau^{0.0274{\nu_s}^2 + 0.0529\nu_s - 0.8765}$

$C_\tau(\Lambda_\tau, \nu_s) = -10^{-4} \times (9.654{\nu_s}^2 + 4.945\nu_s + 3.1)\Lambda_\tau^{0.01867{\nu_s}^2 + 0.4011\nu_s - 1.8186}$

$\Lambda_n = \frac{2\mu_c(1-\nu_s)(1-\nu_c)}{[\pi\mu_s(1-2\nu_c)]}, \Lambda_\tau = \mu_c/(\pi\mu_s)$

$\alpha = [(2/3)(\emptyset_c - \phi)/(1-\emptyset_c)]^{0.5}$

$\nu_c = 0.5(\frac{K_c}{\mu_c} - 2/3)/(\frac{K_c}{\mu_c} + 1/3)$

$\nu_s = 0.5(\frac{K_s}{\mu_s} - 2/3)/(\frac{K_s}{\mu_s} + 1/3)$

Equation set 2.2

$A = \frac{1}{4\pi}\left\{\frac{1}{\mu_s} - \frac{1}{\mu_s - \lambda_s}\right\}$ $B = \frac{1}{4\pi}\left\{\frac{1}{\mu_s} + \frac{1}{\mu_s - \lambda_s}\right\}$, where λ_s is the Lame's parameter of the solid grains and c_0 is the coordination number

References

Andersen, C. F., Grosfeld, V., Wijngaarden, A.J.V., and Haaland, A. N., 2009, Interactive Interpretation of 4D prestack inversion data using rock physics templates, dual classification, and real-time visualization, *THE LEADING EDGE, 2009*

Avseth, P., and Ødegaard, E., 2004, Well log and seismic data analysis using rock physics templates, *First Break, 23, 37-43*

Avseth, P., Mukerji, T., and Mavko, G., 2005, Quantitative Seismic Interpretation: Applying Rock Physics Tools to Reduce Interpretation Risk, *Cambridge University Press*.

Avseth, P., Jørstad, A., Wijngaarden, A. J. V., and Mavko, G., 2009, Rock physics estimation of cement volume, sorting, and net-to-gross in North Sea sandstones, *THE LEADING EDGE, 2009*

Avseth, P., Skjei, N., and Mavko, G., 2012, Rock physics modeling of stress sensitivity in patchy cemented sandstones. *EAGE Expanded Abstract, 74th EAGE conference, Copenhagen, June 2012*

Avseth, P., and Skjei, N., 2012a, Method of predicting the pressure sensitivity of seismic velocity within reservoir rocks, *accessed on: 15.05.2014 approx. 18:00 from http://www.google.com/patents/CA2812155A1?cl=en*

Batzle, M., and Wang, Z., 1992, Seismic properties of pore fluids: *Geophysics, **57** (11), 1396–1408*

Brie, A., Pampuri, F., Marsala, A.F., and Meazza, O., 1995, Shear sonic interpretation in gas-bearing sands, *SPE, 30595, 701-710*

Bjørlykke, K., 2010, Petroleum Geoscience: From Sedimentary Environments to Rock Physics, *Springer-Verlag Berlin Heidelberg, e-ISBN: 978-3-642-02332-3*

Bredesen, K., 2012, Use of inverse rock physics modeling in reservoir characterization, *Master thesis, University of Bergen, accessed on: 10.02.2014 from https://bora.uib.no/handle/1956/7462*

CGG, 2014, 4D RPT, *accessed on: 10.03.2014 approx. 17:00 from http://www.cggveritas.com/downloads/flyers/Hampson-Russell/RockSI.pdf*

Chen, C. T., Chen, L. S., and Millero, F. J., 1978, Speed of sound in NaCl, MgClz, NazS04, and MgS04 aqueous solutions as functions of concentration, temperature, and pressure, *J. Acoust. Sot. Am., 63, 1795-1800*

Chi, X. G., and Han, D. H., 2009, Lithology and Fluid differentiation using rock physics template, *THE LEADING EDGE, 2009, 1424-1428*

Domenico, S.N., 1977, Elastic properties of unconsolidated porous sand reservoirs, *Geophysics, 42, 1339-1368*

Domenico, S.N., 1976, Effect of brine-gas mixture on velocity in an unconsolidated gas reservoir, *Geophysics, 41, 882-894*

Dvorkin, J., Nur, A., and Yin, H., 1994, Effective properties of cemented granular material, *Mech. Mater., 18, 351-366*

Dvorkin, J., Prasad, M., Sakai, A., and Lavoie, D., 1999a, "Elasticity of marine sediments: rock physics modeling", *Geophy. Res. Lett., 26, 1781-1784.*

Ferguson, T. R., and Bazant, M. Z., 2012, Nonequilibrium Thermodynamics of Porous Electrodes, *J. Electrochem., Soc., 2012, 159 (12), 1967-1985*

Gassmann's assumptions, *accessed on: 23.02.2014 approx. 16:11 from http://en.wikipedia.org/wiki/Gassmann's_equation*

Han. D. H., and Batzle, M.L., 2004, Gassmann's equation and fluid-saturation effects on seismic velocities, *Geophysics, 69 (2), 398–405*

HRS, 2013, Patchy Saturation notes, *accessed on: 20.09.2013 approx. 15:10 from Hampson Russell Help assistant manual*

Johansen, T. A., 2014, seismic properties of pore fluid substitution, *accessed on: 04.05.2014 approx.20:20 from http://buster.geo.uib.no/emodules/modules/Seismic%20properties%20of%20fluid/Seismic%20properties.swf*

Johansen, T. A., Åsmund Drottning., Lecomte, I., and Gjøystdal, H., 2002, An approach to combined rock physics and seismic modeling of fluid substitution effects, *Geophysics Prospecting, 2002, 50 (2), 119-137*

Lumley, D.E., 2001, Time-Lapse seismic reservoir monitoring, *Geophysics*, 66 (1), 50-53

Marsh, N.A., 2008, The influence of crustal extension, salt tectonics and gravity-driven deformation on the structural evolution of the Halten Terrace, offshore mid-Norway: new sights from 3D seismic data and fault analysis, *PhD thesis, Durham University, accessed on: 15.03.2014 approx. 21:00 from http://etheses.dur.ac.uk/1933/1/1933.pdf*

Mavko, G., Mukerji, T., and Dvorkin, J., 2009, The Rock Physics Handbook: *Tools for Seismic Analysis of Porous Media (Second ed.), Cambridge University Press*

Mavko, G., 2014, Parameters That Influence Seismic Velocity, *accessed on: 01.03.2014 approx. 17:30 from https://pangea.stanford.edu/courses/gp262/Notes/8.SeismicVelocity.pdf*

Millero, F. J., Ward, G. K., and Chetirkin, P. V., 1977, Relative sound velocities of sea salts at 25°C, *J. Acoust. Sot. Am., 61, 1492-1498*

NPD., Yttergryta field and well 6507/11-8, 2014, *accessed on 10.10.2014 approx. 08:30 from http://factpages.npd.no/factpages/Default.aspx?culture=no*

Ødegaard, E., and Avseth, P., 2003, Interpretation of elastic inversion results using rock physics templates, *EAGE Ann. Mtg Extended Abstract*

PetroWiki., 2014, *accessed on 10.01.2014 approx. 08:00 from http://petrowiki.org/images/d/df/Vol1_Page_627_Image_0001.png*

Rider, M., & Kennedy, M., 2000, The Geological Interpretation of Well Logs, *Third Edition, ISBN: 0-9541906-0-2*

Rojas, E., Davis, T. L., Batzle, M., and Prasad, M., 2005, Vp-Vs ratio sensitivity to pressure, fluid, and lithology changes in tight gas sandstones, *SEG, 2005, Houston Annual Meeting*

Shuey, R.T., 1985, A simplification of the Zoeppritz Equations, *Geophysics, **50**, 609-614*

Smith, T. M., Sondergeld, C. H., and Rai, C. S., 2003, Gassmann fluid substitutions: a tutorial: *Geophysics, 68 (2), 430-440*

Smith, T. M., 2011, Practical Seismic Petrophysics: The Effective Use of Log Data for Seismic Analysis. *The Leading Edge, 30, 1128 – 1141*

Statoil., 2013, Yttergryta field in the Norwegian Sea, *accessed on: 20.12.2013 approx. 10:00 from http://www.statoil.com/en/ouroperations/explorationprod/ncs/yttergryta/pages/default.aspx*

Unigeo., 2014, *accessed on: 10.02.2014 approx. 17:00 from unigeo.no*

Unknown author., 2014, Halten Terrace, *accessed on 10.03.2014 approx. 18:00 from http://www.sitechar-co2.eu/Sections.aspx?section=556.562*

Walton, K., 1987, The effective elastic moduli of a random packing of spheres, *J. Mech. Phys. Solids, 35(2), 213-226*

Wilson. W. D., 1959, Speed of sound in distilled water as a function of temperature and pressure, *J. Acoust. Sot. Am., 31, 1067-1072.*

Wisconsin, 2014, Voigt and Reuss model and Hashin-Shtrikman bounds, *accessed on: 10.02.2014 approx. 19:00 from http://silver.neep.wisc.edu/~lakes/VECmp.html*